Spring 1-1-2017

Microfluidic-Based Broadband Measurements of Fluid Permittvity and Permeability to 100 Ghz

Charles Little
University of Colorado at Boulder, caelittle@gmail.com

Microfluidic-based Broadband Measurements of Fluid Permittivity and Permeability to 100 GHz

By

Charles A. E. Little

B.A. Physics, Appalachian State University, 2008
M.S. Mechanical Engineering, University of Colorado – Boulder, 2013

A thesis submitted to the
Faculty of the Graduate School of the
University of Colorado in partial fulfillment
of the requirement for the degree of
Doctor of Philosophy
Department of Mechanical Engineering
2017

This thesis entitled:
"Microfluidic-based Broadband Measurements of Fluid Permittivity and Permeability to 100 GHz"
written by Charles A. E. Little
has been approved by the Department of Mechanical Engineering

Prof. Victor M. Bright

Dr. James C. Booth

Prof. Yifu Ding

Prof. Xiaobo Yin

Prof. Dimitra Psychogiou

Date

The final copy of this thesis has been examined by the signatories, and we find that both the content and the form meet acceptable presentation standards of scholarly work in the above mentioned discipline.

Little, Charles Anderson Enright (Ph.D. Mechanical Engineering)

Microfluidic-based Broadband Measurements of Fluid Permittivity and Permeability to 100 GHz

Thesis directed by Prof. Victor M. Bright and Dr. James C. Booth

Abstract

This dissertation concerns the development of unique microfluidic microwave devices and associated microwave calibrations to quantitatively extract the broadband permittivity and permeability of fluids between 100 kHz and 110 GHz. The devices presented here consist of SU-8- and PDMS-based microfluidic channels integrated lithographically with coplanar waveguides (CPWs), measured via an external vector network analyzer (VNA). By applying our hybrid set of microwave calibrations to the raw data we extract distributed circuit parameters, representative of the electromagnetic response of the microfluidic channel. We then correlate these parameters to the permittivity and permeability of the fluid within the channels. We are primarily focused on developing devices, calibrations, and analyses to characterize various chemical and biological systems. The small fluid volumes and overall scale of our devices lends the technique to point-of-care blood and cell analysis, as well as to the analysis of high-value chemicals. Broadband microwave microfluidics is sensitive to three primary categories of phenomena: Ionic, dipolar, and magnetic resonances. All three can occur in complex fluids such as blood, proteins and particle suspensions. In order to make quantitative measurements, we need to be able to model and separate all three types of responses.

Here we first measure saline solutions (NaCl and water) as an ideal system to better understanding both the ionic and dipolar response. Specifically, we are targeting the electrical double-layer (EDL) response, an ionic effect, which dominates over the intrinsic fluid response at lower frequencies. We have found that the EDL response for saline obeys a strict Debye-type relaxation model,

the frequency response of which is dependent solely on the conductivity of the solution. To develop a better understanding of the magnetic response, we first measure magnetic nanoparticles; showing it is possible to detect the magnetic resonances of magnetic nanoparticle in a fluid environment using the broad-band approach, and that the response matches cavity-based measurements. In addition, we demonstrate the complicated intermixing that occurs between magnetic and electrical responses in CPW-type measurements through both numerical modeling, and empirical measurements of embedded permalloy devices.

Acknowledgements

I would first like to thank Dr. James C. Booth and my advisor Dr. Victor M. Bright, for their mentorship over these many years, which has been integral to my success. Before I began this work, I had very little to no understanding of microwave science. That being the case, Dr. Booth gave me the opportunity to prove myself, which has meant a lot to me. I have considered myself very lucky to have work with and around Dr. Booth over this period. I would be happy if even a small portion of his knowledge and expertise has rubbed off. I am also very appreciative to Dr. Bright for letting me join his research group. He is a leader in the field of MEMS, and it is an honor to have been one of this graduate students. I'd also like to thank everyone in Dr. Bright's group: Joe Brown, Nate Eigenfeld, Omkar Supekar, Kristen Genter, Jonas Gertsch, Wei Lim, and Philip Nystrom. Having this community has pulled me through a lot of hard times.

There are also a number of people at the National Institute of Standards and Technology (NIST), which I need to thank: Angela Stelson, Nate Orloff, Chris Long, Xifeng Lu, Aaron Hagerstrom, Nina Basta, Jasper Drisko, and many others who have helped me in one way or another. In addition, I need to thank NIST itself for the NIST-on-a-chip program that has funded this work.

The one person who has probably contributed the most directly in both time and labor has been Isaac Hanemann. Isaac is currently an undergraduate student in the physics department at the University of Colorado. He has worked at NIST for the past three years. During this time, he has worked tirelessly in the clean room to fabricate devices, and has contributed immensely to the development of our fabrication processes. He deserves a lot of credit for the work presented in this dissertation. So thank you Isaac!

Lastly, I'd like to thank family and friends. My parents, Andy Little and Katie Early, who have both provided me with much support. All the friends who I have not already mentioned, especially Leyla Murphy and Ian Haygood; you both know how much you have done for me; thank you! Also friends Kevin Gamble and Renee Scholman; your support can be felt all the way in Colorado. Last, but definitely not least, my friend and editor Jesse Skene. You have literally helped with every word I have ever published, my endless thanks. Couldn't have done it without you.

Contents

List of Tables

List of Figures

1 Introduction

1.1 Background and Motivation

The work presented in this dissertation originated as an effort to measure the electron paramagnetic resonance (EPR) signatures of magnetic nanoparticles suspended in fluids [1] (discussed in detail in Section 6.1). This research was based on a substantial body of work in which the ferromagnetic resonance (FMR) of magnetic films and powders [2–7] was measured with a combination of coplanar waveguides (CPWs) and vector network analyzers (VNA). This same CPW-VNA approach has been separately employed to measure the dielectric properties of fluids [8–15]. Here, we expand and improve upon the CPW-VNA measurement technique to study fluids with both magnetic and electric properties in microfluidic channels.

In the CPW-VNA-based measurement, samples are placed directly over CPW structures and measured using a VNA. CPWs consist of three sections of metallization (center-conductor, and two ground planes), patterned on top of a dielectric substrate (Figure 1).

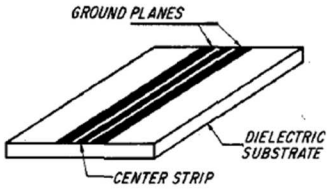

Fig. 1. Coplanar waveguide (CPW), a surface strip transmission line.

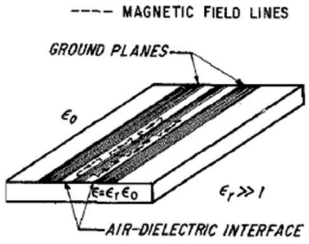

Fig. 2. RF magnetic field configuration in a CPW.

Figure 1. Diagram of a coplanar waveguide (CPW). Image from C.P. Wen's original 1969 article introducing the concept of the CPW [16].

CPWs are similar to coaxial cables, in which the electromagnetic fields are contained between the center-conductor and grounds. The planar geometry of the CPW means that the electromagnetic fields partly extend out from the CPW surface, into the dielectric substrate and into the open air above the waveguides. This means that the CPWs are extremely sensitive to the electromagnetic properties of any materials placed in close proximity to the surface of the CPW. This characteristic makes CPWs well suited to electromagnetic metrology. The electromagnetic properties can be determined through calibrations and analysis of raw VNA measurements. The VNA delivers and monitors the microwave power reflected from and transmitted through the CPW. Changes in the microwaves absorbed and dispersed by the material can be related to its electromagnetic properties through a process that will be explained in this dissertation.

Determining how to design and fabricate CPW-based devices and to analyze data to accurately extract the electromagnetic properties of material is the core scientific focus of this dissertation. More concretely, we are interested in creating integrated microwave microfluidic devices, and understanding

how raw VNA measurements can be quantitatively related to fluid properties. Dried powders and films in both FMR and dielectric spectroscopy are relatively easy to measure, and an extensive literature exists on measuring these solids [4,5,17]. Fluids, on the other hand, pose some additional measurement challenges including higher dielectric losses and difficulties with sample confinement [18,19]. The measurement technique has previously been limited to solid materials, applicable mainly to materials science; the ability to measure fluids widens the applicability to biological material metrology. We also show the importance of microwave calibrations in accurately extracting quantitative information from the CPW-VNA measurement.

1.1.1 Broadband vs. Resonator-based EPR

We begin with a look at the CPW-VNA approach as applied to EPR and FMR*. Resonator cavity-based EPR systems are a common, useful tool in the chemist's arsenal. Unlike the broadband CPW-VNA method, resonator cavities operate at a single frequency; measurements made at multiple frequencies require time-consuming retuning. These systems rely on sweeping across a magnetic field to capture the sample's magnetic resonance; the field-sweeping approach is also common in FMR measurements. However, because cavity-EPR systems are inherently narrow-band, they cannot easily discern important

* The line separating EPR from FMR is somewhat blurry. Both phenomena result from the magnetic resonance of electrons (spins). EPR deals with anything from isolated spins (as in radical molecules), to a collection of spins in a single domain (as in a superparamagnetic nanoparticles). The FMR response occurs when there exists domain wall movement or spin waves, typical for magnetic films.

frequency-dependent parameters such as the magnetic dampening coefficient or anisotropy distribution of samples. However, knowing this information is important in measuring FMR films. Fortunately, FMR films have a strong response that compensate for the broadband approach's poor signal-to-noise [20]. The strong response can reduce the need for microwave calibrations, which is why they are rarely performed in FMR.

However, to the author's knowledge, proper microwave calibrations have yet to be applied to broadband CPW-VNA-based EPR measurements. There is a common misconception that performing microwave calibration cannot increase the sensitivity of field-swept measurements. Signal distortions, caused by mis-calibration, are commonly lumped in with random noise. Proper calibrations can eliminate these distortions, effectively increasing measurement sensitivity, as well as leading to quantitative measurements. There is still a fundamental limit to the sensitivity of the broadband approach, and it has yet to be determined whether this sensitivity level will be sufficient for real-world applications.

Frequency and magnetic field-swept measurements are often seen as mutually exclusive. However, fully calibrated broadband measurements allow for the combination of frequency and magnetic field sweeps, mapping the total response. This combined technique not only yields deeper insight into the magnetic response of the material, it also allows simultaneous differentiation of its electrical response. The ability to probe both the electric and magnetic response simultaneously is applicable to composite materials that have both electrical and magnetic parts, such as ferrite-piezoelectric composites [21] and many biological samples.

1.1.2 Medical Applications

Dr. James Booth, of the National Institute of Standards and Technology (NIST), has already made substantial progress in developing microfluidic devices and calibration schemes for on-chip fluid

metrology [11,12]. In addition to removing signal distortions, Booth's calibration methods render quantitative measurements of the complex permittivity (electrical response) of the fluids. In this dissertation, we will also extend this method to quantitative measurement of the permeability (magnetic response) of various fluids. Measurements of both permittivity and permeability are components of the broader category of complex impedance spectroscopy.

The author anticipates application of these techniques in cytometry (measurement of cell properties), and whole blood analysis. Microfluidic devices have repeatedly proven their efficacy in handling cells [22–24] Additionally, impedance spectroscopy has long been used to measure biological tissues and cellular properties [25–29]. In fact, the first demonstrations of the existence of the cell membrane were based on dielectric studies of cell suspensions [30].

As a general rule, any physical change in the pathology of a cell will also manifest as a measurable change in impedance. Even without a first-principle connection between the physical changes in the cell and changes in impedance, impedance changes can be statistically correlated with changes in cellular pathology. This method is known in the medical community as diagnostic correlation. In cytopathology, the diagnosis of diseases using cellular analysis is referred to as cytologic-histologic correlation [31]. A combination of assays for a disease increases the collative power of the diagnosis.

Malaria is a quintessential application for the on-chip broadband measurement technique: according to the World Health Organization, Malaria is among the top 10 causes of death in humans[32]. Blood smears are the standard for malaria diagnosis. [33] Blood smears rely on imprecise visual analysis of blood. Other diagnostic tools, such as immunofluorescence of Malaria antibodies and DNA detection, exist. However, these alternative methods are expensive, time consuming, and have shown little success. Microfluidic-based impedance measurements have already been used to specifically distinguish malaria-

infected cells from healthy cells [34]. In addition to having a distinct electrical response, malaria, like many other microorganisms, also has a distinct magnetic response. The magnetic response reflects the organism's concentration of biogenetic iron, a naturally-occurring paramagnetic particle, called a hemozoin, also referred to as malarial pigment [35]. Not only do the hemozoin crystals produce a strong magnetic resonance signal to aid in the detection the parasite, the exact shape of the resonance response speaks to the shape of the crystal, which is unique to each species of Malaria [35–37]. Knowing which species a patient is infected with will help to determine risk and treatment [32].

To further highlight the importance of developing more effective ways of diagnosing Malaria, we note that the Gates Foundation awarded a 2003 grant for "Single-Cell EPR Sensors for Rapid Diagnostic Tests of Malaria[†]," in 2012, and another grant for "Ultra-Sensitive Non-Invasive Point-of-Care Immunosensor for Malaria[‡]" in 2016. The second metrology technique detects malaria based on changes in electrical impedance caused by the binding of two molecules.

The higher frequency range afforded by the calibrations gives additional and quantitative data compared with traditional impedance spectroscopy. Combing EPR-based diagnostics with electrical impedance-based diagnostics can also greatly increase the total diagnostic power of the measurement. In addition, microfluidics allows for compact devices for point-of-care applications and increase sample throughput, which is important for increasing the accuracy of parasitemia estimations (statistical number

[†] http://gcgh.grandchallenges.org/grant/single-cell-epr-sensors-rapid-diagnostic-tests-malaria

[‡] http://gcgh.grandchallenges.org/grant/ultra-sensitive-non-invasive-point-care-immunosensor-malaria

of parasites in the blood). Due to the laminar environment of microfluidics, we are able to perform repeated measurements on the exact same volume of sample, or even the exact same cell [38].

1.1.3 Measuring Standard Reference Materials

The majority of this work was conducted at NIST, which operates under the mission statement "to promote U.S. innovation and industrial competitiveness by advancing measurement science, standards, and technology in ways that enhance economic security and improve our quality of life [39]." In addition to advancing fabrication methods and measurement techniques, we want to use these highly accurate techniques to measure fluids pursuant to NIST's goal of improving standards.

Having accurate and precise measurements of the permittivity and permeability of materials in the lab setting impacts real work measurements, an example of which is satellite remote sensing. As the earth warms, most of that heat energy is trapped in the oceans, due to the high heat capacity of water. Precisely knowing the extent of ocean temperature rise is a key quantity in climate change models [40]. Satellite-based remote sensing over the oceans is the primary method of measuring sea temperature rise. Accurate and precise determinations of the ocean salinity and temperature are based on accurate and precise knowledge of the permittivity of seawater [41], which can only be established in a carful lab setting.

1.2 Research Goals

1 Develop the fabrication processes and designs for an integrated microfluidic-microwave platform to measure the electric and magnetic properties of small fluid volumes, on the order of nano-liters. A sub-goal is to reduce the size and complexity of devices for medical point-of-care applications.

2 Develop an on-chip calibration protocol that allows for broadband measurements of fluid-loaded microfluidic channels between DC and 100 GHz.

3 Establish the relationship between the distributed circuit parameters extracted from the calibration and the intrinsic permittivity and permeability of the fluid.

4 Correlate the shape of the measured fluid permittivity and permeability spectra to physical properties, including ionic effects like the electrical double-layer, dipolar relaxations, and magnetic resonances.

1.3 Organization of Dissertation

The remainder of the dissertation is organized into chapters, where the subsections of each chapter are referred to as *sections*: Chapter 2 gives a brief primer on permeability and permittivity phenomena as well as covering relevant microwave calibration theory. Chapter 3 will cover the design and fabrication of our devices, and includes information on the calibration protocol. Chapter 4 covers how finite element simulations can be used to map measurements to permittivity and permeability. Chapter 5 and Chapter 6 concern published work on the modeling of electrical double-layer effects, followed by work on measuring the magnetic resonance of magnetic nanoparticles. In Chapter 6 we will also discuss ongoing work concerning the relationship between electrical and magnetic effects in broadband CPW measurements. Finally, in Chapter 7, we summarize and discuss future research. Supplementary information is contained in the Appendices, following Chapter 7. Appendix A, discusses our work on SU-8 process development.

1.4 Summary of Resultant Publications

Two first author publications and several related second and third author publications have resulted from this research. The beginnings of this research focused on magnetic resonance measurement

of magnetic nanoparticles on CPW lines. The publication that resulted from this work, "On-wafer magnetic resonance of magnetite nanoparticles", was published in the *Journal of Magnetism and Magnetic Materials* [42]. In the second publication, microwave calibrations were used to study electrical double-layer effects in ionic fluids. The resultant paper, "Modeling electrical double-layer effects for microfluidic impedance spectroscopy from 100 kHz to 110 GHz", was published in *Lab-on-a-Chip* [15].

In addition, I have been involved in three other microwave calibration papers, which laid the groundwork for the calibrations and procedures discussed throughout this dissertation. Two articles have already been published [13,43] by Dr. Song Liu. The third article, a collaboration with Xiao Ma, has been accepted and is in press, titled "A Multistate Single-Connection Calibration for Microwave-Microfluidics".

Lastly, over the course of this research we also development a fabrication procedures to create rigid, fully encapsulated devices. This work resulted in microfluidic devices that were used in research measuring shear-banded fluids contained in microfluidic channels, entitled "Jetting of a shear banding fluid in rectangular ducts", published in *Physical Review Fluids* [44].

2 Theory Primer

This chapter presents a general introduction to the physics, history, and methods underlying broadband microwave spectroscopy. The chapter gives the background necessary to understand the work presented in the following chapters. The information contained in this chapter is meant as a primer to prepare the reader to understand the research containing in the rest of the dissertation. We start with a general background explaining the origins of microwave technology as it relates to microwave spectroscopy. Finally, we cover the basics of microwave calibrations, necessary for extracting quantitative information from our measurements.

2.1 History of Microwave Technology

The definition of what constitutes "microwave" frequencies is somewhat arbitrary, but here we define microwaves as the electromagnetic regime between 300 MHz and 300 GHz. Measurements presented in this dissertation also go well below 300 MHz, into the radio frequency regime.

Low frequency, non-visible, electromagnetic (EM) waves, i.e. radio and microwaves, were first theorized by James Clark Maxwell in 1865 [45], and later generated and detected by Heinrich Hertz in 1887 [46]. Radio waves were revolutionary, as they were the first type of EM radiation that could be generated and detected solely through electrical circuitry, yet existed on the same continuum as visible light. Higher frequency microwaves can also be created with electrical circuitry but require more advanced electrical engineering than radio waves. Developed in the early 1900s, the cavity magnetron and klystron were the first devices capable of emitting microwaves. In magnetron and klystron devices, a combination of free vacuum electrons and various electrical and magnetic potentials are used to set up resonances at microwave frequencies. Modern solid-state alternatives to generating microwaves include field-effect transistor (at lower frequencies), tunnel diodes, Gunn diodes, and IMPATT diodes [47]. After World War II, klystrons were used to create a network of microwave relays that allowed for mass telephone communication across the US. In the current era, communication has proven to be among the most important and lasting applications of microwave technology.

Microwaves can also be used to interrogate materials in a manner similar to visible light. When electromagnetic properties are measured over a continuous broadband frequency range, this is known as spectroscopy. The way that electromagnetic waves interact with a given material determines the resulting spectrum. Conversely, spectra can be used to infer material characteristics. Although historically the term "spectroscopy" was primarily used to describe the study of the visible light, it also applies to the microwave regime. For the frequency range we are concerned with, the broadband measurement is

sometimes referred to as impedance or dielectric spectroscopy, at radio and microwave frequencies, respectively. In addition, nuclear and electron resonances also present in the radio and microwave wavelengths, and therefore we could also refer to the measurements as permeability or magnetic resonance spectroscopy, depending on if the material is magnetic or not. We will use all these terms interchangeably throughout this dissertation.

2.2 Permittivity and Permeability

2.2.1 DC Permittivity and Permeability

Our goal in this research is to connect microwave measurements to the inherent electrical and magnetic properties of a material, which can then be correlated to physical properties. A material's electrical and magnetic response is represented by two complex quantities known as permittivity (ε) and permeability (μ), which represent materials "compliance" to the electric and magnetic fields, respectively.

In the static case (which we refer to as DC for direct current, i.e. zero frequency), when an electrical field is applied to a substance containing polar molecules such (e.g. water), the collection of molecules tends to align with the external electric field. The individual dipole moments of the water molecules add together to contribute to the total field. The same is true for magnetic moments. In the DC case, ε and μ are simple proportionality constants.

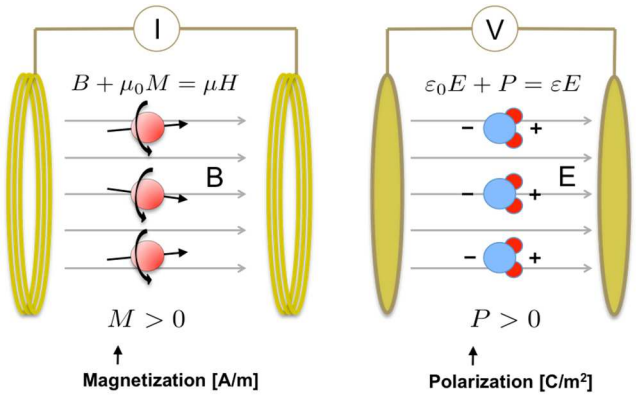

Figure 2. Static permittivity and permeability can be thought of as proportionality constants relating the applied field to the total field.

2.2.2 AC Permittivity and Permeability

In the non-static case, where materials are interrogated with alternating (AC) EM fields, the situation is more complex. In AC measurements, permittivity and permeability are complex quantities ($\epsilon = \epsilon' + i\epsilon''$ and $\mu = \mu' + i\mu''$). The imaginary part of ε and μ correspond to power loss in the material. The greatest energy loss, resulting in the greatest heating, occurs when the charges or spins are moving at the same rate as the applied AC field. For water, this frequency is around ~20 GHz at room temperature.

The speed at which an ideal EM wave travels through a medium is determined by ϵ and μ ($v = 1/\sqrt{\epsilon\mu}$). In a vacuum, these quantities have finite values, which are the permittivity and permeability of free space respectively ($\epsilon_0 \approx 8.854\text{x}10^{-12}$ [F m^-1] and $\mu_0 \approx 1.257\text{x}10^{-6}$ [H m^-1] [48]). It is common practice to normalize permittivity and permeability values by dividing by their vacuum quantities ($\epsilon_r = \epsilon/\epsilon_0$ and $\mu_r = \mu/\mu_0$), known as relative permittivity and permeability.

The full complex permittivity landscape stretches from DC past ultra-violet (UV) frequencies (Figure 3). Changes in the permittivity at lower frequencies (DC to ~300 MHz, radio frequencies) relate primarily to electrical conduction effects, i.e. ionic charge movement or, in metals, electron movement. In

the microwave regime (300 MHz to 300 GHz), we get dipolar relaxations. In the IR and Visible wavelengths, permittivity changes come from atomic resonances, i.e. vibrations of atomic bonds. In this dissertation, we will investigate the permittivity and permeability spectrum between DC and high frequency microwaves (100 GHz).

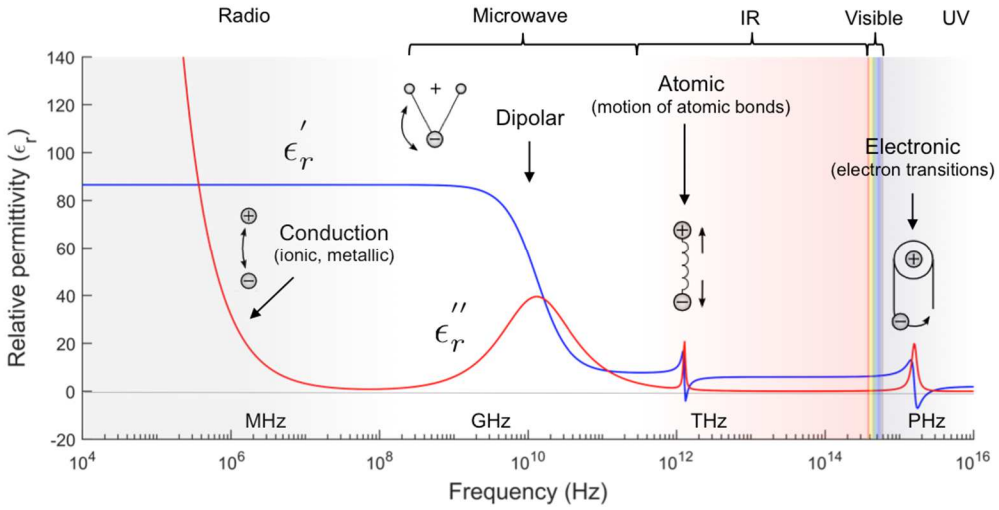

Figure 3. Complex permittivity spectrum with real permittivity (ε′) and imaginary permittivity (ε″).

2.2.3 Resonance Phenomena

In order to interpret phenomena in the complex permittivity spectrum we need to understand resonance and relaxation phenomena. Resonances describe systems with classical restoring and damping forces whereas relaxations describe systems that use random thermal motion to return to equilibrium. Resonances were first described mathematically by Hendrik Antoon Lorentz, a Dutch physicist, in the late 19th century [49]. Lorentz derived the electromagnetic Lorentz force and Lorentz transformations, later used

by Albert Einstein to develop Special Relativity[§]. The model for Lorentz' classical theory of resonances (1878) consists of an atom with a positively charged nucleus, surrounded by a negatively charged cloud. The concept of the electron as a particle did not come about until J. J. Thomson discovered the electron in 1897 [50].

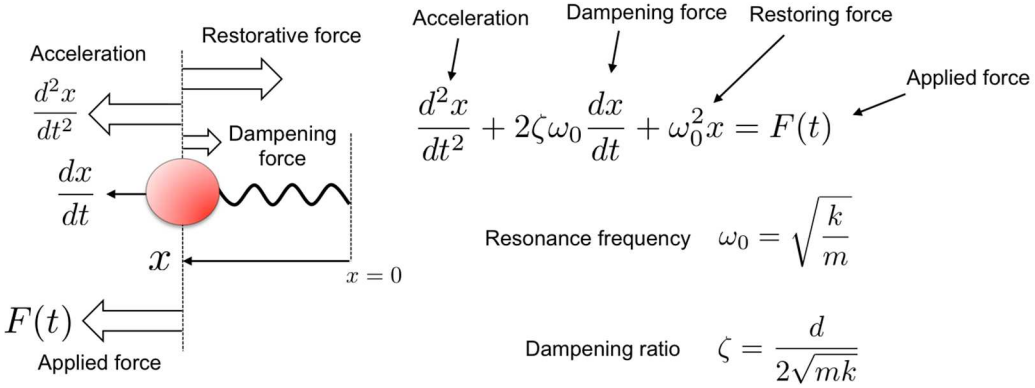

Equation 1. Simple dampened harmonic oscillator, with the natural/fundamental frequency (ω_0) and the dampening coefficient (ζ).

Lorentz resonance is based on the simple harmonic oscillator (SHO) model (Equation 1). Lorentz proposed that the negatively charged electron cloud is bound to the positively charged nucleus of the atom by a force that behaves according to Hooke's law. Hooke's law states that the restoring force is proportional to the displacement ($F = kx$, where x is the displacement, k is the spring constant, and F is the applied force) [49]. In dielectrics, the displacement relates to the polarization (P); in magnetic materials

[§] Lorentz also shared the 1902 Nobel Prize in Physics with Pieter Zeeman for the discovery and theoretical explanation of the Zeeman effect, the basis of magnetic resonance.

it relates to magnetization (M). In the electrical polarization case, the applied force is determined by the strength of the applied electric field (E):

$$\frac{d^2}{dt^2}P + \gamma\frac{d}{dt}P + \omega_0^2 P = \frac{Nq_e^2}{m}E(t),$$

Equation 2. Harmonic osilator system applied to electrical polarization.

where γ is the dampening ratio, ω_0 is the resonance frequency, N is the number of charges, q_e is the charge of the electron, and m is the mass of the electron. Solving Equation 2 yields an expression for complex permittivity:

$$\epsilon_r(\omega) = 1 + \frac{\omega_p^2}{(\omega_0^2 - \omega^2) + i\omega\gamma}, \quad \omega_p = \sqrt{\frac{Nq_e^2}{m\epsilon_0}},$$

Equation 3. Complex Lorentz resonance equation for relative permittivity.

where ω_p is the plasma frequency.

The resonance response has three important regions: below resonance (1: transmissive), at resonance (2: absorptive), and above resonance (3: reflective). A helpful metaphor for understanding resonance behavior involves a child on a swing (Figure 4), another physical example of the SHO. Below the resonance frequency, when pushing the child very slowly, the child can swing only to the extent of your reach; the motion of your arms is in phase with the motion of the child. The length of your reach in this analogy corresponds to the magnitude of the DC permittivity, i.e. far below the resonance frequency. As the swinging child approaches resonance frequency, she is able to swing higher and higher, past your arms. This is the frequency at which you are most efficiently transferring your pushing energy to the stored energy of the swinging child, which eventually is lost as heat through friction and air resistance. Analogously, we see a peak of loss (imaginary permittivity) at the resonance frequency, where the energy can be lost through a verity of means including phonon transfer [51]. At this frequency, your pushing is 90°

out of phase with the child's motion, driving the real part of the permittivity to zero. At a frequency well above the resonance frequency of the child, your arms are moving so fast that they no longer transfer energy to the swinging motion of the child; you are, in essence, shaking the child. Here, the motion of your arms is completely out-of-phase (180°) with the motion of the child. Above the resonance, real and imaginary parts of the permittivity both go to zero.

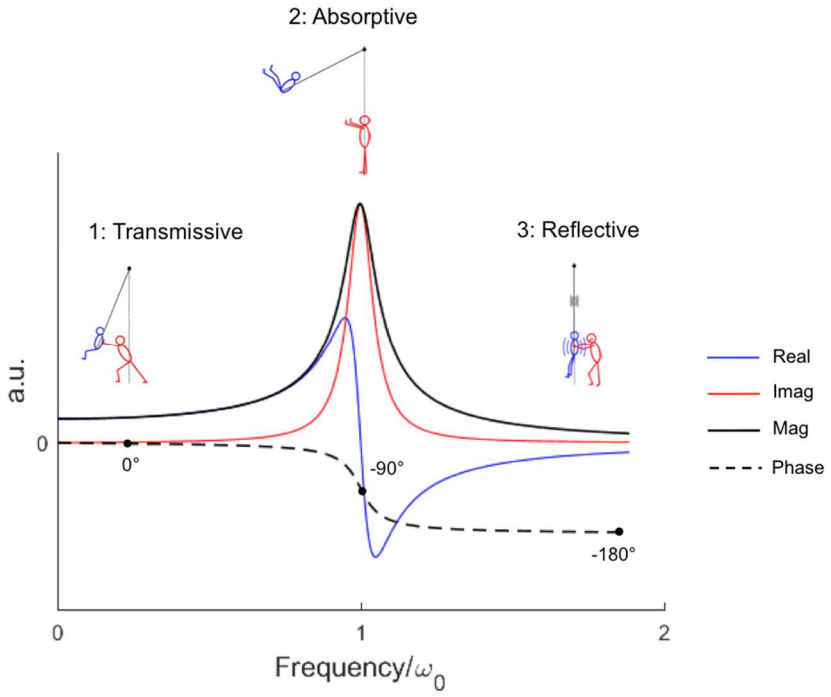

Figure 4. Plot of Lorentzian resonance

Where electrons are free to move through a conductor, as would occur in an infinite metal, there is no restoring force. In 1900, Paul Drude proposed this concept, now referred to as the Drude model. He pictured the conductor as a "sea of electrons" [5049]. The Drude model and the Lorentz model are mathematically interrelated, and are often lumped together as the Drude-Lorentz model. The Drude model of electrical conduction can be derived from the Lorentz equation. No restoring force translates as a negligible spring constant ($k = 0$) in the SHO model, or as a resonance frequency of zero in a Lorentz resonance. This results in the following equation:

$$\epsilon_r(\omega) = 1 + \frac{\omega_p^2}{\omega^2 + i\omega\gamma}$$

Equation 4. Drude model for the relative permittivity of a conductor.

2.2.4 Relaxation Phenomena

Relaxation behavior is distinctly different from resonance behavior, the result of stochastic randomizing thermal processes. In 1912 [52], Peter Debye devised a model for the anomalous dispersion phenomenon seen in dipolar dielectrics like water. Inspired by Einstein's theory of Brownian motion, Debye came up with the Debye relaxation equation [53] (Figure 5) to explain dipolar relaxation, where ϵ_{DC} is the permittivity of the material at zero frequency (DC), and τ is the relaxation time constant. This work was published in 1929 [54], for which he was awarded the Nobel Prize in Chemistry in 1936 [55].

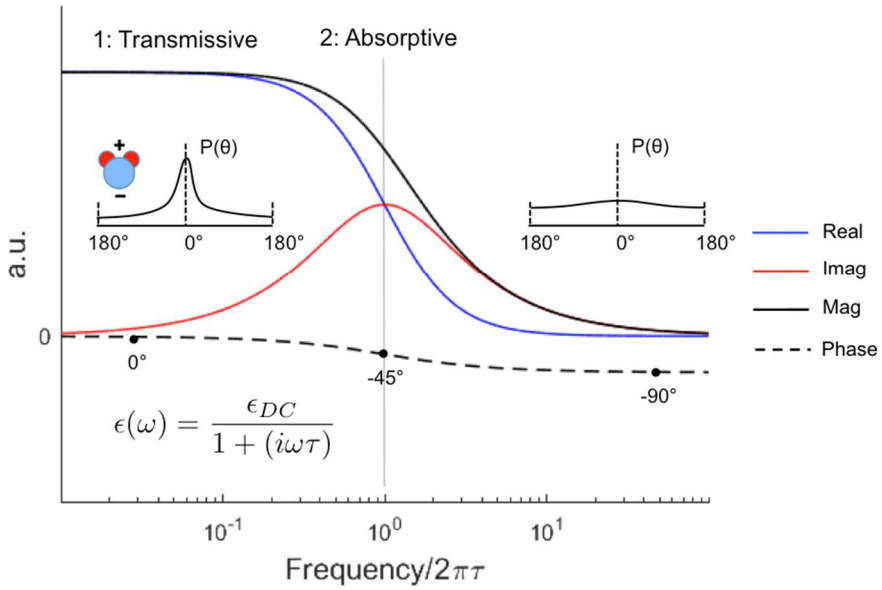

Figure 5. Plot of a Debye-type relaxation.

In formulating the relaxation equation, Debye pictured isolated water molecules in a bulk volume (Figure 5). He ignored the interaction between water molecules, focusing on the free rotation of the molecules. Due to their polar nature, water molecules tend to align with an applied electric field. This

creates a net polarization in the bulk fluid. Debye considered what would happen if the electric field were instantaneously deactivated. In this case, random thermal motion would tend to randomize the orientation of the molecules, "relaxing" the total polarization of the bulk collection of water molecules (Figure 5).

The Debye equation was not completely sufficient at fitting empirical data. Equations, such as the Cole-Cole equation [56] (Equation 5) and Havriliak–Negami equation [57], describe a distribution of Debye relaxations. A distribution of relaxation times is more consistent with reality, where there is often a distribution of physical properties. We will use the Cole-Cole equation for describing the Debye-type relaxation of water and electrode polarization effects in Chapter 5. The exponent α in the Cole-Cole equation (Equation 5) expresses how closely a given relaxation conforms to the Debye model, where ϵ_∞ in Equation 5 is the permittivity far above the relaxation frequency.

$$\epsilon(\omega) - \epsilon_\infty = \frac{\epsilon_{DC} - \epsilon_\infty}{1 + (i\omega\tau)^{1-\alpha}}$$

Equation 5. The Cole-Cole equation.

The Cole-Cole equation has been repeatedly shown to fit measured data [12,56,58]. Although the Debye and Cole-Cole equations are based on a specific physical model for the dielectric relaxation of water, the physical mechanism for this relaxation remains controversial (see Appendix-B).

2.2.5 Magnetic Resonance and Relaxation

We now have a framework in which to understand electrical effects in materials. However, when measuring materials at radio and microwave frequencies, we must also consider the magnetic response of the material. In these frequencies, both nuclear and electron resonance can occur. Nuclear magnetic resonance (NMR), the basis for magnetic resonance imaging (MRI), operates at frequencies on the order of MHz; electron paramagnetic resonance (EPR) and ferromagnetic resonance operate at frequencies on the order of GHz. Magnetic effects are relevant to our research because they must be accounted for in

measurement, and because they provide additional information that can be combined with electrical effects for a more complete picture of the underlying physical phenomena.

Material magnetism originates from the protons and electrons within atoms. The combination of quantum charge and quantum spin results in a magnetic dipole moment, which is often referred to as "spins", essentially subatomic magnets. Bulk material magnetism originates from the collective magnetism of individual protons and electrons within the material, with substantial quantum-mechanical caveats [59].

Magnetic dipole moments (spins), like their electrical equivalents, tend to orient to an external field, however, the property of spin adds additional complexity. When an external and constant magnetic field (B_0) is applied to a spin, and the spin is then perturbed with an instantaneous orthogonal magnetic field (B_1), the spin will display processional motion. The frequency of the procession is proportional to the strength of B_0, called the Larmor frequency. Processional motion decays as processional energy is lost to the environment. A time-varying magnetic field applied at the Larmor frequency (ω_L) equates to the magnetic resonance frequency (ω_0). The strength of the DC magnetic field is commonly referred to as B_0 and the strength of the AC magnetic field as B_1 in nuclear magnetic resonance (NMR) and electron paramagnetic resonance (EPR) (Figure 6).

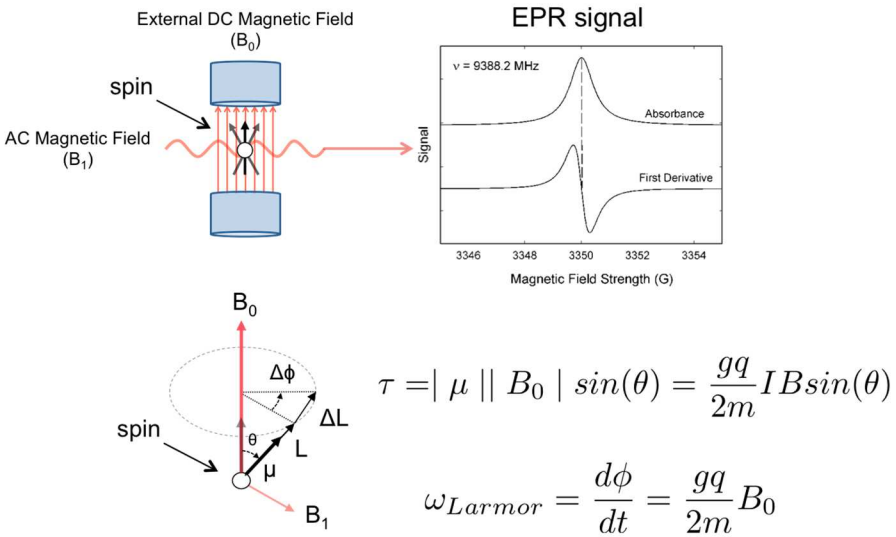

Figure 6. Explanation of paramagnetic resonance

The response of spins combines relaxation and resonance behaviors. Figure 7 has equations for the Debye relaxation and Lorentzian resonance behaviors of a magnetic dipole. The strength of the relaxation of the magnetic moment, and thus its contribution to the total permeability is small and broad relative to the effect of resonance behavior; the relaxation response is therefore often ignored.

Debye relaxation
parallel to B_0

$$\chi'_{\mu\parallel}(\omega) = \chi_{\mu\parallel}(\infty) + \frac{\chi_{\mu\parallel}(0) - \chi_{\mu\parallel}(\infty)}{1 + \omega^2\tau_\mu^2}$$

$$\chi''_{\mu\parallel}(\omega) = \frac{(\chi_{\mu\parallel}(0) - \chi_{\mu\parallel}(\infty))\omega\tau_\mu}{1 + \omega^2\tau_\mu^2}$$

Lorentzian resonance
perpendicular to B_0

$$\chi_\perp(\omega)'' = \frac{\alpha\gamma M_s\omega_0[\omega_0^2 + \omega^2(1+\alpha^2)]}{[\omega_0^2 - \omega^2(1+\alpha^2)]^2 + 4\omega^2\omega_0^2\alpha^2}$$

$$\chi_\perp(\omega)' = \frac{\gamma M_s\omega_0[\omega_0^2 - \omega^2(1-\alpha^2)]}{[\omega_0^2 - \omega^2(1+\alpha^2)]^2 + 4\omega^2\omega_0^2\alpha^2}$$

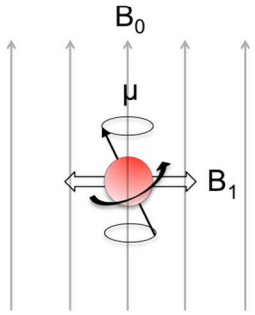

Figure 7. Complex components of Debye relaxation and Lorentzian resonance for a single isolated spin.

2.3 Waveguide Theory and Permittivity Spectroscopy

This section is about the general methods underlying microwave measurements. All the microwave devices used in this body of work are based on concepts covered in this section. We employ coplanar waveguides (CPWs) to perform broadband microwave measurements. In many types of EM spectroscopy, waveguides can be used to direct waves to the material under interrogation, without signal distortion or excessive energy loss. There are two primary categories of waveguides: waveguides based on a dielectric mismatch (i.e. fiber-optics or dielectric waveguides), and waveguides that confine EM fields with a conductive material (i.e. rectangular waveguides, coaxial waveguides, etc.). This type of waveguide is more practical for low-frequency electromagnetic waves like radio and microwaves.

To create and detect microwaves we used a vector network analyzer (VNA) (an introduction to VNAs can be found here). The VNA emits and receives microwaves, often as a function of frequency, between two coaxial connections. Connections are referred to as *ports,* and using two connections is referred to as a *2-port measurement*. The VNA measures both the relative amplitude and phase of the microwave, relative to the initial wave outputted by the VNA. The VNA can be connected to our planar waveguides via coaxial cables and movable microwave probes. Waves are able to travel bi-directionally through the section of waveguide that we wish to measure, referred to as the *device-under-test* (DUT). The VNA specifically measures the ratio of wave voltages transmitted and reflected to and from the DUT, reporting this information as a 2x2 matrix of complex scattering parameters (S-parameters) (Figure 8). S-parameters are the starting point for our microwave calibrations and measurements.

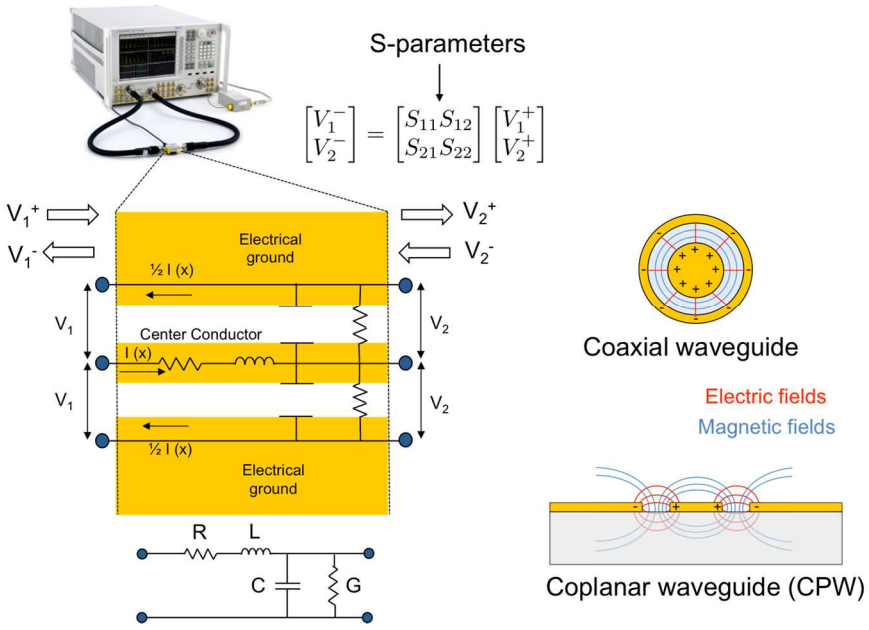

Figure 8. Diagram of broadband measurments.

The distributed circuit model reduces the electrical properties of any homogeneous section of waveguide to the equivalent circuit in Figure 8. This circuit consists of four per unit length (PUL) circuit elements: series resistance (R), series inductance (L), parallel capacitance (C), and parallel conductance (G). These elements are collectively known the distributed circuit parameters (RLCG). The electrical and magnetic response of a homogeneous section of waveguide is described by two parameters: impedance (Z) and the propagation constant (γ). RLCG can be derived from Z and γ (Figure 9). RLCG for the waveguide section can then be related to the complex ϵ and μ of any material within that section (Figure 9).

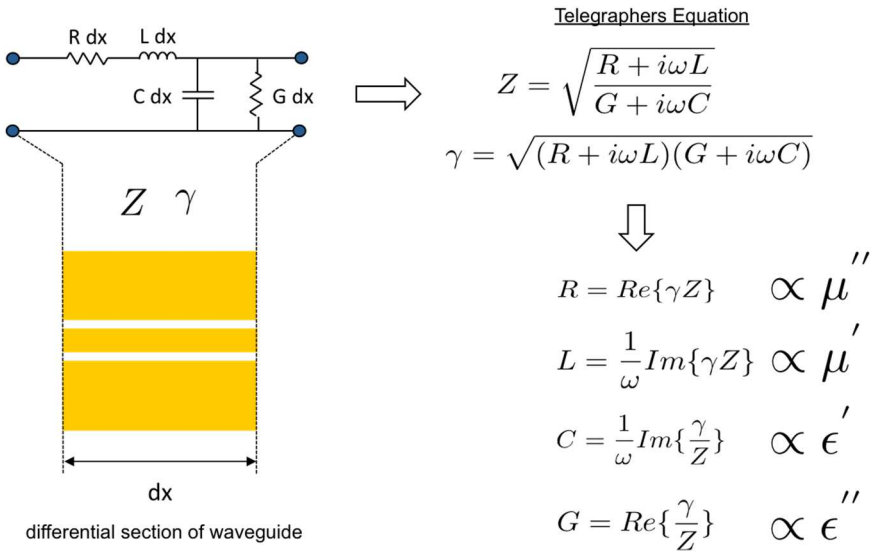

Figure 9. Impedance (Z) and propagation (γ) constants describe the electrical and magnetic response of a homogeneous section of waveguide. Z & γ translate to distributed circuit parameters R,L,C, and G, which relate to the effective ϵ & μ.

Impedance (Z), coined by Oliver Heaviside in 1889 [60], describes the complex resistance to AC currents. Impedance is related to the material's complex permitivity, and so the terms impedance spectroscopy and permitivity spectroscopy are interchangeable. Determining a material's permittivity and permeability via spectroscopy requires accounting for the phase and magnitude of microwaves transmitted to and from that material. In optical spectroscopy, this information yields the index of refraction (n) and wavenumber (k), which then relates to ϵ and μ. In refraction, light is both reflected and transmitted at interfaces between two dielectric materials with dissimilar values of n. By measuring the ratio of light reflected at an interface, the index of refraction of the second material (n_2) can be determined from the index of refraction of the first material (n_1) (Figure 10). The concepts of index-of-refraction and impedance are interrelated concepts. By measuring the ratio of reflections (R) off an interface between a reference and un-known section of waveguide, we can determine the impedance of the unknown section of waveguide (Figure 10). This premise appears clearly in time domain reflectometery (TDR) [61], which uses pulses instead of continuous waves.

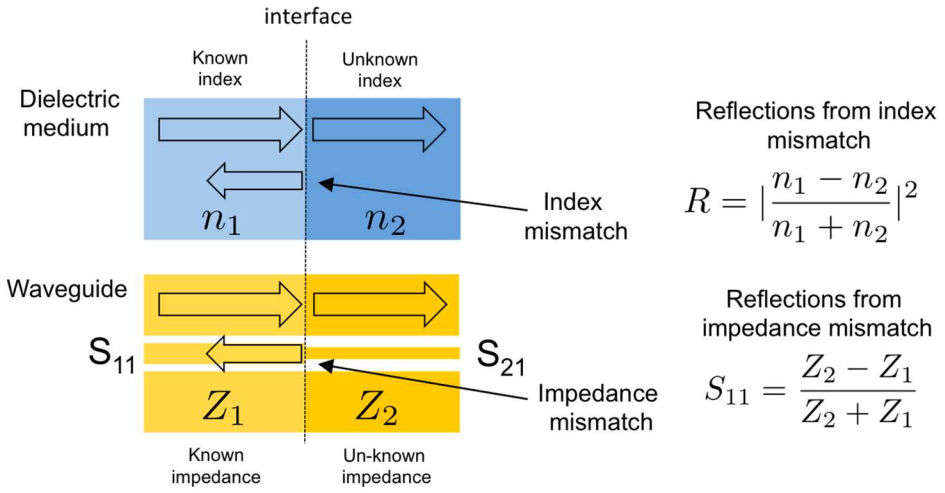

Figure 10. Analogy between index-of-refraction (n) and electrical impedance (Z).

The propagation constant (γ) on the other hand describes how a wave changes with distance through any homogenous medium, such as a homogenous section of waveguide. Like impedance, the propagation constant is a complex number. The real part of γ, known as the attenuation constant (α), describes how much power is lost as the wave travels. The imaginary part of the propagation constant, known as the phase constant (β), describes how much phase change is occurring. When measuring a section of waveguide with a VNA we can extract γ directly from the measured S-parameters (Figure 11).

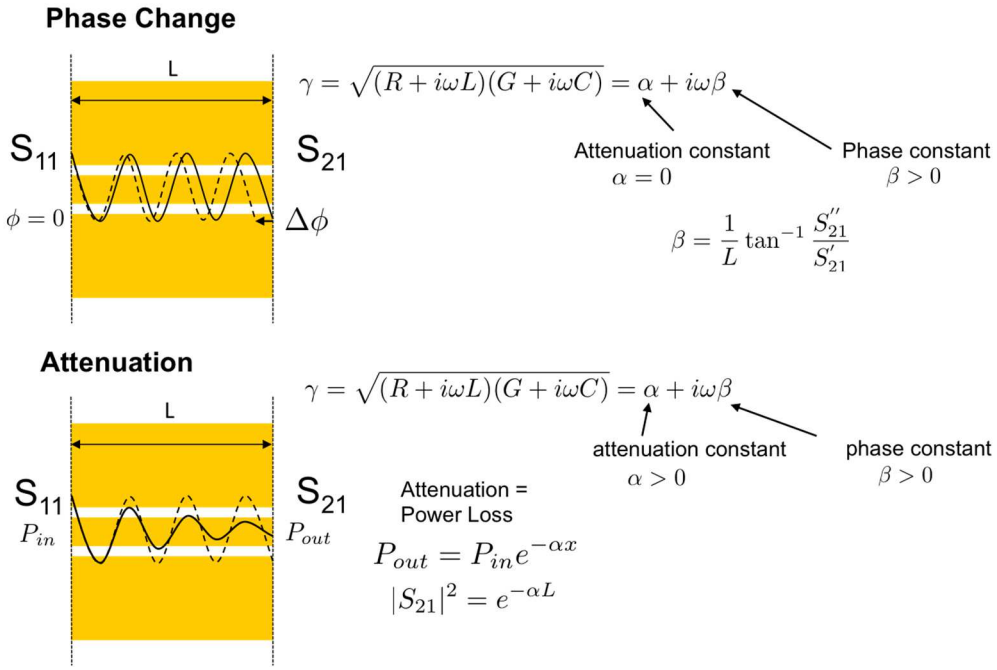

Figure 11. Determining the propogation constant (γ)

2.4 Microwave Calibrations

In our explanations in Section 2.3 on measuring the impedance and propagation constant we were assuming that the S-parameters are measured directly at each end of our waveguide. The section of waveguide being measured is often referred to as the device-under-test (DUT). In reality, there are cables, connectors, and other components between the DUT and the VNA. Any slight differences or gap between interfaces results in impedance mismatches (Figure 10), creating reflections and resonances, distorting the measured S-parameters. In addition, each length of line along the path might have significant attenuation and phase change over the length. The purpose of preforming calibrations is to account for these extraneous factors that distort measurements of the DUT.

This following section introduces microwave calibrations and gives some basic information about the specific calibration used in this work. Microwave calibrations are both a science and an art. Different types of calibrations may be more appropriate in different situations or at different frequencies.

2.4.1 T-matrix Cascade and De-embedding

The S-parameters that result from VNA measurements form a complex matrix that described the microwave response of the entire system, from one VNA port to the other VNA port. There are a number of matrix formalisms used to describe VNA measurements, including the impedance matrix method, admittance matrix method, or ABCD matrix method [62]. In this work, we elected to use transfer parameter matrices (T-matrices). The S-parameters we measure can be directly translated into a T-matrix (Figure 12). The T-matrix for the total VNA measurement (T_M) can be formed from a cascade of T-matrices, where each T-matrix describes a different section of waveguide or interface between waveguide sections. The T-matrix for a homogeneous waveguide section can be described using the propagation constant alone (Figure 12). Impedance is important where the wave transitions from one waveguide section (with one impedance) to another waveguide section (with a different impedance). These transitions in impedance are called impedance mismatches, where reflections occur. Impedance mismatches can be described with another T-matrix, called the *impedance transformer* (Figure 12), using the notation $Q|_B^A$, where A is the impedance of the left section of waveguide, and B is the impedance of the right section of the waveguide. If we have the measured T_M and the impedance of the waveguide (characteristic impedance) leading up to the DUT (Z_0), we can than determine the impedance of the DUT itself. For historical and practical reasons, most microwave equipment is standardized at an impedance of 50 Ω.

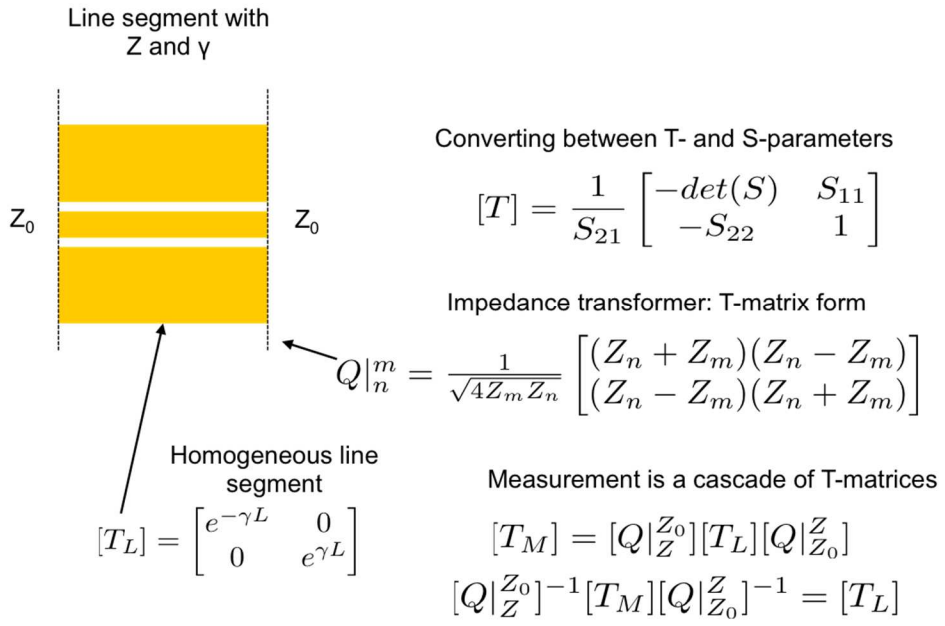

Figure 12. Description of a transmission line segment with T-matrices.

Essentially, when we do a microwave calibration, we are mathematically converting raw S-parameter measurements to simulate measurement directly at the DUT (sample). In microwave science parlance, this is known as *de-embedding* the measurement to the *reference planes*. De-embedding is the process of calibrating the measurement; reference planes refer to the point along the waveguide to which calibrations have been performed. Everything before the reference plane is then considered to have an impedance of 50 Ω (Figure 13). The mathematical representation of the entire measurement in T-matrix form has three T-matrix components: two error boxes (A and B, representing de-embedded measurements) and the T-matrix of the DUT line segment.

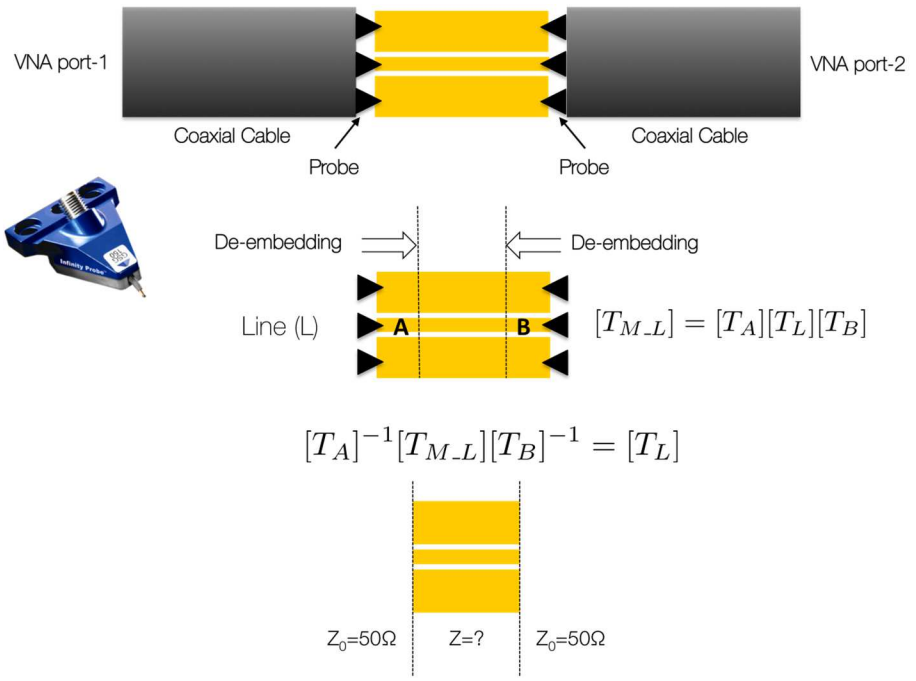

Figure 13. 2-port measurement.

After de-embedding the DUT measurement such that each end of the de-embedded measurement terminates in the characteristic impedance (Z_0, here 50 Ω), we are left with the T-matrix cascade described in Figure 12. The de-embedded DUT T-matrix now consists of an ideal line T_L, with two impedance transforms on either side. We can construct this T-matrix from the impedance and propagation constant for the DUT (Figure 12).

2.4.2 The ExtractRLCG Algorithm

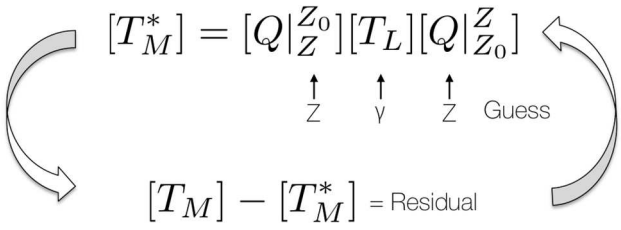

Figure 14. Diagram of ExtractRLCG algorithm.

Our group has developed *ExtractRLCG*, an algorithm that determines RLCG for a de-embedded line by the least-squares-optimization method [14]. ExtractRLCG is related to the trace-method algorithm [13]. This algorithm extracts RLCG values (rendering Z and γ) for the DUT section based on de-embedded S-parameter measurements of the DUT (Figure 14). With an initial guess of RLCG, the algorithm uses the residuals between an ideal constructed DUT and the de-embedded measurement to determine how much to change RLCG in each iteration. This process repeats until it settles on a minimum residual, rendering Z and γ values that match the de-embedded S-parameters.

However, there are some drawbacks to this method. The algorithm may find a local minimum that satisfies the solution. A good initial estimate for RLCG reduces the likelihood of this; if we already know one or more parameters of RLCG, we can hold them fixed, constraining the problem.

Liu et al. has found that the smallest uncertainties for ExtractRLCG occur at low frequencies [14]. ExtractRLCG becomes less accurate at frequencies above 5 GHz, where probe placement errors become problematic for de-embedding line measurements. In our work, we found the optimal range for ExtractRLCG to be between $5x10^5$ Hz and $5x10^9$ Hz. We can also construct a closed-form solution for the line, in which S-parameters are converted to an ABCD matrix [13]. The frequency range between ~20 GHz and ~100 GHz seem to be an optimal range for both the closed-form and trace methods. Below ~10 GHz, these methods result in a very high degree of error; here, ExtractRLCG is far superior [13].

2.4.3 TRL and multi-line TRL Calibration

Many calibration methods and protocols exist, each with advantages and disadvantages. Here, we discuss the thru-reflect-line (TRL), and multi-line TRL methods [63], which yield γ for the DUT section. The basic TRL calibration requires a *through* (T), a *reflect* (R), and a *line* (L) (see DeGroot et al. for an in-depth explanation)[64]. The *through* and *line* are both simple CPW lines; the *reflect* standard defines the

ends of the A and B error boxes for the calibration (Figure 15). The line is simply a longer through, containing both A and B error boxes, as well as line T_L. The idealized line T_L can be represented using the propagation constant alone (Figure 15). The TRL algorithm finds the eigenvalues for the propagation constant for T_L, which satisfies all measurements of through, line, and reflect.

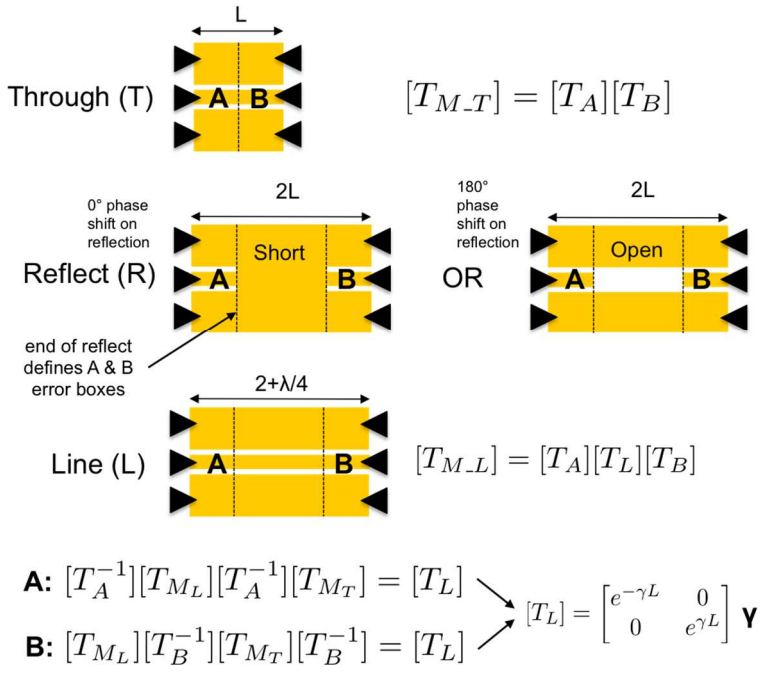

Figure 15. Description of the TRL calibration.

The TRL algorithm gives A and B error boxes and γ for the DUT segment, but not the impedance (Z) of the section. This means that the A and B error boxes in the case of TRL include inside them the impedance transformers discussed earlier. Some reference impedance, with a known value, needs to be measured to extract the impedance of the line. One method is the series resistor calibration discussed in the following section (Section 2.4.4).

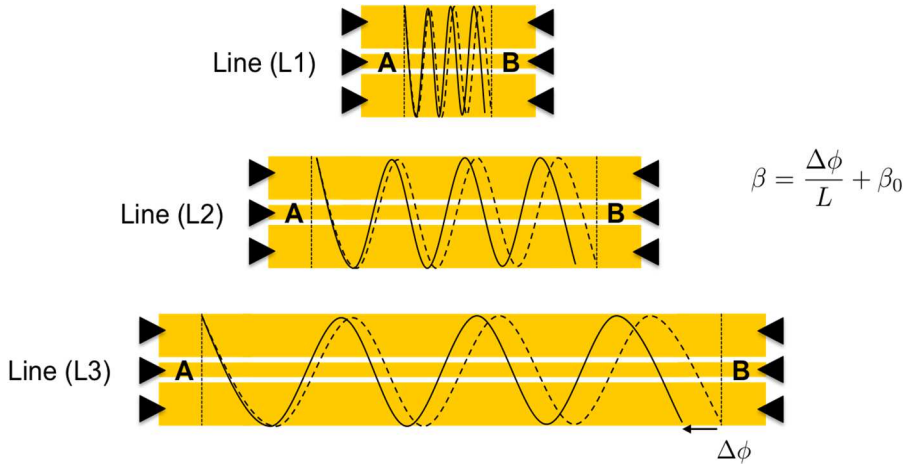

Figure 16. Explanation of how multiple lines help give more phase information to the TRL calibration.

Multi-line TRL calibration (MTRL) is a refinement on the TRL calibration. MTRL uses multiple line standards of varying length to accommodate a wider range of frequencies and reduce overall error. At low frequencies, wavelengths are longer, creating less change in phase across a given length of line, reducing the accuracy of the resultant γ estimate. At high frequencies, too much phase change occurs, making its magnitude difficult to determine. Using multiple lines allows the calibration to operate over a larger frequency range. Not all line length combinations are equal; some combinations of line lengths produce better calibration accuracy than other for the frequencies sampled. Selecting the best set of line lengths requires an in-depth procedure of line length optimization [65].

2.4.4 Series Resistor Calibration

The series resistor calibration uses a known impedance reference to estimate the characteristic impedance of the CPW [66]. The calibration uses three separate calibration structures (or standards): a series resistor (Rs), a through line (L1), and a series capacitor (Cs). The Rs standard is simply the L1 standard with a thin-film resistor in the middle. The Cs standard has the same geometry as the Rs standard, but with no resistor in the middle. The resistor pad in the Rs standard consists of a 10x10 µm area of PdAu material (micrograph of Rs in Figure 18), with a thickness of ~10.5 nm to give the resistor a total DC

resistance of ~50 Ω. Due to the short length of the resistor, its series inductance is negligible; its total impedance is a combination of its measured DC resistance (R_{DC} = Rs – L1) and the capacitance measured by the series capacitor (Cs). The impedance mismatch between the CPW and the resistor section causes reflections. By knowing the impedance of the resistor section, measuring the resulting scattering parameters of the device, and knowing the propagation constant of the CPW lines on either side, we can determine the impedance of the CPW line (Figure 17).

$$R_{DC} = R_{Rs} - R_{L1}$$

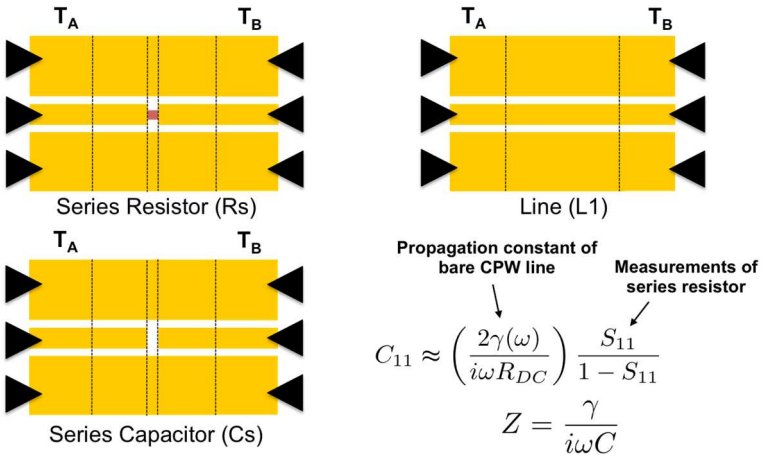

Figure 17. Series resistor calibration.

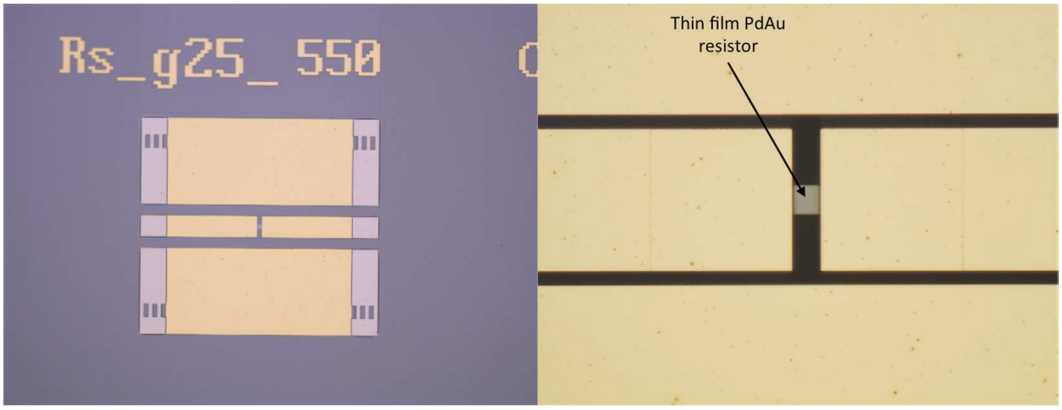

Figure 18. Microscope image of microfabricated series resistor standard (Rs).

3 Device Design and Calibration Method

This chapter will familiarize the reader with the layout, design, and fabrication of the devices used in this work. We will also cover the specifics of calibration used in conjunction with the devices, as the choice of calibration strategy dictates device design. The devices presented in this dissertation extend from a steady iteration in design sophistication within the Booth research group's goals of better electrical measurements of fluid properties using the on-chip calibration method [11,12]. Although a number of different devices have been created over the course of this research, this section focuses on the devices and calibration protocol used in my work on electrical double layer effects in fluids [15].

Although described in full in the following sections, we want to briefly introduce our devices. The devices consist of four primary layers: The fused-silica (quartz) substrate, the conductor layer on which CPWs are patterned, an SU-8 layer, and a PDMS layer. Our devices have two layers of microfluidic channels; the bottom channels are formed in SU-8, and the upper channels are formed in PDMS (Figure 19). Fluid is injected through holes punched in the tops of the PDMS layer, flowing first through the upper PDMS channels over the ground planes, then into the lower SU-8 channels and finally back out again through the PDMS channels (Figure 19B). Measurements are only sensitive to fluids within the SU-8 channels. Using two layers of channels creates well-defined regions over the CPW lines. From a microwave calibration perspective, this design creates three CPW sections (Figure 19E). Sections with distinct EM properties facilitate de-embedding (Section 2.4.1), part of our hybrid calibration strategy (Section 3.3). The remainder of this chapter will explore the considerations and challenges that informed the present device design.

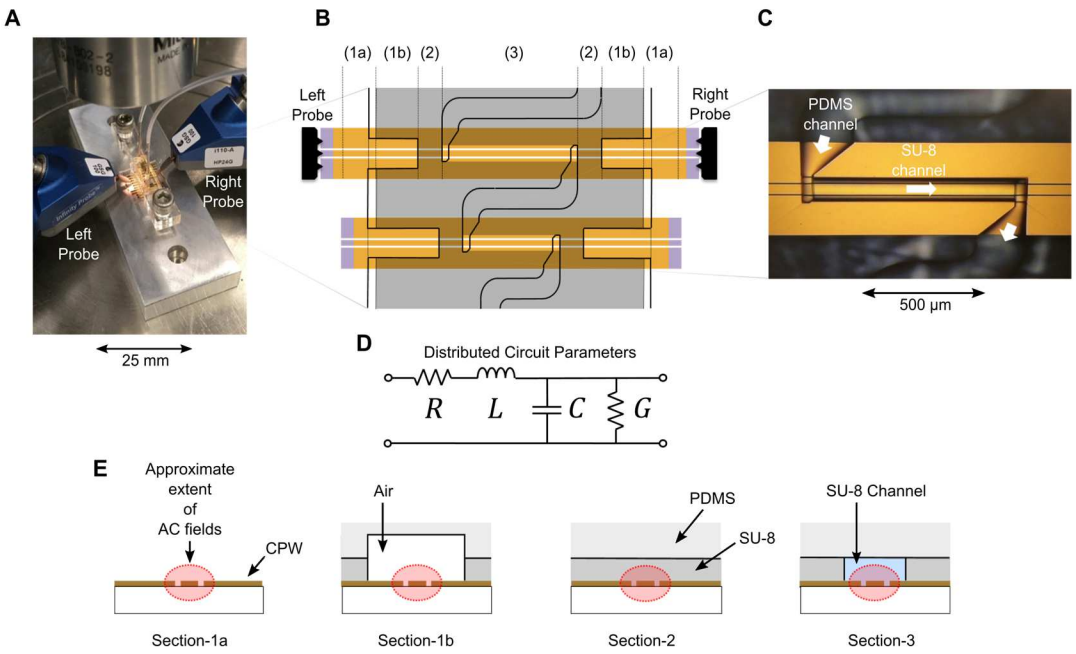

Figure 19. Device design and measurement setup. (A) Image of devices during measurement; left and right probes are shown. (B) Top-view diagram of device design; numbers relate to calibration sections. (C) Microscope image of microfluidic channels with arrows indicating direction of fluid flow. (D) Circuit model describing electrical behavior of the CPW. The distributed circuit parameters R, L, C, G are frequency dependent per unit length quantities, which are different for each calibration section. (E) Cross-section diagrams for each calibration section.

3.1 Device Development

The first microfluidic microwave devices created by the Booth research group consisted of CPW structures microfabricated on quartz or fused silica, similar to the devices discussed in this section. Using on-chip microwave calibrations, these devices were capable of measuring the permittivity of fluids up to 40 GHz [67,68]. A similar device concept was separately employed by Grenier et al. and Ocket et al. [9,69]. Refinements to calibration and design have since pushed the upper frequency limit to 110 GHz [15].

PDMS is the industry standard polymer for creating microfluidic devices. PDMS-based microfluidic devices are fabricated by soft lithography [70], which involves creating rigid positive models over which a liquid polymer, such as PDMS, can be poured and then cured. After curing, the PDMS is

solid, yet still flexible. It is removed from the mold and place on a smooth surface, such as a glass slide, which forms the base of the channel.

Preventing leaks is a major challenge in microfluidics. PDMS is widely used to create microfluidic devices because its physical properties allow it to hold the shape of the channel, while remaining flexible enough to act as a natural gasket, forming a seal. Both pressure and chemical bonding [71,72] can be used to hold the seal. It is also easy to punch holes out of PDMS to insert capillary tubing as inlets and outlets. PDMS is transparent to visible light, which is important for viewing liquids in the channels. Although traditional PDMS-based devices are robust, we have found a number of drawbacks to the direct application of PDMS channels over CPW waveguides and other microelectronic devices.

The first devices created by the Booth group aligned PDMS channels with the underlying CPW structures by hand. Manual alignment is difficult, and some amount of misalignment is inevitable. Most of our calibrations rely on precise knowledge of device geometry; a slight misalignment can lead to poor calibrations. PDMS, although deformable, cannot completely conform to the topography of our CPW structures (~500 nm CPW height); Small gaps in the contact of the PDMS to the underlying structures can result in leaks. These leaks drastically limit the maximum pressure that can be applied and the maximum flow rate, negatively affecting the devices' lifespan and commercial viability. Other issues with PDMS include deformation under fluid pressure, gas permeability, and incompatibility with a number of solvents [73].

I refer to one device-specific issue as the crossover problem: for a single layer of continuous microfluidic channel, the channel must cross over the CPW ground planes. Asymmetric crossover can be avoided by making the channels wider than the full CPW, causing the interface to appear symmetric to

microwaves traveling along the CPW. This can result in channel widths that exceed 200 μm; these large channel widths result in dead volumes, and can prevent laminar flow.

SU-8 is a photo-definable epoxy-based polymer, prevalent in clean-room applications. We have found that SU-8 solves many of the problems presented by PDMS. SU-8 is often used to create support structures larger than those created with standard deposition methods. Processing of SU-8 involves spin-coating the un-crosslinked version of the polymer onto a wafer, exposing the polymer to ultraviolet (UV) light with standard photo-lithography tools, heating to initiate crosslinking, and removing the un-crosslinked polymer with a solvent. This leaves a rigid SU-8 structure on the wafer that can be made to be anywhere from 2 μm to 200 μm thick. The final structure is optically clear and chemically inert to a wide array of acids and bases, as well as with both polar and non-polar solvents [73,74]. Most importantly, crosslinked SU-8 conforms to any underlying structures. SU-8 can be used to form the walls of microfluidic channels. It then needs to be capped in some way to complete the channel. Our present devices cap SU-8 channels with PDMS. The top surface of the SU-8 is left flat after patterning; this makes it easy to form a seal with the bottom surface of PDMS. Conformance of the SU-8 layer to underlying structures ensures that there is no space for leaks to occur. I have devoted substantial attention to perfecting SU-8 fabrication procedures. These procedures and their development are detailed in Appendix-A.

3.2 Device Fabrication Process

This section gives an over-view of the fabrication process we used to construct microfluidic-microwave devices. The processes described herein distill years of process development. Devices are constructed in layers. With the exception of the substrate, each layer was produced through lithography. The layers, discussed in detail below, are as follows: Layer 0 is the substrate (in this case quartz), Layer 1 defines the alignment marks and contact pads, Layer 2 consists of thin-film resistors, Layer 3 is the

primary conductor layer, Layer 4 is the SU-8 microfluidic channel layer, and Layer 5 is the PDMS microfluidic channel layer.

3.2.1 Layer 0: Substrate

The on-chip calibration protocol that will be discussed in section 3.3 requires multiple CPW structures. We co-fabricated both CPW structures with microfluidic channels and all additional calibration structures on the same 500 μm thick 7.62 cm diameter fused silica (quartz) wafer. Co-fabrication minimizes variability in material properties and dimensions among CPW structures. We chose fused silica for its low electrical conductivity and isotropic permittivity. Previous devices used high-resistive (>18 kOhm) silicon substrates.

3.2.2 Layer 1: Alignment Marks and Contact Pads

Electron beam evaporation is used to deposit Ti (5 nm) \ Pd (200 nm), patterned using a standard SPR-660 photoresist. This layer forms alignment markers while also reinforcing the contact pads. Photolithography was performed using an ASML 550/100D wafer stepper, capable of sub-micron resolution and alignment. The stepper alignment marks use a diffraction pattern to align the wafer to the mask. Two alignment markers are patterned on either side of the wafer. This material is also patterned under the contact pads on each CPW device. Palladium, a hard conducting metal, acts as a pad reinforcement to increase device lifetime under repeated probing.

3.2.3 Layer 2: Thin-film Resistors

Thin-film resistors are used in the series resistor calibration. The alloy PdAu was used as the resistor material due to its resistance to corrosion and its low resistivity dependence on temperature [75]. Multiple four-point probe measurements of the PdAu sheet resistance were performed to determine optimal thickness. We wanted a resistor with a total resistance of ~50 Ω for microwave calibration. We

consistently achieve a resistance value of 50 ± 10 Ω, corresponding to a thickness of ~10.5 nm. To increase adhesion to the substrate, we first deposited 1.6 nm of Ti. This thickness was chosen to minimize the Ti layer's electrical effect on the total resistor. Below a thickness of ~2 nm, the Ti film becomes discontinuous [76], greatly increasing its resistance. Resistors were patterned using a standard SPR-660 photoresist liftoff. Resistors were designed to be 10x10 μm in size, with large contact areas on either side. The contact areas lie under the center-conductors for electrical contact, but do not add to the resistance.

3.2.4 Layer 3: Conductor Layer

Conducting metal layers for CPW structures were made of Ti (5nm) \ Au (500nm). Gold is used for its low electrical resistivity and resistance to corrosion. A thicker metal layer means lower resistance and lower losses in the CPW. However, metal thickness on the order of the gap width (W_{gap}) will result in non-standard field distribution. For the 5 μm gaps used in these devices, we found an optimal metal thickness was around 500 nm. For the series resistor, conductive metal was patterned over the resistor contact pads. A lift-off-resist (LOR) process was used to pattern and lift-off the thick layer of metal (LOR-5a, MicroChem).

3.2.5 Layer 4: SU-8 Layer

The SU-8 process we now use is optimized to maximize adhesion and minimize stress. In our recipe, SU-8 3000 series is spun on the wafer. Immediately after spinning, the wafer is soft-baked at 85 °C for 10 minutes and ramped down to room temperature. SU-8 is exposed with the stepper (i-line source 365 nm) with 200 mJ/cm^2. It is then baked at 55 °C for 1 hour after exposure [77]. Un-exposed SU-8 is removed with SU-8 developer (a solvent). We use a spin-on method to apply the SU-8 developer; continuously applying the developer until all un-crosslinked SU-8 is removed. This step is followed by 1 minute of immersion in Isopropanol. For lower exposure doses, it is important to follow up with a hard-bake to ameliorate *crazing* on the surface. Crazing is the formation of a network of shallow cracks on the

surfaces of the polymer as it crosslinks; it also can be seen to occur in ceramic glazes. During the post-exposure bake, the wafer is raised slowly to a temperature of 150 °C for 5 minutes, then cooled slowly to room temperature. After the SU-8 process, the wafer is cut into individual 12x12 mm die. Appendix-A contains further detail about our SU-8 process.

3.2.6 Layer 5: PDMS

We also use SU-8 as a positive mold to form the PDMS channels. Positive SU-8 molds of the channels are patterned on a separate silicon wafer. The SU-8 thickness is ~50 μm. PDMS is poured slowly over the mold, with surface tension at the wafer edges preventing the PDMS from spilling over. The wafer is baked at 60°C for 24 hours. The solidified PDMS is then pulled from the mold. The PDMS is cut along die sections into ~1x0.5 cm blocks using a razor blade. Holes are punched in the PDMS to allow for stainless steel capillary tubes to be placed snugly into the holes; these become fluid inlets and outlets. The PDMS blocks are placed by hand onto individual device die under a microscope.

3.3 Hybrid Calibration Protocol

This section covers the specifics of the hybrid calibration protocol used in conjunction with our devices. Device design (i.e. the lithographic pattern for each layer) was primarily dictated by our choice of calibration strategy. We have utilized a calibration that combines MTRL, series resistor calibration, de-embedding and distributed circuit parameter fitting (Sections 2.4.1 and 2.4.2.) This MTRL approach splits the calibration into two chips, the *dcal* and *test* chips. In general, the MTRL calibration is used for higher frequencies (>1 GHz) and the de-embedding method for lower frequencies (< 1 GHz). Chapter 6 contains experimental validation for the calibration strategy outlined in this section.

3.3.1 MTRL and Series-resistor for Bare CPW

The calibration was divided into two steps, sometimes referred to as a two-tier calibration. The first-tier calibration involves measuring seven different bare CPW lengths (0.420, 1.000, 1.735, 3.135, 4.595, 7.615, and 9.970 mm), a series resistor, a series capacitor, and a short-circuit reflect (Figure 20). The series resistor and series capacitor calibration structures used in our devices are identical to those described in previous work by Orloff et al. [78], explained previously in section 2.4.4.

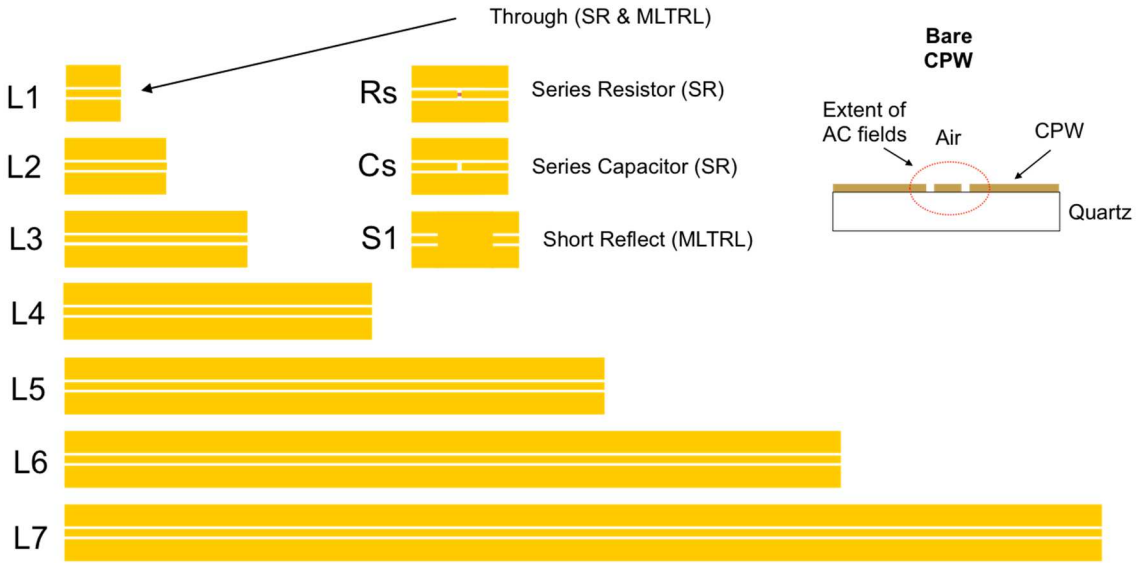

Figure 20. Bare CPW calibration structures used in MTRL and the series resistor calibrations.

We first performed a MTRL calibration [79] using measurements from devices L1 through L7 and the S1 reflect (Figure 20). MTRL calibration on the bare CPW structures yields the propagation constant for the bare CPW lines (γ_0), in addition to their error boxes (T_A and T_B in Figure 22). We additionally perform series-resistor calibration using measurements of L1, Rs, and Cs, yielding an estimate of capacitance per unit length (PUL) of the bare CPW section (C_0); this estimation assumes negligible conductance ($G_0 = 0$). For a quartz substrate and bare CPW capacitance (C_0) is assumed to be constant with frequency. Having γ_0 and C_0, we can construct the Z and γ for the bare CPW lines on quartz, which now give us the resistance (R_0) and inductance (L_0) for a discrete segment of bare CPW line.

3.3.2 MTRL Calibration at Higher Frequencies

In the second-tier calibration we begin to measure the microfluidic channels directly. Here we again use the MTRL algorithm (Figure 21), this time on the microfluidic channels. In this case, we have only four lines, each with different lengths of microfluidic channels, as well as a reflect with channels (0.5, 0.85, 1.55, and 3.314 mm long). Using these lines and reflect we perform another MTRL calibration, which gives the propagation constant for the channel (γ_{tot}). In this step, we also measure two lengths of SU-8-covered CPW line (Figure 21), which will be used in de-embedding.

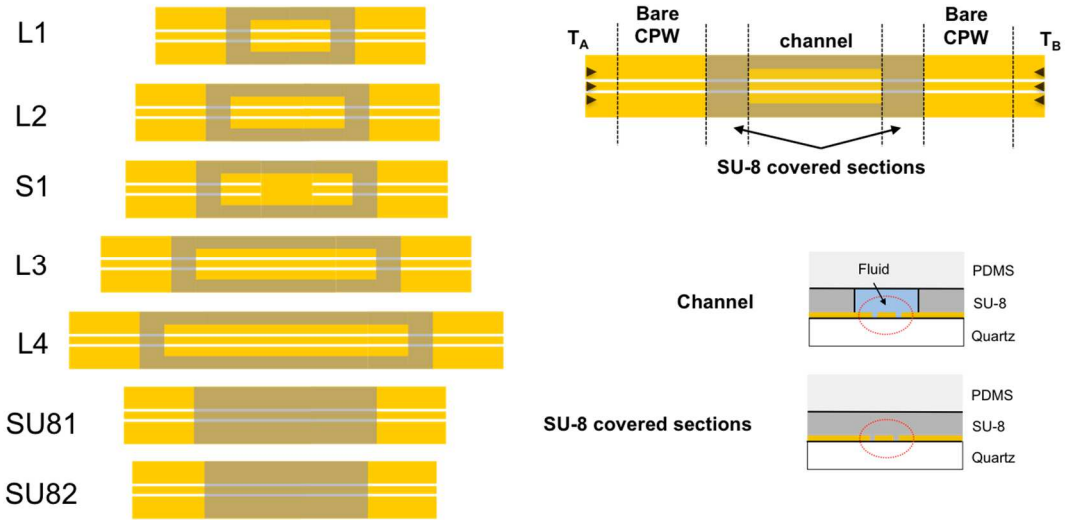

Figure 21. Test calibration.

To get all four distributed circuit parameters for the fluid channel (R_{tot}, L_{tot}, C_{tot}, G_{tot}), we need to know the impedance of the channel (Z_{tot}). We can calculate Z_{tot} if we know R_{tot} and L_{tot}. Here we assume that $R_{tot} = R_0$ and that $L_{tot} = L_0$, which is true for non-magnetic systems. The propagation constant for the bare CPW lines can be written as: $\gamma_0 = \sqrt{(R_0 + i\omega L_0)(G_0 + i\omega C_0)}$, where ω is the angular frequency and R_0, L_0, G_0, and C_0 are the distributed resistance, inductance, conductance, and capacitance PUL of the bare CPW lines, respectively, as a function of frequency. We can assume that $G_0 = 0$ as quartz has a negligible conductivity. Given a nonmagnetic fluid, $\gamma_{tot} = \sqrt{(R_0 + i\omega L_0)(G_{tot} + i\omega C_{tot})}$, where R_0 and L_0 came from the first-tier calibration of the bare CPW structures on the reference or dcal substrate, and

where G_{tot} and C_{tot} are the capacitance and conductance PUL, respectively, of the microfluidic channels. We computed G_{tot} and C_{tot} using both γ_{tot} and γ_0 [80]:

$$\left(\frac{\gamma_{tot}^2}{\gamma_0^2}\right) \cdot i\omega C_0 = G_{tot} + i\omega C_{tot}.$$

Equation 6. Ratio of propagation constants method, assumes the same R and L between decal and test devices.

3.3.3 De-embedding and ExtractingRLCG for Lower Frequencies

The MTRL calibration enables accurate measurements at microwave and mm-wave frequencies; the upper frequency limit of the measurements in this approach is determined by the appearance of higher-order waveguide modes beyond the quasi-TEM mode, at frequencies >150 GHz, depending on the cross-sectional dimensions of the waveguides. The lower frequency limit is determined by the length of the longest CPW line; however, there are practical limits to the length of CPW structures. Below 5 GHz, instead of using the multiline-TRL approach, we directly extracted the propagation constant of the channels through an alternative calibration procedure of de-embedding and distributed parameter fitting, previously described in Section 2.4.1 and Section 2.4.2 [12,14].

De-embedding involves accounting for the impedance and propagation constant of cables, probes, and each section leading up to the microfluidic channels. Error boxes from the first-tier calibration account for the effects of the cables and probes. The de-embedding procedure starts from these error boxes (T_A and T_B in Figure 22). To make the analysis easier, we first modify the error boxes so that they end at the probe tips (T_{A*} and T_{B*}). To accomplish this, we use Z_0 and γ_0, determined in the first-tier calibration, to remove a length of bare CPW line from each error box, equal to half the length of the through line (1/2 L_T, Step#1 in Figure 22). We then add back a length of bare CPW line (L_1, Figure 22); this length of bare CPW line is the same for all microfluidic devices and for the two lengths of SU-8 section. Next, we determine the properties of the SU-8 covered CPW. The two SU-8 lines in Figure 21 are used to get Z_{SU8} and γ_{SU8}. Having already done the work of de-embedding to the interface of the SU-8

covered section, we use the ExtractRLCG algorithm (Section 2.4.2) holding fixed $R_{SU8} = R_0$ and $L_{SU8} = L_0$ to get C_{SU8} and G_{SU8} (Step#2, Figure 22). We now have the information necessary to de-embed all the way to the channel (Step#3, Figure 22). We now perform the ExtractRLCG algorithm on the de-embedded section of channel, holding fixed $R_{tot} = R_0$ and $L_{tot} = L_0$.

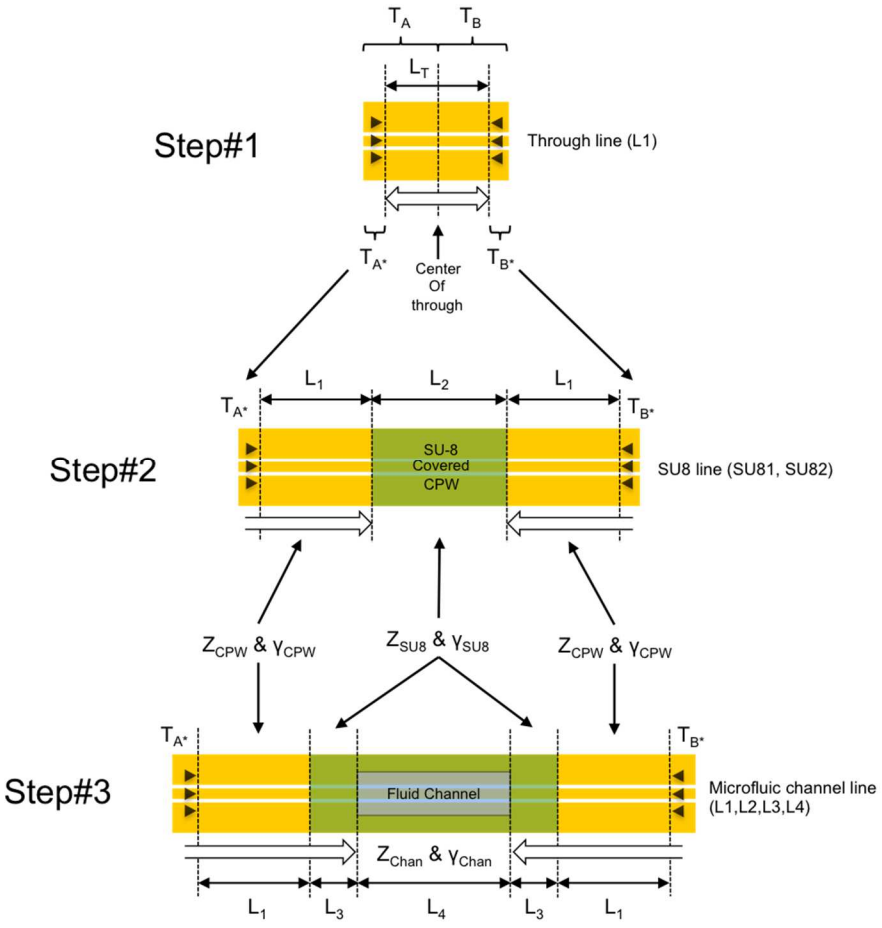

Figure 22. De-embedding procedure. Step#1: preparing error boxes T_{A^*} and T_{B^*} to probe tips. Step#2: De-embedding to SU-8 section on SU-8 line and performing ExtractRLCG algorithm. Step#3: De-embedding to channel section and performing ExtractRLCG algorithm.

3.3.4 Determining Uncertainties in the Hybrid Calibration

Uncertainties in our values for RLCG from the hybrid calibration are determined in two separate ways. For the higher frequency MTRL calibration [13,79], uncertainties for the extracted propagation constants (γ_{tot} and γ_0) are based on various error sources that are propagated through a Monte Carlo

uncertainty analysis as part of the NIST Microwave Uncertainty Framework . In a similar manor, we can get uncertainties from the series resistor calibration [78] for the capacitance PUL for the bare CPW line (C_0). By propagating uncertainties through Equation 6, we can get uncertainties for the conductance and capacitance PUL for the channel sections (G_{tot} and C_{tot}). For lower frequencies, using the de-embedding method, instead of propagating error, we directly calculated the standard error (SE) for G_{tot} and C_{tot}. We calculate the mean as our values for G_{tot} and C_{tot}, as well as the standard deviation (σ) between the four line lengths on the test chip (L1,L2,L3,L4), where $\mathrm{SE} = \sigma/2$.

3.4 Devices and Wafer Layout

The following section discusses the patterning of the device layers. For the most part, each layer design is de-coupled from the fabrication process discussed in Section 3.2; we can consider them separately. With the fabrication process in hand, we can make any pattern we want in each layer.

Our first consideration was choosing dimensions for the CPW structures. First, the CPWs must be compatible with the probes dimensions; we use probes with a 50 μm pitch (distance between the center and ground probes). The CPWs must have a nominal characteristic impedance of ~50 Ω to match the probes, cables, and VNA. Lastly, we want the fields to be primarily contained within the channels. The fields die off from the gap exponentially; from simulations, we have determined that anything 5 times the width of the gap away from the gap has a negligible effect on the measurement. To keep the effect of the PDMS negligible, we fabricated devices with SU-8 channels that were ~50 μm in height/thickness, with 5 μm gaps between the center conductor and ground planes. Analytical approximations indicate that maintaining a characteristic impedance of ~50 Ω, with 5 μm wide gaps on quartz, requires a ~50 μm wide center-conductor. The width of the ground plane has less impact on the impedance of the CPW line, but it should be made wide to limit higher-order modes. We chose to fabricate 200 μm-wide ground planes.

The bottom SU-8 channel and PDMS channels are ~50 μm in height. The SU-8 channels are patterned directly over the CPW structures. We designed the SU-8 microfluidic channels to be ~80 μm wide, and 0.5, 0.85, 1.55, and 3.314 mm long. An acrylic press bar screwed into an aluminum chuck presses the PDMS against the SU-8 and chip, sealing the PDMS block to the chip.

As mentioned at the beginning of this chapter, our microfluidic CPW devices had four physically distinct sections (Figure 19E): a bare CPW section with nothing over the CPW, a bare CPW section with a PDMS roof, a CPW section completely covered with SU-8 and PDMS, and the SU-8 channel section. The first and second sections are electrically equivalent; both can be considered bare CPW sections.

Real estate was a major consideration for our chip designs. The MTRL and series resistor calibrations for the bare-CPW section took up too much space to be placed on the same chip as the microfluidic channels. The inlet and outlet ports also limited the number of lines we could put on a single chip. CPW lines are larger than standard microelectronics, and chips can only be ~12x12 mm in size due to restrictions in the stepper. Ultimately, we decided to split the calibration between two chips: the *decal* chip and the *test* chip (Section 3.4.1 and Section 3.4.2).

The global layout of chips on the wafer is shown in Figure 23. There were 10 decal chips, 8 microfluidic test chips, and 2 SU-8 test chips. The SU-8 chips are based on the same basic design of channel as those with SU-8 channels but with channels filled in with SU-8. This gives us a MTRL measurement of the SU-8 properties. In addition, we added one large square of resistor material (PdAu) on the edge of the wafer to verify each wafer's sheet resistance. There were also two alignment markers for the ASML stepper, positioned to the left and right of the flat edge of the wafer. The following two subsections detail the design of the decal and test chips.

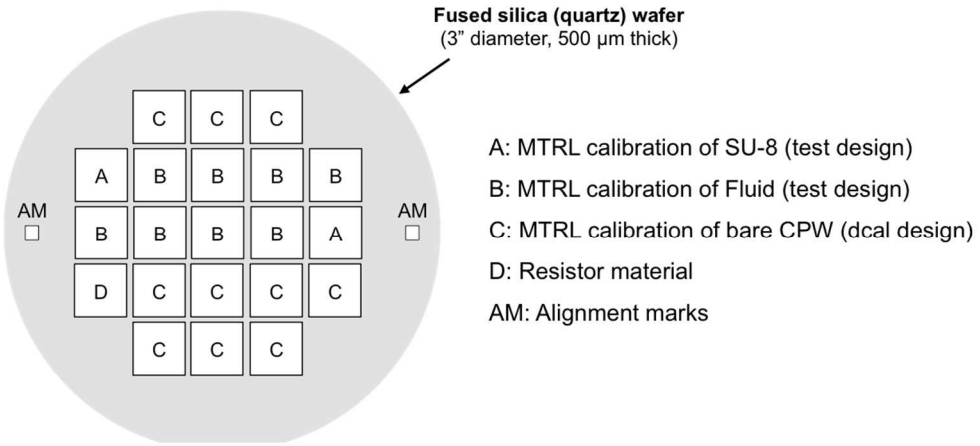

Figure 23. Example layout of devices on wafer for hybrid calibration.

3.4.1 Design of Decal Chips

This section describes the specific design for the decal devices. The MTRL calibration method requires lines of different lengths. The choice of line length affects calibration accuracy. Line lengths for both the MTRL calibration on the decal devices and the test devices were determined through an optimization process [65]. The decal device consists of duplicate calibration structures. The series resistor (Rs), series capacitor (Cs), and the first line length (L1) are used for the series resistor calibration, which determines the capacitance PUL of the bare CPW. The MTRL calibration for the bare CPW, which gives the propagation constant for the bare CPW line, uses all line lengths (L1…L7) and the short reflect (S1).

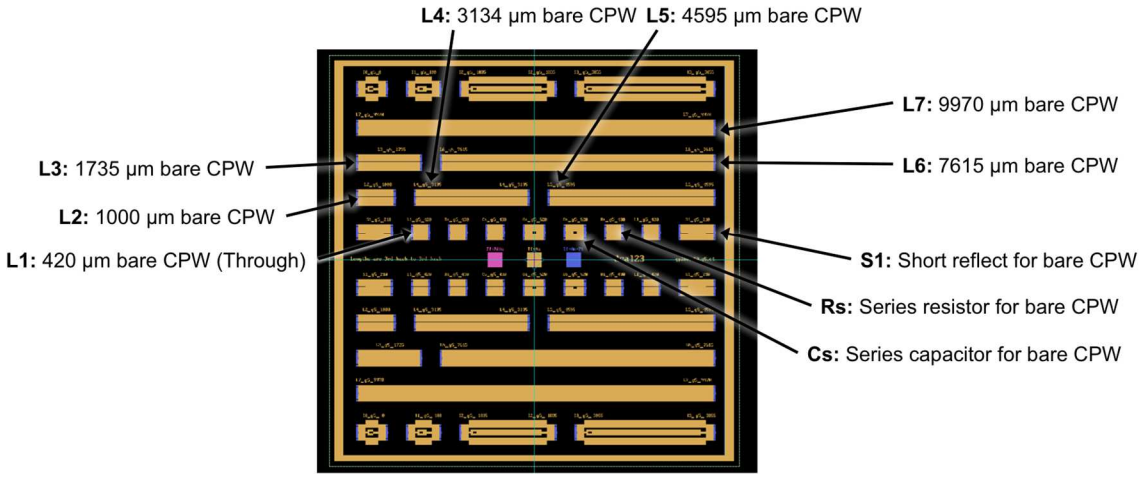

Figure 24. Decal chip layout.

3.4.2 Design of Test Chips

The test devices contain a MTRL calibration for the channels, with the minimum number of calibration structures (L1…L4, and S1), as well as a line for measuring the distributed circuit parameters of a pure SU-8 section. The channel lines on these devices have four distinct sections described already.

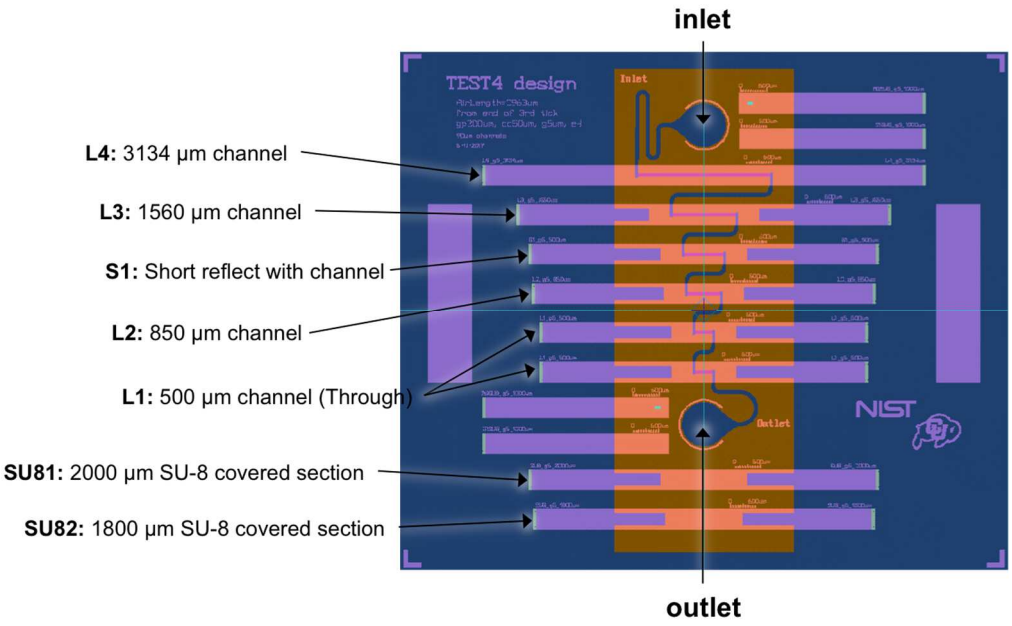

Figure 25. Test chip layout.

One challenge in designing the microfluidic channels was eliminating dead-volume (regions where there is little flow) can result in trapped bubbles or complicate the process of contaminant removal. Dead volumes were particularly problematic in the transitional area between PDMS and SU-8 channels. This transition was narrowed to minimize dead-volumes. COMSOL finite element simulations were used to optimize the transition between PDMS and SU-8 channels (Figure 26).

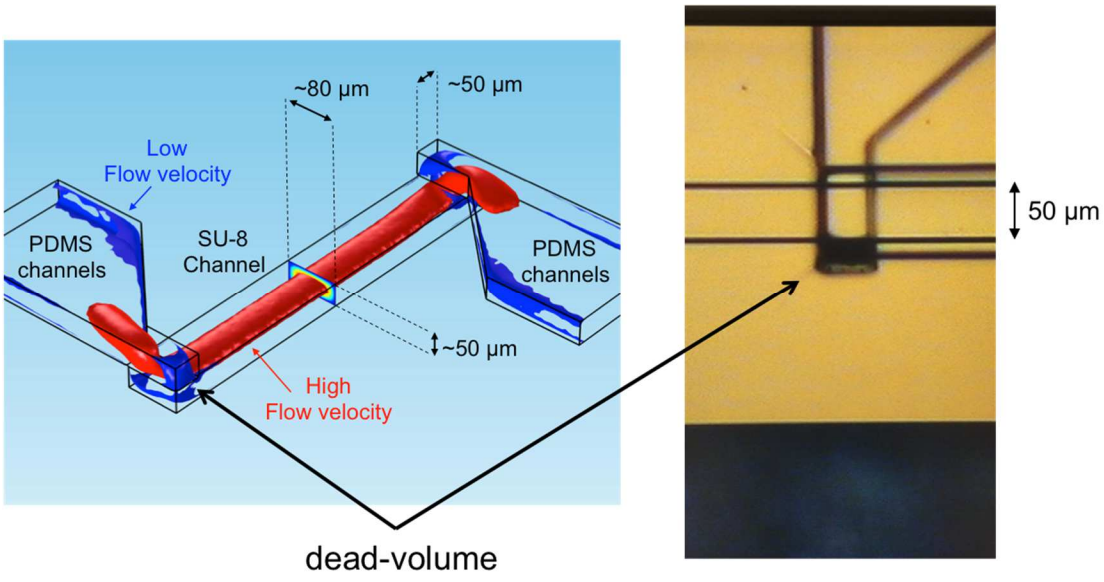

Figure 26. Left) is a COMSOL simulation of flow within our device. In the red areas, flow is high. Outside of the blue surface, flow is low; this is the region where dead-volumes are most likely to occur. Right) is a microscope image of an air bubble trapped in a dead-volume.

3.4.3 PDMS and Device Assembly

This section discusses the design and fabrication of the PDMS layer in conjunction with the assembly of the devices. Measuring materials using the MTRL method requires a staggered pattern of microfluidic channels. The interface between the bare CPW section and the material being measured (DUT) must expand as the DUT becomes longer. In previous devices, PDMS molds were created to define the edges of the PDMS blocks in a staggered pattern. PDMS can tear as it is removed from molds, and its odd shape complicates the alignment. The mold also caused surface tension bowing, which made optical viewing more difficult. The new combined SU-8 and PDMS devices use the SU-8 layer to define the staggered pattern. Even though the fields interact negligibly with the PDMS, we also implemented this staggered pattern in the PDMS layer. In this way, the microwaves do not interact with the SU-8 or PMDS until reaching the SU-8 interface (Figure 27).

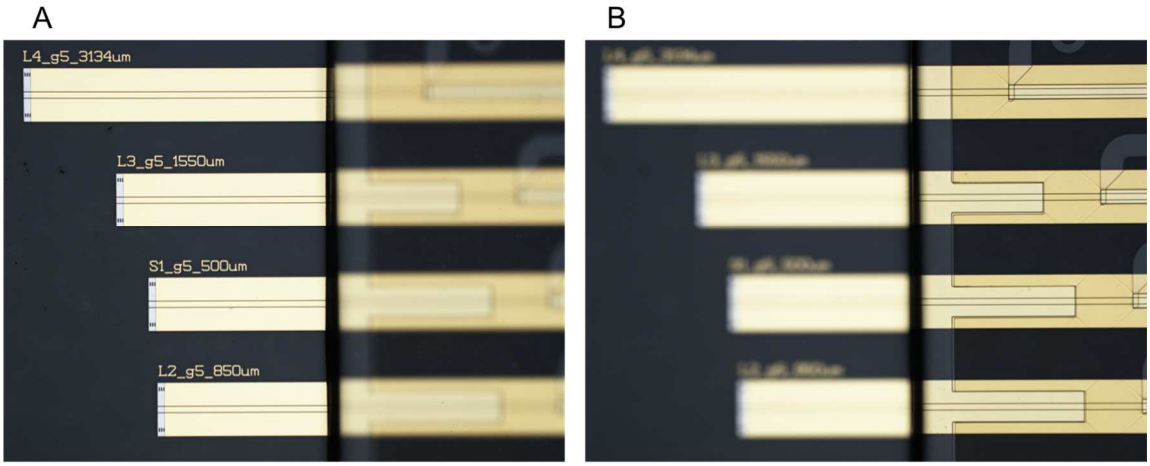

Figure 27. A) Microscope image focused on CPW lines. B) Microscope image focused on SU-8 and PDMS channels. PDMS was hand aligned.

After patterning the underside of the PDMS, we cut blocks of patterned PDMS to place atop our devices (Figure 28). The holes for fluid ports were punched out of the PDMS using a blunt needle, which was sharpened symmetrically on all sides to create a cutting bevel.

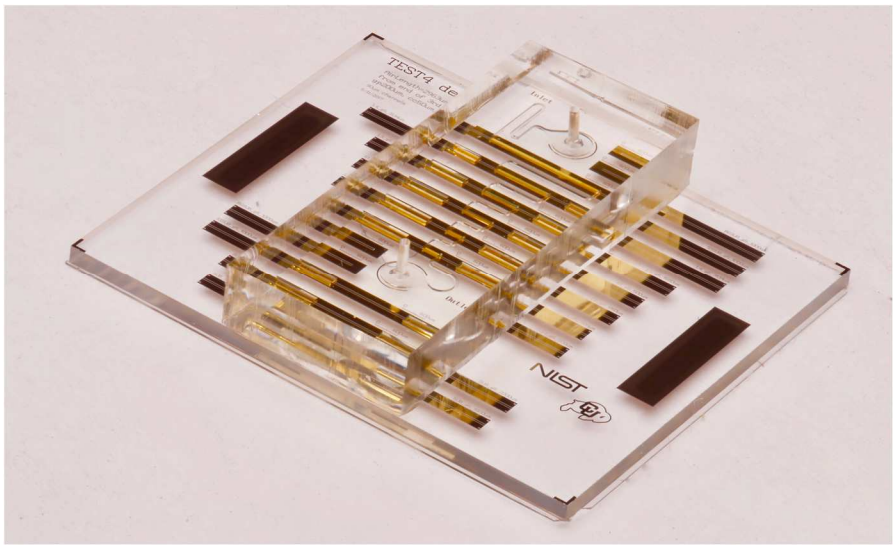

Figure 28. Close-up image of an assembled device.

Although bonding methods exist for PDMS, compression is required to keep the PDMS attached to the substrate at normal microfluidic operating pressures. For these devices, we build a simple compression system consisting of an acrylic press bar on top of the PDMS, which is screwed into an

aluminum plate (Figure 29). The whole device can be placed directly on the probe station. Aluminum, a good thermal conductor, keeps the chip and sample close to the temperature of the probe station.

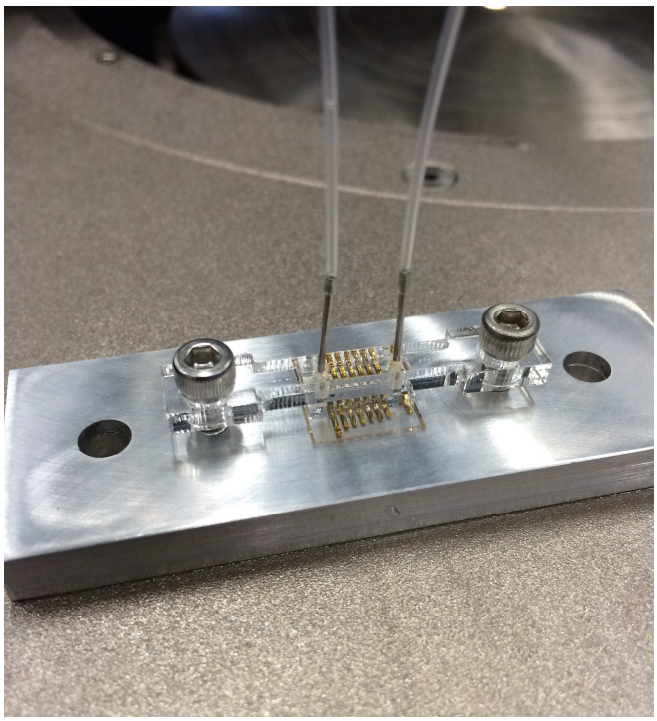

Figure 29. Chip in compression device, with capillary tubing attached.

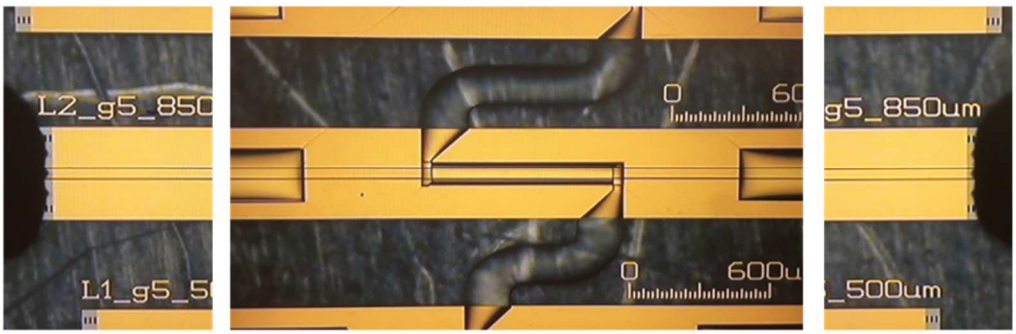

Figure 30. Composite image showing the test device under measurement. Microwave probes are visible on the left and right of the image.

4 Simulations

So far in this dissertation we have described the fabrication of devices and shown how to perform calibrations. Calibrations render the distributed circuit parameters (RLCG) (Section 2.3). We now need to relate RLCG to the permittivity (ϵ) and permeability (μ) of the fluid in the channels. One method for determining ϵ and μ, which we have utilized heavily in the past, is computational simulation. Computational models such as finite element analysis (FEA), the finite difference method (FDM), and method of moment (MoM), simulate the interactions of electromagnetic fields with physical objects and the environment with discrete approximations to Maxwell's equations.

In this chapter, we use computational modeling to build a mapping function between RLCG and ϵ and μ. Because we know the geometry of our devices, we can assign ϵ and μ values to each material in the simulation. We then run the simulation for different values of ϵ and μ (i.e. sweep ϵ and μ) and calculate RLCG from the simulations. This gives us a mapping function that determines ϵ and μ for any measured values of RLCG. [13].

In the following section, we discuss our use of ANSYS Q3D and COMSOL (two FEA electromagnetics software packages) to simulate a 2D section along our waveguides. Q3D and COMSOL can be used to perform both 3-D and 2-D quasi-static electromagnetic field simulations. Q3D is specifically adept at extracting RLCG due to a feature that allows for adaptive meshing based on an optimization of RLCG. The RLCG adaptive meshing capability of Q3D is important for determining accurate values of permittivity. Here we use simulations with the quasi-static approximation. Appendix-D discusses the differences between full-wave simulations and the quasi-static simulations used in the Q3D and COMSOL models.

In Section 4.1, we will go through the process of validating Q3D simulations step-by-step. Q3D has been used extensively by the microwave community, and is considered reliable; COMSOL is less well-validated. For this reason we will use COMSOL simulations more as a qualitative predictor of the electromagnetic field distributions.

4.1 Computationally Determining the Permittivity of Substrate and SU-8

4.1.1 Determining the Resistivity of the Conductor Material

The first step in building our simulation was to determine the resistivity of the conductor material comprising the CPW structure, as this can be measured directly. The conductor is made of Ti (~5 nm) / Au (~500 nm). Because the conductor is primarily composed of gold, its resistivity should be close to the bulk value for gold (~2.2×10^{-8} Ωm at 20 °C [81,82]). We expect, however, that the Ti layer and other micro-scale effects will skew this value, so a direct measurement is necessary. The decal devices have varying lengths of CPW lines, which we can use to determine a resistance PUL (R). For each line, we measured the DC resistance from the center conductor (CC) of port-1 to the CC of port-2. Plotting the DC resistance against length gives us R (Ω/m) of the CC (Figure 31). To determine the resistivity of the conductor material, we need to know the cross-sectional geometry of the CC. Using a calibrated microscope, we measured the width of the CC (49.8 μm); we measured the thickness of the conductor (652.8 nm) via profilometry. The resistivity of the conductor material at 10, 30, and 50 °C for a single batch of devices were measured to be 2.420×10^{-8}, 2.567×10^{-8}, and 2.747×10^{-8} Ωm respectively, slightly higher than bulk gold.

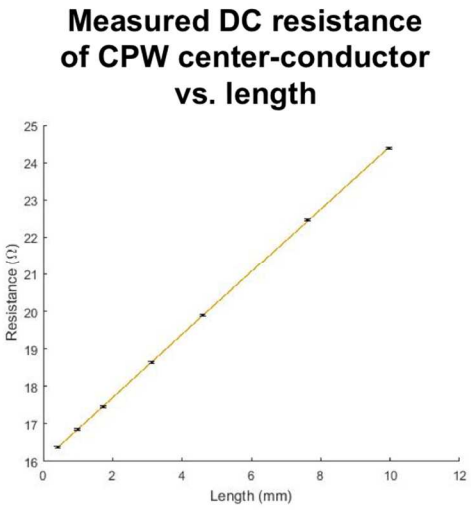

Measured resistivity of conductor material [Ω*m]
2.420×10^{-8} @10 °C
2.567×10^{-8} @30 °C
2.747×10^{-8} @50 °C

Bulk resistivity of gold [Ω*m]
2.44×10^{-8} @10 °C

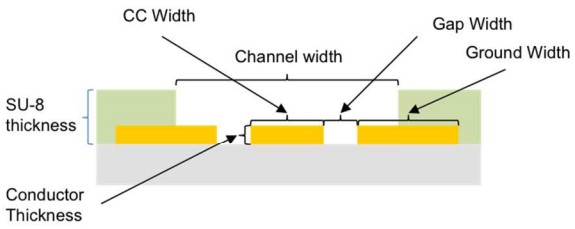

Measured CPW dimensions
- CC width = 49.8 µm (profilometer)
- Gap width = 5.0 µm (microscope)
- Ground width = 200 µm (as defined)
- Conductor thickness = 652.8 nm (profilometer)
- SU-8 thickness = 59.5 µm (profilometer)
- Channel width = 85 µm (microscope)

Figure 31. Conductor resistivity measurements and measured device dimensions

4.1.2 Determining the Permittivity of the Quartz Substrate

The next step is to determine the permittivity of the substrate. We did this by simulating a bare CPW device, with only air ($\varepsilon_r = 1$) above the CPW and substrate below. For the quartz substrate, we know that the conductivity is negligible. In the simulation, we set the loss tangent of the substrate to zero and linearly varied the permittivity of the substrate. From measurements of the decal device and the calibration procedure outlined in 4.2, we can get a measured value for the capacitance PUL (C) for this specific device. Q3D simulations also output an estimate of C, calculated as a function of the substrate permittivity. By matching the C from measurements and the C from the Q3D simulation, we can determine the permittivity of the quartz substrate (Figure 32). The determined relative permittivity of the quartz substrate at 10, 30, and 50 °C was 3.828, 3.829, and 3.830, respectively. This is comparable to known values for the permittivity of fused silica glass (3.81 at 100 MHz at 20 °C [81]).

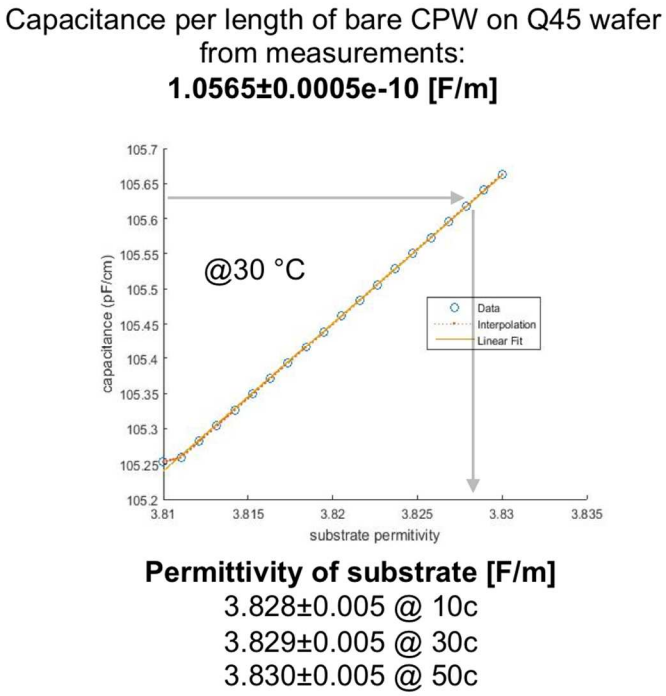

Figure 32. Determination of substrate permittivity.

With conductivity of the conductor and the permittivity of the substrate determined, we now look at the resistance PUL (R) and inductance PUL (L), and compare the simulated values from Q3D to MTRL measurements on the decal device. We also compare with COMSOL. The simulations matched well with measurements (Figure 33). We found that the simulated resistance PUL is extremely sensitive to estimates of the resistivity of the conductor material.

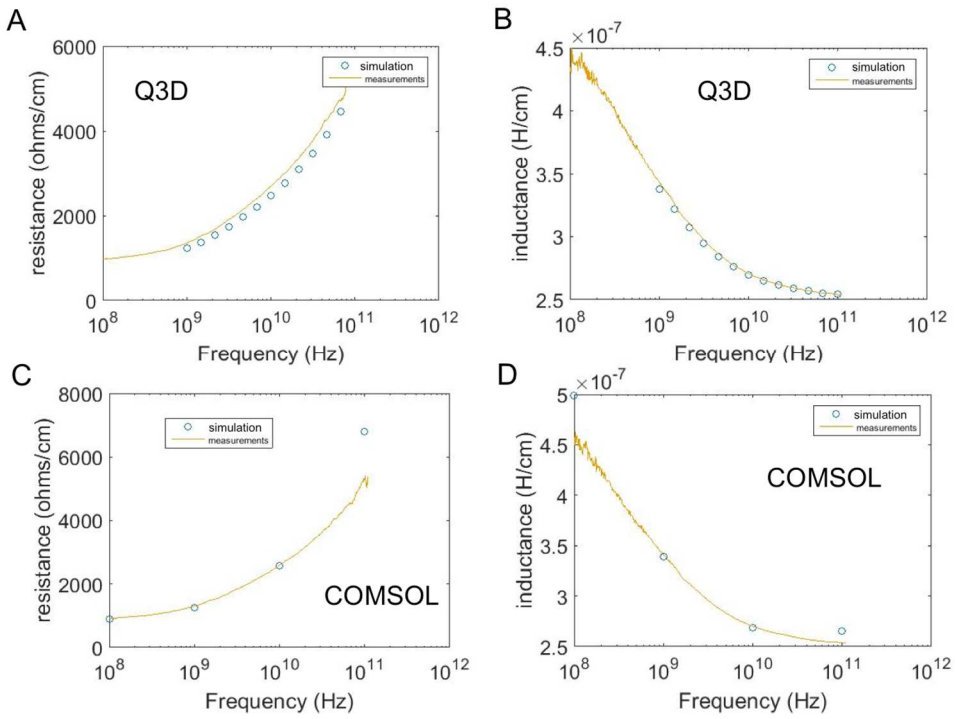

Figure 33. Resistance and inductance per length compared with frequency. A) Resistance of measurements compared with Q3D data. B) Inductance of measurements compared with Q3D data. C) Resistance of measurements compared with COMSOL data. D) Inductance of measurements compared with COMSOL data.

4.1.3 Determining permittivity of SU-8

The de-embedding and ExtractRLCG procedure described in Section 2.4.1 and Section 2.4.2, gave us the capacitance PUL (C) and conductance PUL (G) of the SU-8 covered section. The capacitance and conductance of SU-8 has a slight frequency dependence, which we can reflect in the simulations. This frequency dependence was confirmed by MTRL measurements of covered SU-8 sections, as well as by Liu et al. [13]. Using the previously determined permittivity of the quartz substrate and the same dimensions and resistivity of the conductors, we vary the permittivity above the CPW. In order to estimate the bulk permittivity of SU-8, we matched the C value derived from the simulation to the measured C of the SU-8-covered section. We do this at two frequencies to determine a linear frequency-dependent permittivity of the SU-8. The result is that SU-8 has a relative permittivity of 3.10 between 10 °C and 50 °C at 100 GHz, and 4.62 between 10 °C and 50 °C at 100 kHz (Figure 34).

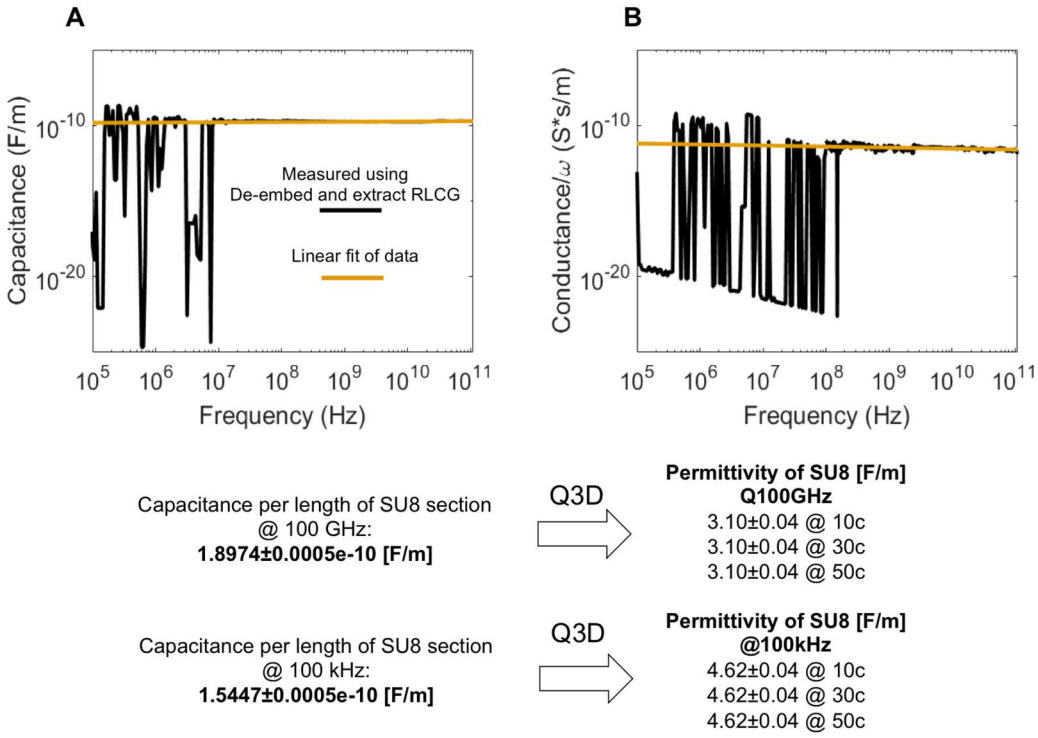

Figure 34. Measurements of the capacitance and conductance of SU-8 covered section.

4.2 Full Computational Simulation of Microfluidic Channels

We now have all the information necessary to build a computational model of the device channels. The simulated SU-8 sections consist of two blocks on either side of the channels. We can re-use the technique of varying permittivity, now within the channel section of the devices. Although the simulations are highly accurate for the bare CPW sections and for the section completely covered by SU-8, we found it difficult to accurately simulate the full channel as the exact cross-sectional geometry of the SU-8 channel proved difficult to determine. The channel cannot be presumed to be perfectly rectangular as photolithography produces non-vertical sidewalls in SU-8. Nor can we accurately measure the width of the channel using profilometry, due to the greater height of the channels; SU-8 is transparent, rendering optical techniques inaccurate. Large uncertainties in our estimates of channel width and geometry lead to a correspondingly large uncertainty in the capacitance of the channel, ultimately compromising the resultant estimate of channel permittivity. Even though the simulations are not accurate enough to extract

permittivity values from the fluids in the channel, they are sufficient in validating measurements. This qualitative use of the simulation will be described in the following sections.

Knowing the electric and magnetic field distribution is important for designing devices and interpreting measurements. As stated previously, we have adopted the design rule that the channel height should be greater than 10 times the gap width (gap width = 5 µm, so channel height = 50 µm) to minimize the interaction of the fields with the PDMS. The fields are predicted to drop off exponentially from the gap, proportional to the width of the gaps. The simulations indicate that this assumption is valid. Separately, we found that when a low-value dielectric material, like air ($\varepsilon_r = 1$), is in the channels, fields are primarily confined to the substrate and channel (Figure 35A). By contrast, in the presence of a high-value dielectric like as water ($\varepsilon_r \approx 80$), fields start to penetrate both the SU-8 sidewalls and the PDMS, contributing to the measured capacitance and conductance.

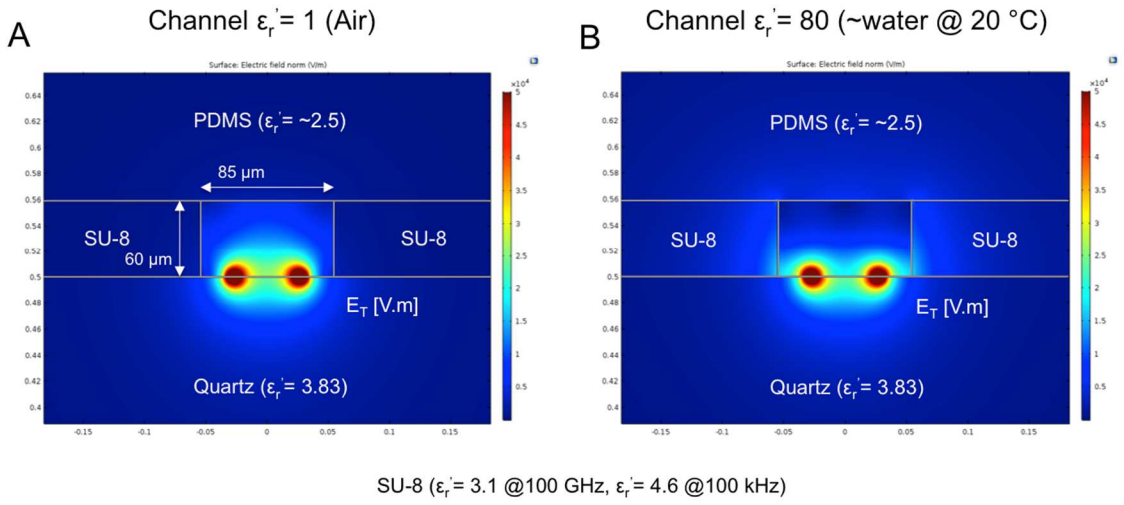

Figure 35. COMSOL contour plots of the magnitude of the electric field (V/m) in the transverse plane. More electric fields penetrate the SU-8 when a higher-value dielectric like water (~80) is present in the channels.

4.3 Mapping Between Distributed Circuit Parameters and Permittivity

The mapping approach described in the previous section requires multiple simulations, one for each permittivity value at each frequency of interest. Interpolation reduces the number of simulations required to extract a complete permittivity and permeability (ϵ and μ) mapping function. We are interested in finding a simpler close-form mapping function or experimental method for mapping from RLCG to ϵ and μ.

From the quasi-static Q3D and COMSOL simulation we found that as we sweep channel permittivity, simulations return a corresponding linear dependence with the capacitance PUL (C) of the channel. We observed the same result when we swept the loss-tangent (imaginary permittivity). This result implies a linear relationship between imaginary permittivity and calculated conductance. The relationship also appeared constant for all frequencies. There was no interdependence between capacitance and conductance when sweeping the real and imaginary permittivity; that is, capacitance is only dependent on the real permittivity while the conductance only on the imaginary permittivity. Finally, we found that the same proportionality constant relates both capacitance to real permittivity and conductance to imaginary permittivity. These findings suggest the following relationships:

$$\epsilon^{'} = (C - C_{Air})k + \epsilon_0,$$

$$\epsilon^{''} = \frac{G - G_{Air}}{\omega}k.$$

$$\mu^{'} = (L - L_{Air})\frac{1}{k} + \mu_0,$$

$$\mu^{''} = \frac{R - R_{Air}}{\omega}\frac{1}{k},$$

Equation 7. TEM approximation leading to a linear relationship between RLCG and permitivity and permeability.

In Equation 7, C_{Air} is the PUL capacitance of an air-filled channel (C_{Air} = 1.08x10^{-10} F/m), ε_0 is the permittivity of free space, and k is a dimensionless geometric conversion factor that is specific to our devices. Instead of using the computational approach mapping RLCG to permittivity and permeability for each value of permittivity at each frequency, we posit a simple analytical relationship. We will employ these linear approximations (Equation 7) in Chapter 5 to convert measurements to permittivity values. Measurements of water will be used to estimate the geometric factor k.

The CPW is described with a dominant quasi-TEM (Transverse Electromagnetic) propagating mode. The relationships in Equation 7 are only valid for the TEM approximation. The general waveguide equations (Equation 8 [83]) gives us the absolute relationship between the distributed circuit parameters (RLCG) and permittivity and permeability (ϵ and μ). Each distributed circuit parameter in Equation 8 is influenced by both the AC fields in the transverse direction (T) and by AC fields in the propagation direction (z). In the TEM approximation, the fields are only in the transverse direction. The equations are complex, requiring integration over a field distribution specific to the waveguide geometry. Because there exist no general analytical solutions for the CPW geometry, we tend to fall back to the linear expression in Equation 7.

$$C = \frac{1}{|V_0|^2}\left[\int \epsilon' |E_T|^2 dS - \int \mu' |H_Z|^2 dS\right]$$
$$G = \frac{\omega}{|V_0|^2}\left[\int \epsilon'' |E_T|^2 dS + \int \mu'' |H_Z|^2 dS\right]$$
$$L = \frac{1}{|i_0|^2}\left[\int \mu' |H_T|^2 dS - \int \epsilon' |E_Z|^2 dS\right]$$
$$R = \frac{\omega}{|i_0|^2}\left[\int \mu'' |H_T|^2 dS + \int \epsilon'' |E_Z|^2 dS\right]$$

Equation 8. General waveguide theory equations [83].

The capacitance and conductance in the waveguide equations (Equation 8) can only be reduced to the linear form (Equation 7) by making some assumptions: By assuming the TEM approximation (i.e. $E_Z = H_Z = 0$), we can remove all transverse (z) components, fully half of the expressions in Equation 8.

Assuming homogenous permittivity values in the two regions above and below the CPW allows the field integral to be split into two parts. If we assume that the permittivities are homogenous in their respective regions, we can consider them constant and remove them from their respective integrals. Under these assumptions, capacitance, for example, reduces to the following:

$$C = \epsilon'_1 \frac{\int |E_T|^2 dS_1}{|V_0|^2} + \epsilon'_2 \frac{\int |E_T|^2 dS_2}{|V_0|^2} = \epsilon'_1 \frac{1}{k_1} + \epsilon'_2 \frac{1}{k_2} ,$$

Equation 9. TEM approximation of the general wavguide equation for capacitance (C) asssuming two regions of homoginous permittivity above and bellow the CPW.

where ϵ'_1 is the permittivity above the waveguide and ϵ'_2 is the permittivity of the substrate below the waveguide. Because capacitance (C) and permittivity have the same units (F/m), we can assume that the geometric constants (k) are unitless. The geometric constant can be interpreted as the ratio of microwave power in each region above or below the waveguide. The geometric constant k, which we extract from simulation and will extract from measurements, is a convolution of the k_1 and k_2, sense the field distribution will change with changing ϵ'_1. However, if we assume that k_1 and k_2 stay relatively constant for changing ϵ'_1, then k_1 and k_2 reduce to the single geometric constants (k) in Equation 7.

For a pure-TEM mode (i.e. an ideal wave propagating in free space) all of the fields are in the transverse direction. However, when a discontinuity is present in the transverse plane, such as when there is a dielectric mismatch between the substrate and space above the CPW, the result is a distortion of the fields centered on the point of discontinuity (Section 6.2.2 and Section 6.2.3). This can lead to fields in the propagation direction, so we expect some non-linearity in the relationship between RLCG and the permittivity of the fluid in the channel. We cannot see these effects in our 2D Q3D and 2D COMSOL simulation because these models assume a uniform field distribution in propagation direction. However, we do see a non-linear relationship in the Full-wave simulations (Full-wave vs. quasi-static simulations described in Appendix-D). Full-wave simulations are computationally intensive, and benchmarking these models is difficult. In addition, the computed non-linearity is small, less than one percent. As such, our

modeling of electrical double layer effects in Chapter 6 will incorporate the TEM-approximation and use the linear equations described above (Equation 7).

5 Modeling Electrical Double Layer Effects

This chapter details work on measuring and modeling of electrical double-layer (EDL) effects. We will explore the use of the microfluidic devices and calibration protocols discussed in Chapter 3 to quantitatively determine the complex electrical impedance of saline-loaded CPW lines between 100 kHz and 110 GHz. Here, we use the high frequency, broadband capabilities of our devices to separate the intrinsic fluid response from electrical double-layer (EDL) effects. A two-component model was developed for electrical double-layer effect comprised of a Debye relaxation and a constant phase element (CPE). We show that the relaxation time associated with this EDL is strictly inversely proportional to the ionic conductivity of the measured solutions. Knowing this information allows us to fit EDL parameters at one concentration and temperature and extrapolate the EDL response to any other combination of concentration and temperature, making it possible to distinguish EDL effects from other low-frequency phenomena. This work was published in 2017 in the journal Lab-on-a-Chip [15] under the title "Modeling Electrical Double-Layer Effects for Microfluidic Impedance Spectroscopy from 100 kHz to 110 GHz."

5.1 Introduction

Many relevant samples for impedance spectroscopy (permittivity measurements <300 MHz), specifically biological samples, have some ionic components. Ionic fluids are a challenge for lower frequency impedance spectroscopy. When electric fields are applied to the fluid as part of the impedance spectroscopy measurement, free ions in solution migrate towards the electrodes. As these ions build up, an EDL layer forms at the surface of the electrodes (Figure 36). The EDL results in a large capacitance between the electrode and fluid, screening electric fields from the bulk of the fluid, thereby reducing

measurement sensitivity to the intrinsic fluid impedance. The ability to distinguish device-specific EDL effects from the intrinsic fluid response is a major challenge for microfluidic impedance spectroscopy, especially at lower frequencies.

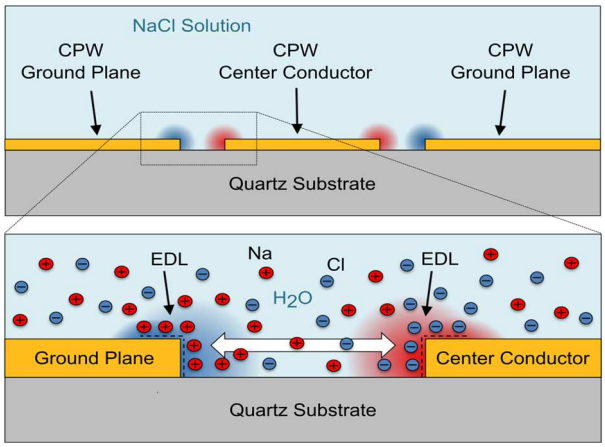

Figure 36. Depiction of the EDL formation. During measurement, ions in the NaCl solution accumulate on the edges of the CPW electrodes.

At sufficiently high frequencies, EDL effects become negligible; higher frequency measurements give information primarily about the dielectric response of the fluids. However, measurements above ~300 MHz require waveguides and microwave calibrations. The 6-decade frequency range provided by our devices and calibration protocol uniquely capture both the low-frequency regime where EDL effects are dominant as well as the high-frequency regime where EDL effects are negligible. Here, we apply our technique to measuring the complex electrical impedance of NaCl solutions (saline) in microfluidic devices over a range of temperatures and concentrations, analyzing the resulting EDL. We can accurately model the intrinsic fluid impedance of saline at high frequencies where EDL effects are negligible, and subsequently extrapolate this fluid response to lower frequencies where EDL effects dominate. In this way, we isolate the EDL contribution to the impedance from the intrinsic fluid impedance for solutions with different ionic conductivities. The frequency dependence of the experimentally-determined EDL impedance can be accurately modelled by a combination of a Cole-Cole response (Section 2.2.4) and a constant phase element (CPE) [84–88]. These models yield a double-layer relaxation time that is inversely

proportional to solution conductivity, with little change in the other fitting parameters with changing solution conductivity. This suggests that device-dependent double-layer effects in microfluidic devices can be quantitatively accounted for based on measurements at a single value of solution conductivity.

5.2 Determining the Linear Mapping Coefficient

In the results section (Section 5.4) we will present calibrated fluid data in terms of C_{tot} and G_{tot}/ω. We have shown in Section 4.3 that these quantities can be approximated as linearly proportional to the real and imaginary parts of the fluid permittivity (ϵ' and ϵ'') respectively. In the following, we used the linear expressions in Equation 7 in conjunction with literature values for the permittivity of de-ionized water [89] (DI water) to compute a value for the geometric constant.

Literature values for the permittivity of DI water came from Fernández et al. [89], whose study aggregated literature values. The permittivity of DI water varies based on temperature; To get specific permittivity values for the temperatures used in this work, we fit the aggregated data from Fernandez et al. at various temperatures to the following polynomial equation:

$$\epsilon_r = a + bT + cT^2$$

Equation 10. Polynomical approximation of the temprature dependence of the static relative permitivity of DI water, where a, b, and c are fitting paramters.

Equation 10 is a polynomial expression similar to that used by Malmberg and Maryott [90], where T is the temperature in Kelvin, and ϵ_r is the relative static permittivity of DI water at zero frequency (DC). The fit resulted in the following values: a = $2.46\text{x}10^{2}$, b = $-7.62\text{x}10^{-1}$ K^{-1}, c = $6.76\text{x}10^{-4}$ K^{-2}. We used Equation 10 to calculate values for ϵ_r. The resulting permittivity values were 84.6, 76.9, and 70.3 at 9.5 °C, 28.6 °C and 47.6 °C, respectively (Table 1), the temperatures used in these experiments. These

permittivity values are consistent with those that result from the equation proposed by Pátek et al. [91], within uncertainties.

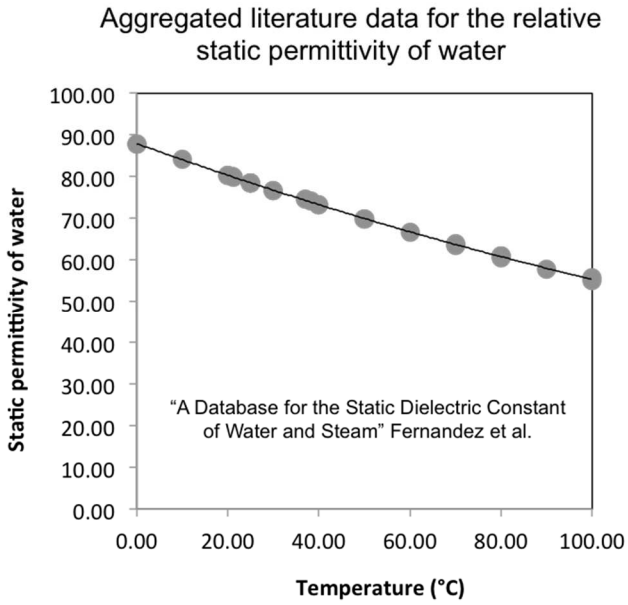

Figure 37. Aggregated data from Fernández et al. [89] for the relative static permittivity of water at various temperatures, fit with Equation 10.

Shown in Table 1 below, we calculate the geometry factor *k* for the three temperatures: 9.5 °C, 28.6 °C and 47.6 °C. We found that *k* has the same value for each temperature ($k = 0.411 \pm 0.005$).

Table 1. Estimation of geometric permittivity conversion factor *k* at different temperatures.

Temp (°C)	9.47	28.53	47.61
Literature value of The relative static permittivity of water	84.25	77.24	70.72
Capacitance per length for water [F/m]	1.90E-09	1.74E-09	1.60E-09
Capacitance per length for air [F/m]	1.12E-10	1.10E-10	1.07E-10
Geometric factor (k)	0.413	0.413	0.413

While Equation 7 allows us to convert measured admittance parameters (C_{tot} and G_{tot}/ω) directly to permittivity values, we only convert to permittivity in situations where we want to describe the intrinsic fluid properties. We do not convert to permittivity for EDL effects, as the EDL is not associated with the intrinsic properties of the fluid. The geometric constant *k* can also be used to determine the ionic conductivity of the measured solutions (σ), as shown in the next section.

5.3 Methods

5.3.1 Measurements

For these measurements, we used the Hybrid Fluid Calibration and Devices described in Chapter 3. We measured each CPW structure using a VNA and movable microwave probes. We acquired 512 frequency points from 100 kHz to 110 GHz on a log frequency scale, at an AC power of -20 dBm (where 0 dBm corresponds to a power of 1 milliwatt), and with an intermediate frequency (IF) bandwidth of 50 Hz. All measurements were performed on a temperature-controlled stage. Care was taken to perform all calibrations and measurements in thermal equilibrium. The chips and aluminum block were kept on the

stage for a minimum of 5 minutes after the stage reached the desired setpoint. After measurements were performed on the decal and air-filled test devices, fluid was injected into the channels and held for at least 1 minute at zero flow rate prior to measuring the fluid. The temperature of the fluid was determined by measuring the temperature at the surface of the aluminum block with a thermocouple at each of the temperature setpoints. The small thermal mass of the chip and fluid sample ensured that the sample was at thermal equilibrium with the aluminum block.

5.3.2 Sample Prep

We used serial dilutions to prepare four concentrations of saline solutions: 30%, 3%, 0.3%, and 0.03% NaCl by weight W_{NaCl}. We prepared the 30% solution by dissolving 428.6 g of NaCl in 1 L of DI water, and then added DI water. For context, normal/physiological saline is 0.9% NaCl [92], typical sea water is ~3.5% NaCl, and the maximum solubility of NaCl in water at 20 °C is 35.9% [93]. Note that our sample fluid with the maximum concentration (W_{NaCl} = 30%) is near the solubility limit.

5.4 Results

The resulting calibrated admittance for air, DI water, and all concentrations of saline, as a function frequency, at temperatures of 9.5 ± 2 °C, 28.6 ± 2 °C, and 47.6 ± 2 °C are shown in Figure 38. We omitted data below a frequency where uncertainties rose above 2% of the measured value. We can qualitatively distinguish EDL effects from the intrinsic fluid admittance in the data as an increase and plateau of capacitance at lower frequencies (seen below ~1 GHz in C_{tot} data for the W_{NaCl} = 30% solution), and as a suppression of conductance, also at lower frequencies (seen below ~10 MHz in G_{tot} data for the W_{NaCl} = 30% solution). We consider increases in G_{tot}/ω from the ionic conductivity of the fluid as part of the intrinsic response of the fluid. As we increased the ionic concentration in the solution, there was a corresponding increase in ionic conductivity as well as a shift in the EDL response to higher

frequencies. The capacitance contribution from the EDL is significant compared to the fluid, up to ~3 orders of magnitude larger than the intrinsic capacitance of water.

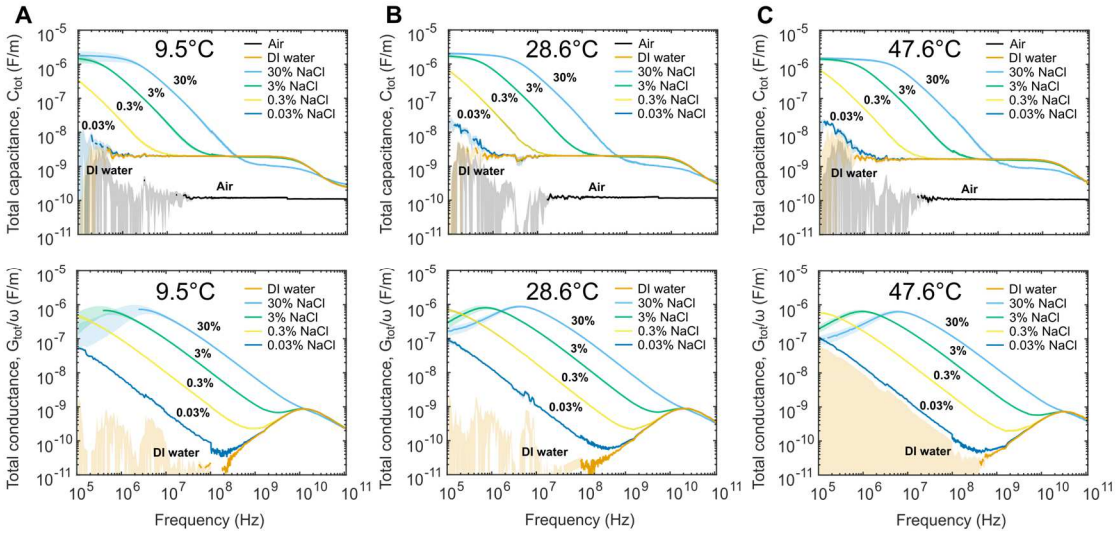

Figure 38. Calibrated admittance per unit length data for all samples. (A) Data at 9.5℃. (B) Data at 28.6℃. (C) Data at 47.6℃.

5.4.1 Modeling the Fluid Admittance

For a given device, the total measured admittance can be written as $Y_{tot} = G_{tot} + i\omega C_{tot}$, (where the total measured impedance is $Z_{tot} = 1/Y_{tot}$). Illustrated in Figure 39A, we assume that the EDL admittance Y_{EDL} acts in series with the fluid admittance Y_f:

$$\frac{1}{Y_{tot}} = \frac{2}{Y_{EDL}} + \frac{1}{Y_f}.$$

Equation 11. Total impedance of measurment (Y_{tot}) can be modeld as the ELD impedance (Y_{EDL}) and the fluid impedance (Y_f) in series.

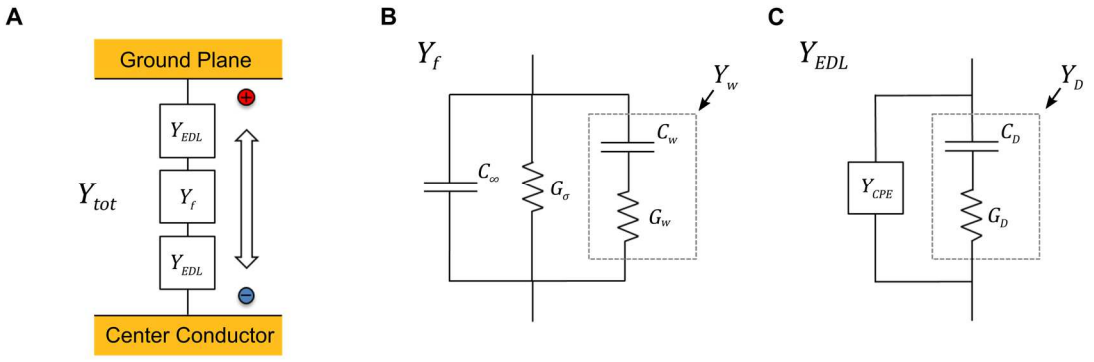

Figure 39. Ionic fluid admittance model. (A) EDL admittance Y_{EDL} and fluid admittance Y_f act in series to form the measured admittance Y_{tot}. (B) Equivalent circuit of Y_f, where C_∞ is the capacitance of the fluid without the dipolar contribution of the water, Y_w is the admittance from the dipolar response of the water, and G_σ is the bulk conductance from the ions. (C) Equivalent circuit of Y_{EDL}, where Y_D is the admittance of the Debye relaxation component of the EDL effect, and Y_{CPE} is the admittance of the constant phase element (CPE).

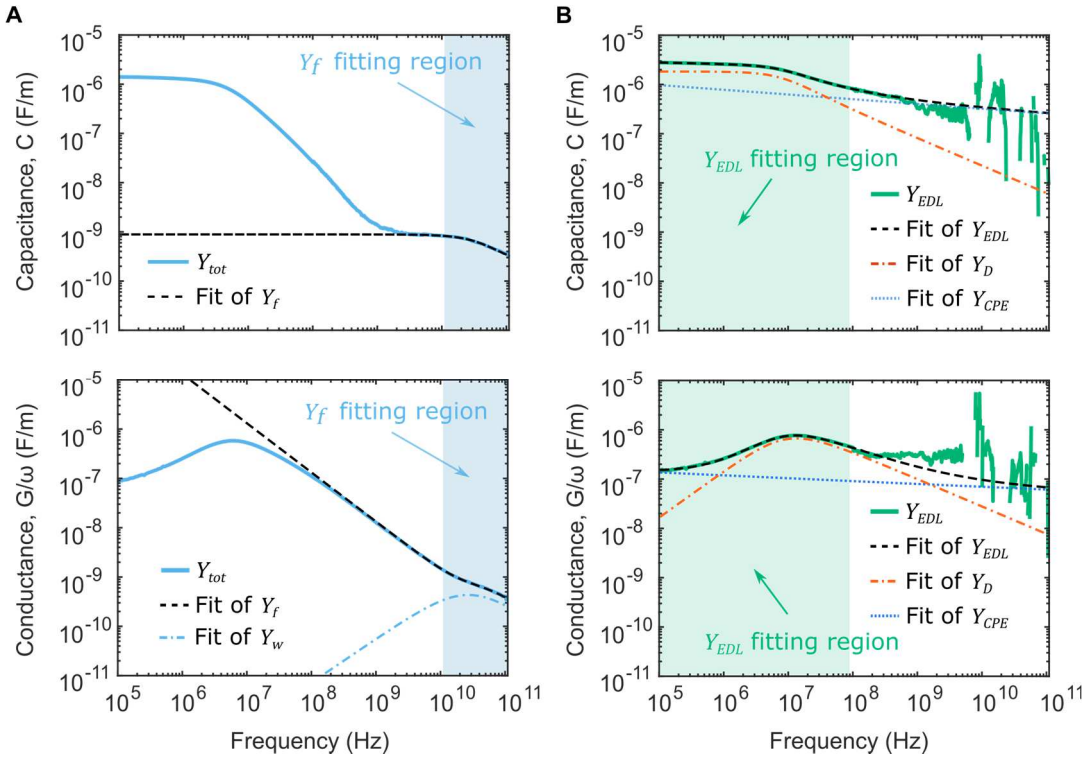

Figure 40. Fitting procedure using W_{NaCl} = 30% data at 47.6 °C. (A) Data, and fit of the fluid admittance (Y_f), with contribution from water admittance (Y_w). (B) Extracted EDL admittance (Y_{EDL}), fit Y_{EDL}, Debye relaxation component of Y_{EDL} (Y_D), and the CPE component of Y_{EDL} (Y_{CPE}).

We initially modeled the admittance of the fluid (Y_f) in the high-frequency regime, above an estimated minimum frequency where EDL effects can be neglected (Figure 40A). We estimated the minimum frequency of this range using an iterative procedure, where we found the lowest frequency that maximized the goodness of fit for a model that included only the fluid response. The fluid admittance of the saline solutions can be represented with the equivalent circuit shown in Figure 39B, with three parallel components: the capacitance of the fluid far above the relaxation frequency of the water C_∞, the dipolar contribution of the water (C_w), and the conductance due to the ions G_σ. When measuring air, $C_\infty = C_{Air}$ and $G_\sigma = C_w = 0$. The relaxation of water (seen at ~20 GHz in our data) is a Debye-type relaxation phenomenon, and is modeled with a Cole-Cole function [58,86–88]. A Cole-Cole description was used to model the water relaxation, instead of a bimodal Debye relaxation (as suggested by Buchner et al.[94]), as the Cole-Cole function produced an acceptable fit with fewer fit parameters for all solutions studied. The total admittance of fluid (Y_f) was therefore:

$$Y_f = i\omega C_\infty + G_\sigma + Y_w = i\omega C_\infty + G_\sigma + i\omega \frac{C_w}{1 + (i\omega\tau_w)^{1-\alpha_w}},$$

Equation 12. The fluid impednace (Y_f), which is a combination of the impedance of the water and the conductivity from the ions (G_σ).

The resulting fit parameters for Y_f, obtained from the high frequency portion of the admittance spectra, for all ionic concentrations and all temperatures can be found in Table 2.

.

Table 2. Fluid admittance per unit length fitting parameters using Equation 16, as well as the intrinsic parameters describing the Cole-Cole fit to the fluid permittivity. The values for the relative permittivity of DI water are from the literature and are marked with an asterisk (*). These values were used to determine the geometric factor *k*.

Temp (℃)	W_{NaCl} (%)	C_w (F/m)	Relative permittivity water (f=0)	C_∞ (F/m)	Relative permittivity water (f=∞)	τ_w (s)	$1-\alpha_w$	G_σ (S/m)
	30	1.07×10^{-9}	45.8	2.09×10^{-10}	5.7	9.41×10^{-12}	0.849	4.15×10^{1}
	3	1.80×10^{-9}	79.6	2.09×10^{-10}	5.7	1.18×10^{-11}	0.980	6.24
9.5	0.3	1.90×10^{-9}	84.3	2.13×10^{-10}	5.9	1.22×10^{-11}	0.992	5.91×10^{-1}
	0.03	1.91×10^{-9}	84.6	2.16×10^{-10}	6.0	1.22×10^{-11}	0.997	4.02×10^{-2}
	DI water	1.91×10^{-9}	84.6*	2.16×10^{-10}	6.0	1.22×10^{-11}	0.998	$<1 \times 10^{-2}$
	30	9.06×10^{-9}	38.0	2.00×10^{-10}	5.3	4.96×10^{-12}	0.896	6.50×10^{1}
	3	1.64×10^{-9}	72.1	1.87×10^{-10}	4.7	6.93×10^{-12}	0.974	9.47
28.6	0.3	1.74×10^{-9}	76.6	1.92×10^{-10}	4.9	7.13×10^{-12}	0.988	9.29×10^{-1}
	0.03	1.74×10^{-9}	76.9	1.93×10^{-10}	4.9	7.14×10^{-12}	0.990	6.20×10^{-2}
	DI water	1.74×10^{-9}	76.9*	1.92×10^{-10}	4.9	7.16×10^{-12}	0.990	$<1 \times 10^{-2}$
	30	8.88×10^{-10}	37.2	1.90×10^{-10}	4.8	3.43×10^{-12}	0.926	8.44×10^{1}
	3	1.51×10^{-9}	66.2	1.63×10^{-10}	3.6	4.56×10^{-12}	0.965	1.31×10^{1}
47.6	0.3	1.60×10^{-9}	70.2	1.67×10^{-10}	3.7	4.65×10^{-12}	0.979	1.25
	0.03	1.60×10^{-9}	70.3	1.85×10^{-10}	4.6	4.72×10^{-12}	0.992	8.94×10^{-2}
	DI water	1.60×10^{-9}	70.3*	1.80×10^{-10}	4.6	4.69×10^{-12}	0.993	$<1 \times 10^{-2}$

Plots of the water relaxation as a function of frequency can be found in Figure 41. The concentration dependence is shown in Figure 41A, and the temperature dependence is shown in Figure 41B. The temperature dependence of the relaxation time was expected to be Arrhenius, based on reaction rates, but instead displayed a Vogel-Fulcher-Temman relation, which is used to fit the α-relaxation in materials like glasses [95]. The effect of increased ion concentration shifts the relaxation time to higher frequencies, as well as lowers the overall permittivity of the measured water [94].

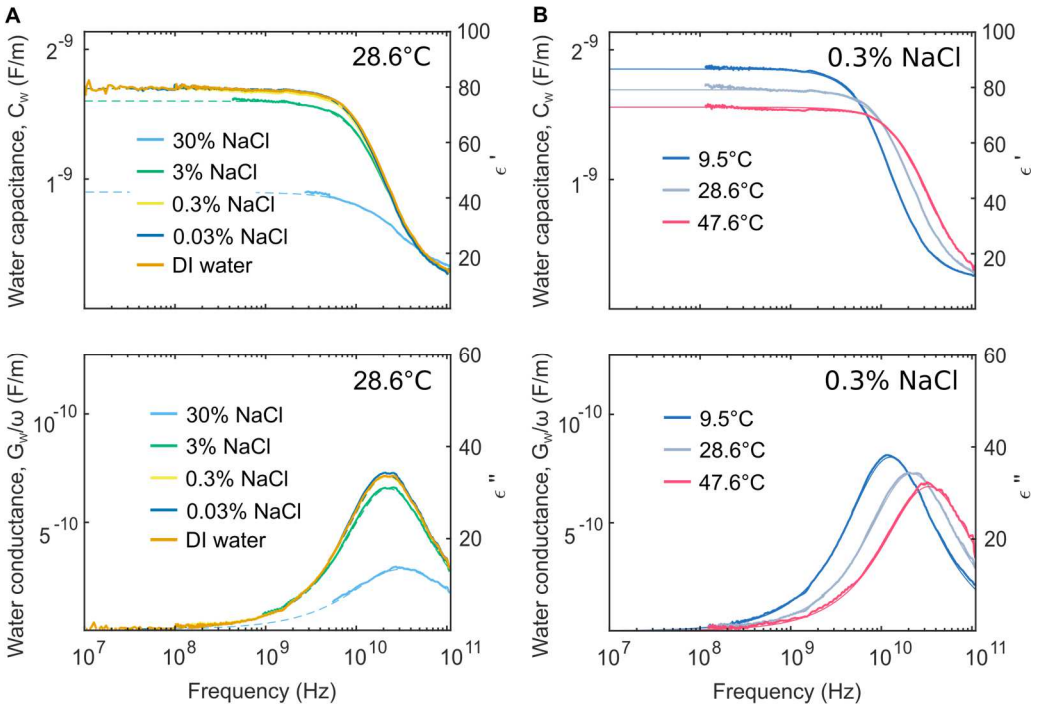

Figure 41. Water admittance per unit length. (A) water admittance per unit length with NaCl concentrations at a temperature of 28.6℃. (B) Change in water admittance per unit length with temperature for a concentration of 0.3% NaCl by weight. Permittivity values on the right hand vertical axes are calculated based on the dimensionless geometrical parameter *k* introduced in the main text.

As we mentioned previously, the intrinsic fluid conductivity of the saline solutions relates to the conductivity parameter (G_σ) through the following expression: $\sigma = kG_\sigma$ (Table 3).

Table 3. The measured ionic conductivity of saline solutions (σ) for all concentrations and temperatures calculated with the dimensionless geometric factor *k*.

Temp (°C)	W_{NaCl} (%)	σ (S/m)
9.5	30	1.71 x10^{1}
	3	2.58
	0.3	2.44 x10^{-1}
	0.03	1.66 x10^{-2}
	<0.01	< 1 x10^{-2}
28.6	30	2.681 x10^{1}
	3	3.91
	0.3	3.841 x10^{-1}
	0.03	2.561 x10^{-2}
	<0.01	< 1 x10^{-2}
47.6	30	3.491 x10^{1}
	3	5.40
	0.3	5.181 x10^{-1}
	0.03	3.691 x10^{-2}
	<0.01	< 1 x10^{-2}

5.4.2 Modeling the Double-layer Admittance

We solved Equation 11 for Y_{EDL} (Figure 39A), using the calculated value of Y_f for each fluid sample. The extracted EDL admittance data were analyzed in the region below the frequency limit where Y_{tot} deviated from the fit of Y_f by more than 2%, i.e. where EDL effects begin to have a measurable effect. As shown in Figure 40A, we modeled the EDL admittance (Y_{EDL}) as two parallel components (Figure 39A): the primary component of the EDL response is a Debye-type relaxation, with admittance: $Y_D = C_D + i\omega G_D$, and a second parallel contribution which we describe as a constant phase element Y_{CPE}. The accumulation of ions at the surface of the electrodes result in a capacitance (C_D), with an associated conductivity term (G_D), which describes the immobility of the ions in proximity to the electrode surface.

Like the Debye-type relaxation of water, Y_D can be approximated by the Cole-Cole function, with an associated relaxation time constant τ_D, and broadening shape parameter α_D. The resulting expression for Y_{EDL} is then:

$$Y_{EDL} = Y_{CPE} + Y_D = Y_{CPE} + i\omega \frac{C_D}{1 + (i\omega\tau_D)^{1-\alpha_D}},$$

Equation 13. Model for the EDL impednace (Y_{EDL}), where the primary component can be modeld as a Debye-type relaxation (Y_D), in pararllel with CPW effects (Y_{CPE}).

Our analysis suggests that there is a second component to Y_{EDL}, which we show can be described with a constant phase element (CPE), with admittance Y_{CPE}. This additional admittance term becomes important at lower frequencies for higher conductivity solutions. The CPE contribution has most commonly been attributed to the electrode surface topography, i.e. surface roughness or porosity [88]. More recently, the CPE has been attributed to atomic scale inhomogeneities [96]. Regardless of physical interpretation, we observe a power-law frequency dependence in our data that can be modeled with a CPE term:

$$Y_{CPE} = Q\omega^{-n} e^{i\frac{\pi}{2}n},$$

Equation 14. Theoritical expression for the constant phase element (CPE) impedance (Y_{CPE}).

where Q and n are fitting parameters, and where Q has the units [S m^{-1} Hz^n] [97]. The inclusion of Y_{CPE} in the model (Equation 13) was essential for getting an accurate fit of Y_{EDL} over all frequencies and concentrations, and for an accurate determination of the time constant τ_D. The resulting parameters from our fit of extracted Y_{EDL} data, for all NaCl concentrations and all temperatures, using Equation 13 and Equation 14, can be found in Table 4. The results for all fits to Y_{EDL} were within measurement uncertainties.

Table 4. Parameters obtained from the fit of electrical double-layer (EDL) admittance vs. frequency (Equation 13). The label "fixed" indicates that a parameter was held fixed while fitting the low concentration data using values from a previous fit of W_{NaCl} = 3% data.

Temp (°C)	W_{NaCl} (%)	C_D (F/m)	τ_D (s)	$1-\alpha_D$	Q (S m^{-1} Hz^n)	n	ϕ (°360)
9.5	30	1.91x10-6	2.9x10-8	0.89	3.7x10-6	-0.92	82.80
	3	2.25x10-6	1.8x10-7	0.79	8.7x10-7	-0.99	89.10
	0.3	Fixed	2.0x10-6	Fixed	Fixed	Fixed	Fixed
	0.03	Fixed	4.2x10-5	Fixed	Fixed	Fixed	Fixed
28.6	30	1.93x10-6	1.6x10-8	0.83	3.0x10-6	-0.92	82.80
	3	2.02x10-6	1.1x10-7	0.79	7.8x10-7	-0.99	89.10
	0.3	Fixed	1.1x10-6	Fixed	Fixed	Fixed	Fixed
	0.03	Fixed	2.5x10-5	Fixed	Fixed	Fixed	Fixed
47.6	30	1.87x10-6	1.1x10-8	0.87	2.3x10-6	-0.93	83.70
	3	1.93x10-6	7.4x10-7	0.81	1.2x10-6	-0.97	87.30
	0.3	Fixed	8.0x10-6	Fixed	Fixed	Fixed	Fixed
	0.03	Fixed	1.5x10-5	Fixed	Fixed	Fixed	Fixed

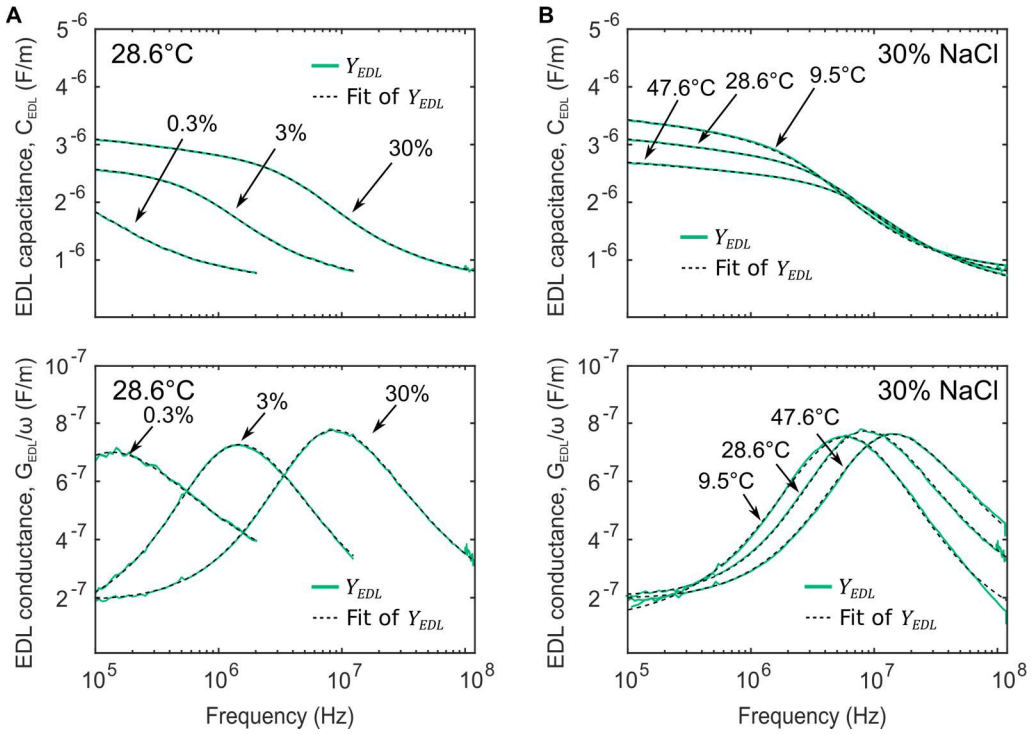

Figure 42. Extracted EDL admittance per unit length and fit. (A) Electrical double layer (EDL) admittance per unit length for different NaCl concentrations at 28.6℃. (B) Electrical double layer (EDL) admittance per unit length for different temperatures for a concentration of 30% NaCl by weight.

We were only able to accurately model Y_{CPE} effects for W_{NaCl} = 30% and 3% solutions, which have a relaxation frequency τ_D that was well above our minimum measurement frequency of 100 kHz. At lower concentrations, the contribution of CPE effects occurred at frequencies below the range used in these measurements. For these lower concentrations (W_{NaCl} = 0.3% and 0.03%), we held C_D, α_D, Q, and n fixed using values from the fit of W_{NaCl} = 3% data, while allowing τ_D to vary. This method produced fits for the W_{NaCl} = 0.3% and 0.03% solutions that were comparable in goodness of fit to the W_{NaCl} = 30% and 3% solutions. The phase of the CPE is given as: $\phi = -n\frac{\pi}{2}$, where a purely capacitive effect has a phase of $\phi = \frac{\pi}{2}$ (90°). The phase angle of the CPE in our measurements was found to be ~83° for the W_{NaCl} = 30% solution, and ~88°for the W_{NaCl} = 3% solution and lower concentrations. A similar study of EDL effects in CPW devices performed by Hong et al. reported a CPE phase angle of ~76° [98].

The fitting procedure described above yields an experimentally determined frequency ($1/2\pi\tau_D$) that separates an EDL-dominated regime from a regime that reflects intrinsic fluid properties. This time scale, τ_D, was interpreted as the characteristic charging time associated with the EDL, which was expected to be inversely proportional to solution conductivity [84]. To test the dependence on the solution conductivity, we show in Figure 43 that the results of a linear regression ($\tau_D = A\sigma^a$, where A and a were fitting parameters) for all NaCl concentrations and all temperatures. This linear regression produced the values of A = 6.0±0.2x10^{-7} (F/m) and a = -1.0±0.05, confirming our expectations that $\tau_D \propto \sigma^{-1}$.

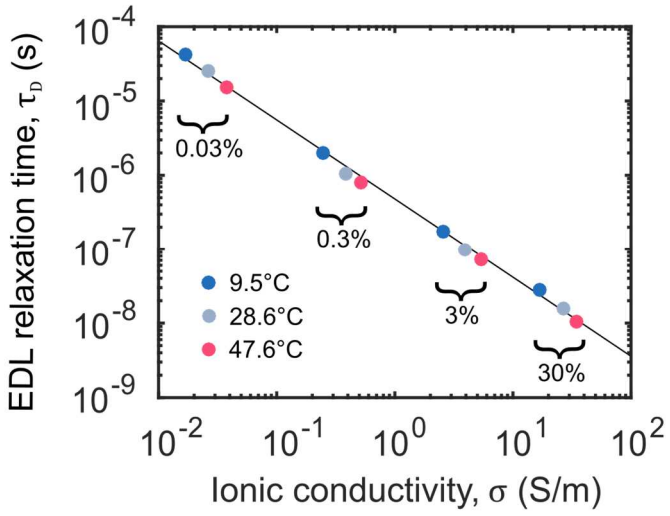

Figure 43. The electrical double-layer (EDL) relaxation time constants (τ_D) vs. ionic conductivity (σ) for all NaCl concentrations and for all temperatures. A power law was used to fit the data.

These results demonstrate that the frequency dependence of the EDL admittance can be accurately modeled with a time constant that can be predicted based on the ionic conductivity of the solution. To further illustrate this point, we show the Y_D contribution to the EDL admittance for all temperatures and concentrations (Figure 44), which we plotted as a function of frequency scaled by the experimentally determined relaxation frequency τ_D. The collapse of the data for all concentrations and temperatures implies a single mechanism that gives rise to the Y_D response, which can be accurately predicted by the solution conductivity. This in turn suggests that device-dependent EDL effects in

microfluidic-based impedance measurements and sensors can be quantified by a single measurement of a fluid of known conductivity.

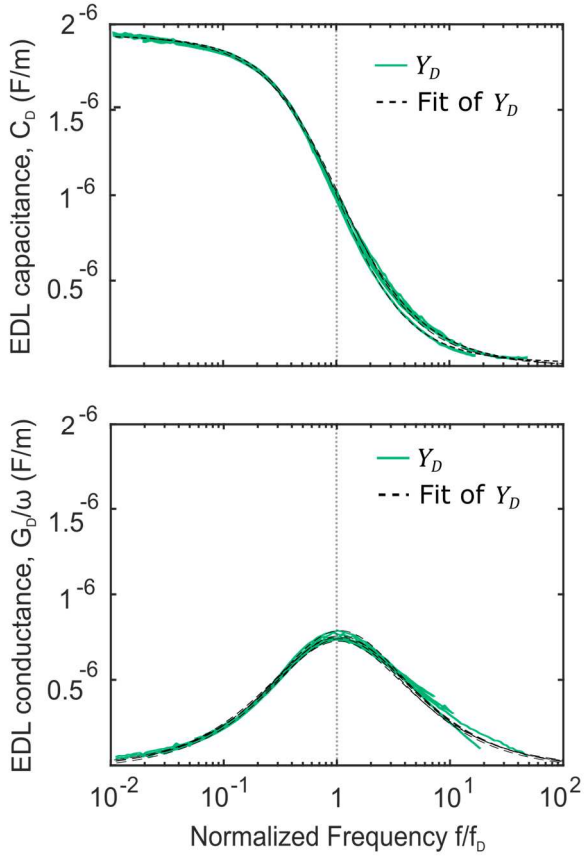

Figure 44. Extracted Debye relaxation component of the electrical double-layer (EDL) admittance with fit ($Y_D = Y_{EDL} - Y_{CPE}$) for W_{NaCl} = 30%, 3%, and 0.3%, for temperatures of 9.5 °C, 28.6 °C, and 47.6 °C. Data is normalized to the EDL relaxation frequency $(2\pi\tau_D)^{-1}$.

6 Magnetic Measurements

In addition to measuring the dielectric and ionic properties of fluids, we are also interested is using our devices to measure magnetic properties. Both nuclear and electron resonances occur in the frequency range in which we operate. In theory, our devices and calibrations should be simultaneously sensitive to both the electrical magnetic properties of materials within our channels, potentially offering more information in every test. However, this fact also means we need to disentangle electric and

magnetic effects, potentially complicating the measurements. In Chapter 5 we were able to extract the permittivity of the materials only by assuming that the permeability of the sample was the same for both the bare CPW sections and the fluid filled channel sections, i.e. in both cases $\mu_r = 1$. For samples with frequency dependent permeability and permittivity however, we can no longer make such an assumption.

I will refer to materials with both magnetic and electric properties as composite materials. Composite materials (some time referred to as nano-composites [99]) have some discrete portion of magnetic and dielectric or ionic parts. Magnetoelectric materials, are a sub-class of composite materials where the magnetic properties couple with the electric properties of the material; one method to achieve this coupling is by ferroelectric materials [100]. Magnetoelectrics are typically solids; however, we should not discount the possibly that coupling between magnetic and electric properties may occur in some composite fluids. There are many natural composite fluids, an example of which is whole blood. Whole blood consists of dielectric components in the form of polar molecules (primarily water) and dissolved ions (the salinity of the blood is ~1% by weight, on the order of sea water; 65% of its ions are NaCl [101]). At lower frequencies (<300 MHz), ion buildup on interfaces results in interfacial polarization[102,103]. The various cell types and inter-cellular structures produce complex permittivity spectra, where each relaxation peak corresponds to a characteristic length scale [102].

Blood is also magnetic; water itself is diamagnetic. Additionally, blood contains metalloproteins, a generic term for any protein that contains a metal ion cofactor. Some of these metal ions are magnetic, such as the Fe^{3+} in transferrin or the Fe^{2+} in hemoglobin, both detectible through EPR. There are also biogenic forms of magnetic nanoparticles, solid aggregates of magnetic components such as ferritin containing mineralized ferrihydrite ($(Fe^{3+})_2O_3 \bullet 0.5(H_2O)$) or malaria, which produces hemozoin crystals (discussed previously in Section 1.1.2). These natural magnetic nanoparticles have a much larger

magnetic signature than metalloproteins. Quantitative measurement of biological fluids with composite properties, like blood, will require separation of magnetic and electric effects.

6.1 Measuring Magnetic Resonance of Nanoparticles

At high concentrations, bulk fluid containing both synthetic and biogenetic magnetic nanoparticles is referred to as a ferrofluid. In this section, we show how the broadband CPW-VNA method can be used to measure synthetic magnetic nanoparticles in water. Later in Section 6.2 we explore the subtleties of the interdependence of electric and magnetic effects.

The frequency range covered by our measurements includes the typical ranges for nuclear magnetic resonance (NMR) as well as the electron paramagnetic resonance (EPR) and ferromagnetic resonance (FMR) regimes. Given the weak magnetic fields used in this work ($B_0 < 500$ mT), and the narrow line width of the NMR signal compared with EPR resonances, it would be difficult to simultaneously detect EPR and NMR signals[104]; Here, we concentrate on EPR and FMR effects.

Although the CPW-VNA method has been previously used to measure the magnetic resonance of nanoparticles in dried powders, the use of the CPW-VNA approach to measure magnetic nanoparticles in a fluid environment is unexplored to our knowledge. The VNA-based (broadband) method has the potential to provide more information about the particles than the cavity EPR method (narrow band). A broadband approach can render the complex resonance response (both μ' and μ'' vs. only μ'' in cavity EPR), as well as sweeping both magnetic field and frequency to give information such as the magnetic dampening ratio. Lastly, as already stated many times, microfluidics provides a convenient platform for point-of-care applications.

Magnetic resonance measurements like EPR and FMR require a large static external magnetic field (B_0) to stimulate the magnetic resonance (see Section 2.2.6). Although it is possible to sweep the frequency or the magnetic field to determine magnetic resonance, magnetic field-swept measurements are generally preferred for both EPR and FMR. Frequency-swept measurements are difficult because, without calibrations, frequency-swept measurements result in a convoluted frequency response. The complexity of broadband CPW-VNA measurement makes background-subtractive difference measurement impossible. Measurements swept across the magnetic field (field-swept), however, allow for difference measurement. Field-swept measurements produce a cleaner, less ambiguous magnetic resonance response. However, field-sweeps are slow, requiring bulky electromagnetics that often need cooling systems and can present difficulty in measuring precise field values.

Commercial cavity-resonator EPR spectrometers are traditionally used to measure the resonance spectra of small molecule radicals, which have narrow resonance lines with ~5 mT. These systems can also be used to measure the broader resonance peaks of super-paramagnetic nanoparticles (~200 mT). In the following, we reproduce cavity-EPR measurements of the magnetic nanoparticles using the CPW-VNA method.

6.1.1 Samples and Methodology

Here we chose to measure magnetic nanoparticle called ferumoxytol (Feraheme), suspended in water. In addition, we measured the molecular free radical TEMPO (2,2,6,6-tetramethylpiperidine1-oxyl), also suspended in water. TEMPO has a narrow resonance, and therefor useful for determining the field resolution of the measurement. Ferumoxytol was chosen for this study because of its commercial availability, stability in water, and particle-agglomerating organic shell. X-ray diffraction showed that the cores of the Ferumoxytol nanoparticles have a diameter of 6 ± 0.5 nm, i.e. they are likely to be super-paramagnetic. Particles that are too large lose their super-paramagnetic properties. SQUID magnetometry

confirmed that the particles are indeed super-paramagnetic, with a blocking temperature of 23 ± 5 K and a non-hysteretic response.

These first generation of devices consisted of CPW structures fabricated on high-resistive (>18 kOhm) silicon <100> substrates (375 µm thick, with a relative static permittivity of ~11.7). The CPW layer consisted of 4 nm Ti and 600 nm Au, deposited with electron-beam evaporation. CPWs had 100 µm center-conductor (W_{CC}), and 50-µm gap width(W_{gap}) (Figure 45A).

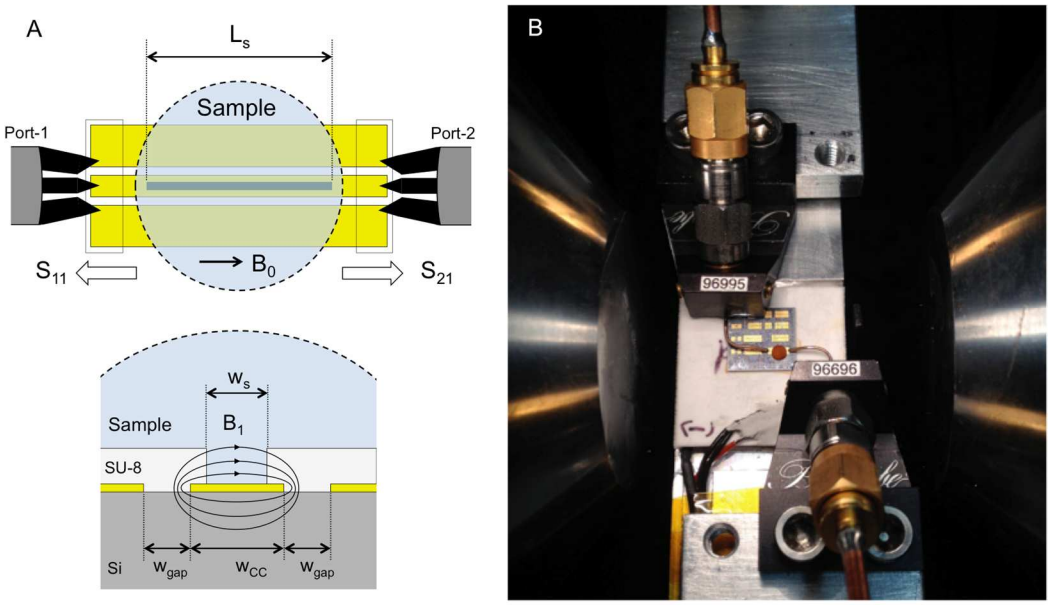

Figure 45. A) Top and cross-sectional view of wave-guide with sample drop. B) Image of experimental setup.

Rather than using microfluidics, the device worked with a drop of liquid sample placed directly over the waveguide. We patterned 25.6 µm of SU-8 over the CPW structures. The SU-8 was patterned to leave an area on either side for probing and a fluid well area over the center conductor (Figure 45A). SU-8 helps isolate the location of the sample so that the measurement is less affected by the size and shape of the sample drop. By spacing the sample away from the gaps of the CPW (where the AC field geometry is more complex), we were better able to approximate AC field geometry at the sample location. During measurement, the sample will experience a B_1 field horizontal to the substrate, perpendicular to the

direction of propagation along the CPW, and perpendicular to the external B_0 field. Due to the constrained geometry of the external magnet we incorporated right-angle microwave probes.

We applied ~2 mm diameter drops of sample fluids onto the surface of the chips by micro-pipetting. Measurement chips were positioned on top of a Peltier device to control the temperature of the chip and sample. Due to the small thermal mass of the chip and sample, the Peltier devices were capable of rapidly heating and cooling the sample between a range of -20 °C and 60 °C. Samples could be measured in liquid form or frozen to facilitate anisotropy measurements. One of the main drawbacks to using the drop method instead of fully enclosed microfluidic devices is that the small fluid volumes evaporate rapidly, during the course of measurement. This challenge informed future methods.

To keep the particles close to magnetic saturation, we needed to work in a magnetic field range greater than 10 mT. This corresponds to a resonant frequency in the 1-15 GHz range. Liquid water has increased power loss centered around ~20 GHz. This reduces sensitivity by decreasing the power delivered to the particles. Frozen water molecules are immobile and reduce the overall power loss. Realizing this, we froze the samples under field (1 T) to preserve the configuration of the nanoparticles while dramatically improving the signal-to-noise ratio of our measurements. We also measured dried particles, letting a drop dry over the SU-8 well.

We have discussed how microwave calibrations are important for microwave spectroscopy measurements. However, full on-chip microwave calibrations are rarely used in the literature for CPW-VNA-based FMR, nor did we employ them in our initial work. However, we did perform coaxial calibrations to de-embed measurements up to the beginning of microwave probing. Even with these calibrations, we found distortions in the partially-calibrated measured S-parameters. To increase signal-

to-noise ratio, we chose the frequency at which reflections were lowest (9.35 GHz) to perform a field-swept measurement.

Cavity-EPR systems measure the magnetic resonance relative to the power absorbed by the sample. The magnetic resonance peak represents the sample's peak power absorption. The power absorbed through magnetic resonance is directly related to imaginary susceptibility (χ''), which relates to permeability ($\mu_r'' = \chi'' + 1$). As discussed throughout this dissertation, the principle challenge of broadband on-chip microwave measurements is in relating measured VNA S-parameters to the sample's EM properties, the permeability and susceptibility.

The literature on VNA-FMR takes two distinct approaches to evaluating complex susceptibility by measured S-parameters: the lumped element model and the distributed circuit model. The distributed circuit model approach was already described in Section 2.3, with the circuit parameters RLCG continuously distributed along the line; This is also sometimes referred to as "Barry analysis" in the FMR context [5,105]. The lumped element model, Derived by Ding et al. [2], treats the transmission line as an idealized single lumped electrical circuit element; RLCG are not PUL quantities, but lumped into a single electrical element. The susceptibility of the sample is related to changes in the impedance of the lumped element, which relates in turn to changes in the measured S-parameters. The distributed model is inherently more accurate.

The simpler lumped-element model commonly approximates complex susceptibility as proportionally related to the change in s-parameters with magnetic field (ΔS_{21} or ΔS_{11}) [2–4,106,107,17] where Re[ΔS_{21}] or Re[ΔS_{11}] correspond to the χ'' and Im[ΔS_{21}] or Im[ΔS_{11}] correspond to χ'. Simplifications of the two previously stated models show this to be approximately valid in cases where the initial

reflections are relatively low and the transmission is relatively high, i.e. a well matched low-loss waveguide.

Both the lumped and distributed element models require some amount of calibration. They also require that probes be placed equidistant from the sample [5]. In reality, on-chip measurements are highly dependent on calibrations. Failing to properly de-embed the sample will distort the extracted line shape of the susceptibility produced by both the lumped and disturbed models, the result of which will be some convolution of χ' and χ''.

Our ad-hoc solution, without using an on-chip calibration, was a power conservation approach [42]. The imaginary magnetic susceptibility is directly related to the power absorbed by the sample from magnetic interactions in a distributed circuit model approach. By accounting for the power transmitted and reflected, and by making analytical assumptions about the field distribution at the sample's location, we can approximate χ''. The expressions below for χ'' are a unique contribution by the author (Equation 15) [42].

$$\chi'' \cong \left(\frac{4Z_0 w^2}{f\mu_0 A_s L_s}\right) Y$$

$$Y = \left(\frac{2ln|S_{21_{HF}}|}{|S_{21_{HF}}|^2 - 1}\right)\left(|S_{11_{LF}}|^2 - |S_{11_{HF}}|^2 + |S_{21_{LF}}|^2 - |S_{21_{HF}}|^2\right)$$

Equation 15. Power conservation model, where Z_0 is the impedance of the line, w is the width of the center conductor, A_s is the coss-ssecitonal area of interaction, and L_s is the length of the SU-8 well.

6.1.2 Results and Conclusion

Figure 46 shows a comparison between the measured magnetic resonance spectra for dried TEMPO using the on-chip technique and that obtained from a commercial cavity EPR system (The cavity EPR system was operated at 9.35 GHz, with a TE_{102} cavity, 0.4 mW microwave power, and 100 kHz AC field modulation). The TEMPO samples measure the field resolution of the on-chip measurement (~1 mT). The offset between on-chip and cavity measurements stemmed from slight differences in RF frequencies used in the cavity-EPR system and on-chip method. We can now resolve narrow resonances. We also found that the line-width of the resonance, as measured by the on-chip (on-wafer) method, is comparable to that measured by the conventional cavity-EPR system.

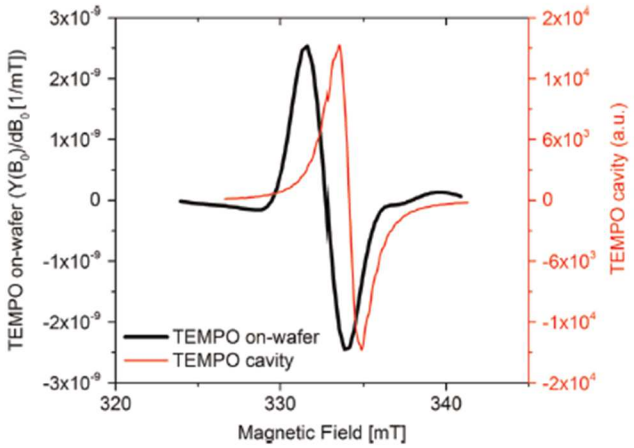

Figure 46. Cavity and on-chip magnetic resonance spectra of dried TEMPO with excitation frequencies of 9.35 GHz and 8.6 GHz.

Comparison of the magnetic resonance of frozen of ferumoxytol in a commercial cavity-EPR systems with the on-chip method concur with line width measurements. However, the cavity-EPR measurement showed a slight asymmetry in the resonance peak (Figure 47). When the samples are frozen in field, the water crystals that form during freezing can physically break magnetic symmetry. This causes random asymmetries in the magnetic resonance spectrum.

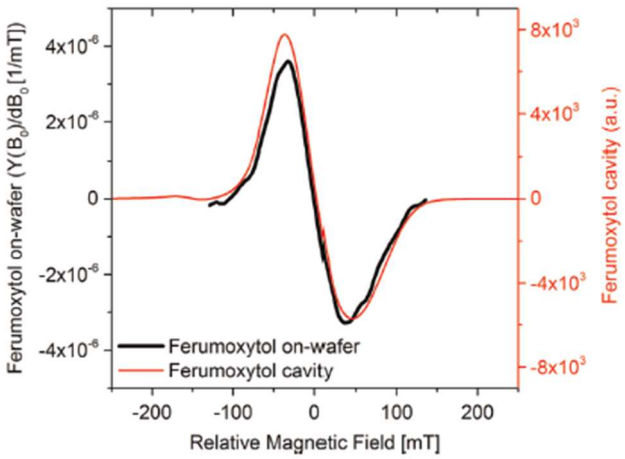

Figure 47. Cavity and on-chip magnetic resonance spectra of frozen 10% concentration ferumoxytol with excitation frequencies of 9.35 GHz and 8.6G Hz.

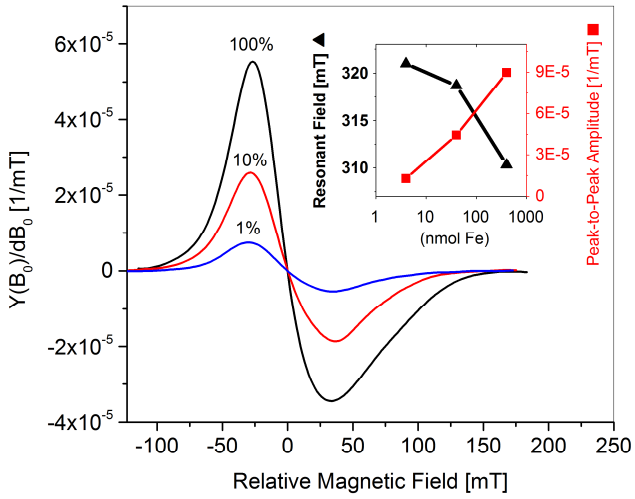

Figure 48. Concentration dependence of dried films of ferumoxytol with excitation frequency of 8.6G Hz. The inset shows that the resonance field decreases and the peak-to-peak amplitude increases as the concentration of particles increases.

The on-chip VNA-FMR method proved as effective in reproducing similar EPR spectra as those measured by the cavity-EPR system. These measurements had a minimum sensitivity of ~1 nmol of spin. The power conservation model is an alternative to the existing distributed and lumped element approximations, and gives a phase-independent estimation of the absolute magnitude of the imaginary part of the magnetic susceptibility. However, we could get both better sensitivity and more information if we used microwave calibrations to isolate the response of the sample.

6.2 Separating Permittivity and Permeability

We have shown in the previous section that we are able to detect weak magnetic resonances with the CPW-VNA technique by measuring low concentrations of magnetic nanoparticles. In Section 6.1 we used a power conservation model to relate measured S-parameters to imaginary susceptibility, and thus to imaginary permeability. The power conservation model is an approximation, and only gives limited information. In this section, we will investigate how to use microwave calibrations to experimentally

extract accurate quantitative values for the complex permittivity and permeability. We want to expand upon our linear approximation made in Section 4.3 to experimentally determine the relationship between the measured distributed circuit parameters RLCG and complex permittivity and permeability. This requires ideal samples with both a dielectric and magnetic responses. We also want materials with a strong and clear resonance. Magnetic thin-films, typically measured in FMR, are ideal for continuing our investigation into complex permittivity and permeability.

6.2.1 Sanity Check with YIG Film

We started by measuring a 1 μm thick film of Yttrium Iron Garnet ($Y_3Fe_5O_{12}$, YIG) grown on a gadolinium gallium garnet ($Gd_3Ga_5O_{12}$, GGG (111)) substrate. YIG is a well-known ferromagnetic insulator with extremely low magnetic damping that has been widely used in microwave devices and thoroughly measured in the past with FMR techniques [108]. Here, a YIG film was centered over a CPW line, and the difference in transmission (ΔS_{21}) measured for different external magnetic field strengths (B_0). In this measurement, no calibration was used. We used two adjustable permanent magnetics in a magnetic yoke to create our B_0 field. By adjusting the distance between the poles we are able to increase or decrease B_0. This setup is more compact than an electromagnet, which requires water-cooling. The permanent magnet setup produces a strong magnetic field (~611 mT at 1 inch pole separation), as well as a homogeneous field in the region of interest. Permanent magnets also increase the utility of the measurements for point-of-care applications.

We chose to measure YIG as a proof-of-concept to understand the sensitivity of our measurement, and to determine the B_0 field strength as a function of permanent magnet separation (A.K.A. pole piece separation). The magnetic resonance of the YIG film can be used as a magnetic field standard for relating resonance frequency to B_0. For FMR films, we can get the relationship between

magnetic field (B_0) and the resonance frequency (f_{res}) using the Kittel equation [17], given for an in-plane field geography by:

$$f(B_{res}) = g\frac{\mu_B}{h}\sqrt{[B_{res} + B_k^a(\theta)][B_{res} + B_{eff} + B_k^b(\theta)]},$$

Equation 16. The Kittel equation.

where B_{res} is the external resonant magnetic field at a given frequency, μ_B is the Bohr magneton, *h* is Planck's constant, and B_k^a and B_k^b are the shape anisotropy fields for the two dimensions in plane (*a* and *b*) which depend the angle of the field. The effective field $B_{eff,}$ i.e. the in-plane field, is given by the following equation:

$$B_{eff} = B_{sat} - \frac{2K\mu_0}{B_{sat}} = B_{sat} - B_{OOP},$$

Equation 17. The Kittel equation, effective field.

where K is the perpendicular (out-of-plane) anisotropy energy density, which gives the out-of-plane magnetization (B_{OOP}). Equation 17 implies that any out-of-plane magnetization has the affect of reducing the in-plane saturation magnetization. We used literature values for B_{OOP}, with B_{OOP} = 27.5 mT for a 56 nm thick film of YIG [109], and B_{OOP} = 370 μT for a 6 μm thick film [108]. The effective magnetization (B_{eff}) of these films were measured as 144 mT for the 56 nm film [109], and 164 mT for the 6 μm film [108]. This gives a saturation magnetization of B_{sat} = 170 ± 2 mT for YIG.

The anisotropy fields in the Kittel equation (Equation 16) add complexity to the measurement. However, because the film is oriented in the (111) direction, crystalline anisotropy is minimal. Additionally, we are measuring an un-patterned film, and there is also no shape anisotropy in-plane. If we assume that the shape anisotropy is negligible, the Kittle equation reduces to the following form:

$$f_{res} \cong g\frac{\mu_B}{h}B_{res} = \frac{\gamma}{2\pi}\sqrt{B_{res}^2 + B_{res}B_{eff}}.$$

Equation 18. The Kittel equation, with no anisotropy.

YIG has a known g-factor (g≈2) [17,108]. In this case $\gamma/2\pi \approx 2.80\text{x}10^{10}$(Hz T^{-1}). This value can be used to approximate the strength of the external magnetic field (B_0) used in our experiments.

Figure 49 shows S-parameter difference measurements of YIG for different field values. As we increase the field we see an obvious shift in the resonance from 1.8 GHz to 6.1 GHz. This corresponds to a change in pole piece separation (D) from the maximum separation of 82 mm to 49 mm (minimum separation), respectively. The magnitude ($|S_{HF} - S_{HL}|$) of the resonance shows a peak, while the phase difference ($\phi_{HF} - \phi_{LF}$) presents sinusoidal line shape; the phase shift should be roughly proportional to the real part of the permittivity. We see a resonance width of ~500 MHz, typical of YIG. Values for B_0 were calculated with Equation 18 (B_0 goes from 22 mT to ~150 mT). These field values are consistent with measured field values using our magnetic field probe (Hall effect probe).

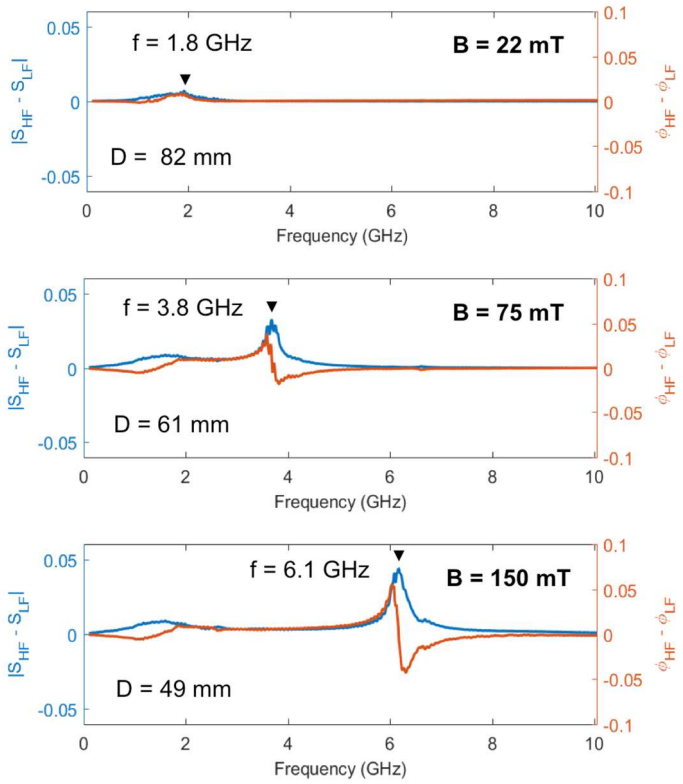

Figure 49. Broadband measurements of Yttrium iron garnet (YIG). Switch term corrected S-parameters in terms of the magnitude difference and phase difference between high B_0 field and low B_0 (4 mT). The values of the resonance frequency (f), magnetic values calculated from Equation 18 field (B), and the pole separation (D), are included.

We see agreement between the YIG and probe estimates of magnetic field strength with pole separation (Figure 50B). The field strength (B) has the following relation to pole separation (D):

$$B = \alpha e^{\beta D},$$

Equation 19. Relationship between field strength (B) and pole separation (D), with fitting parameters α and β.

where $\alpha = 2.74 \times 10^{3}$ and $\beta = -5.91 \times 10^{-2}$.

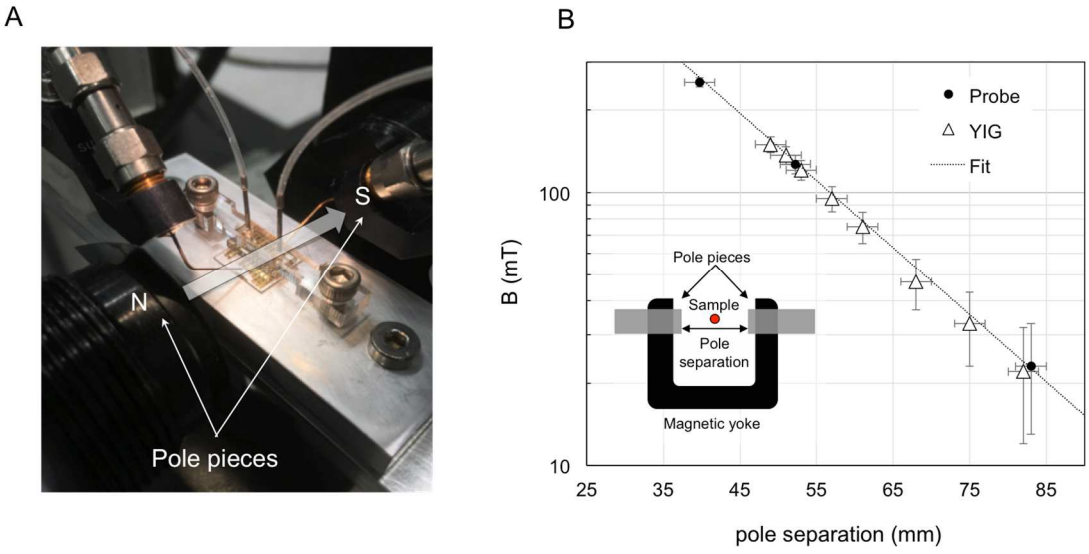

Figure 50. Permanent magnet used to create magnetic field. A) Image of the magnetic measurement set-up showing pole pieces. B) Measurements of magnetic field vs. pole separation from YIG films and Hall effects probe. The fit of the data is given in Equation 19.

6.2.2 Calibrated Measurements of Embedded Permalloy

We can see from the YIG data in Figure 49 that the un-calibrated differences in S-parameters can give a clear resonance response. To measure the intermixing between permittivity and permeability in our extracted RLCG we need to be able to vary both the permittivity and permeability within our channels.

We can change the permittivity simply by exchanging the fluid, i.e. air to water. To give the channels a changing permeability, we add a strip of 10 nm of Permalloy (Py), a material commonly measured in FMR. The Py film is patterned under the center conductor (Figure 51). This is a typical configuration for measuring FMR films, but it has not previously been used in conjunction with microfluidics. By analyzing changes in the Py resonance between water and air measurements we can qualitatively capture the intermixing.

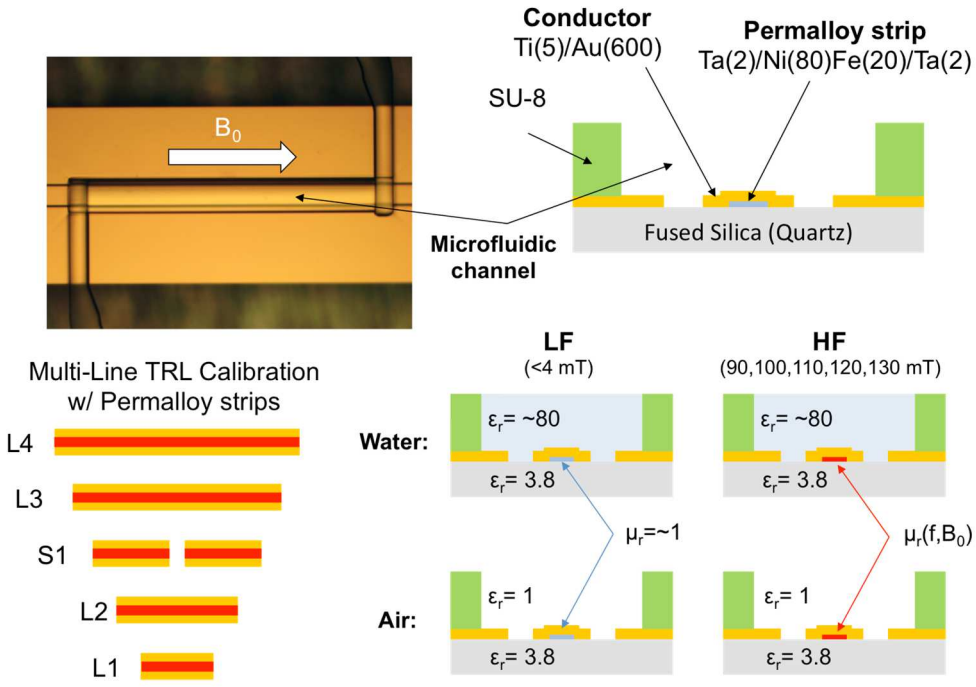

Figure 51. Impeded permalloy devices. Permalloy (Py) strips with thickness of 10 nm were embedded under the center conductor of the CPW lines. The length of the Py strips are present only where there is channel, to perform a MTRL calibration.

The hybrid calibration (Section 3.3) requires the assumption that R and L are constant for all materials placed over the CPW. We were able to assume this previously because all of the materials (SU-8 and liquids) were non-magnetic, and therefore contribute neither to R nor L, which we know from Section 4.3 are roughly proportional to μ'' and μ', respectively. This allows us to extrapolate the impedance measurement from the series resistor to the impedance of the channels. However, to measure

both the magnetic and dielectric response, we can no longer assume that R and L are constant. One option is to modify the ExtractRLCG algorithm (Section 2.4.2), to separate de-embedded measurements into RLCG. However, the algorithm also has some trouble in untangling the electric and magnetic response; for instance, in assigning loss to either R or G. Instead, in this preliminary work, we utilize the MTRL to extract the propagation constant. We are not currently able to determine the impedance, and thus RLCG. We instead compare propagation constants, from high field (HF) to low field (LF). We are lucky that the MTRL calibration has low uncertanties in the frequency regime for EPR and FMR. If we take the ratio of propagation constant from HF to LF (R), we should eliminate any contribution from C and G if C and G don't have any magnetic field dependence, i.e. there is no intermixing (Figure 52).

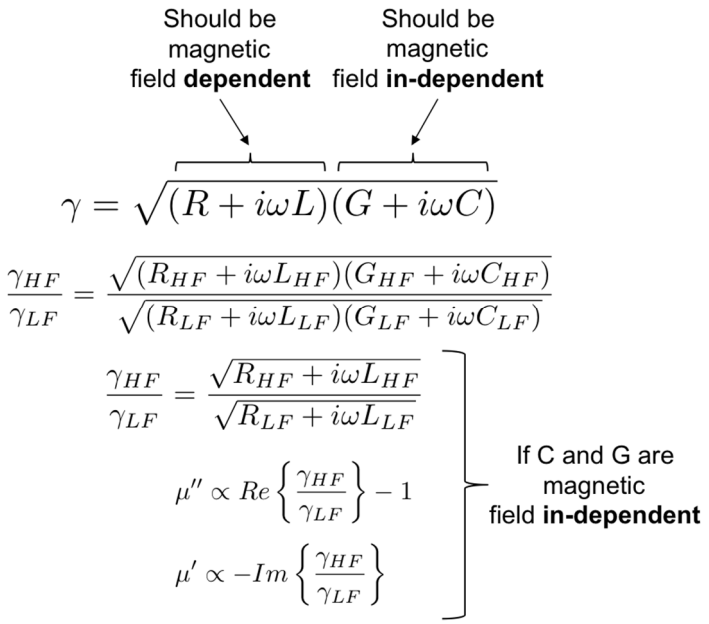

Figure 52. The ratio of propagation constants (γ) for the high magnetic field case (HF) over the low magnetic field case (LF). If *C* and *G* are magnetic field in-dependent, then the ratio can be reduced to a form that is approximately proportional to the real and imaginary permittivity (μ' and μ'').

We measured our composite microfluidic devices at 6 field values (90, 100, 110, 120, and 130 mT (HF) and 4 mT (LF). All recorded field values were direct measurements near the sample location using a Hall effect sensor (field probe). While landed on each MTLR line (L1…L4, S1), the channels were measured with air at each magnetic field value, and then with DI water at each magnetic field value.

Later, the measurements were separated and the MTRL calibration was performed at each field value for air or DI water. In Figure 53, we display the results of the calibrations for air filled channels in terms of the ratio of propagation constants, defined previously. Assuming C and G are magnetic field independent, we can pull out quantities that are approximately proportional to $\mu' and\ \mu''$. The attenuation constant we measure is a calibrated quantity; therefore, what is displayed in Figure 53, should be the undistorted magnetic resonance of the Py strip.

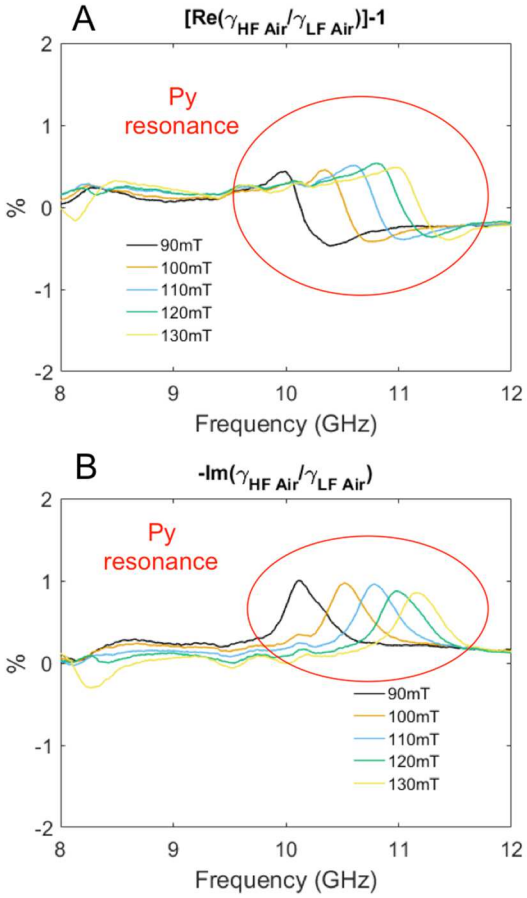

Figure 53. Ratios of propagation constant between high field measurements (130, 120, 110, 100, 90 mT) and low field measurements (4 mT) for air filled channels. The Permalloy (Py) resonance is circled. A) is approximately proportional to the μ'. B) is approximately proportional to μ''.

Increasing B_0 increases the resonance frequency, helping to confirm that what we see in Figure 53 is indeed a magnetic resonance. The field values were labeled based on the values measured by the Hall probe, and correspond to underestimates of the actual field experienced by the permalloy. For the 130 mT

measurement, the pole pieces had a separation distance of 49 mm, which corresponds to a magnetic field of 150 mT as determined by measurements of YIG (Section 6.2.1). Using this magnetic field value, the known g-factor for permalloy (g = 2.2 [5]), and the frequency of the resonance (f_{res} = 11.15 GHz for the 130 mT measurement), we can calculate an effective saturation magnetization (B_{eff} = 694 mT). If we assume a saturation magnetization from the literature (B_{sat} = 597 mT [5]), we get an estimation for the out-of-plane magnetization (B_{OOP} = 97 mT). This value is close to that measured by Beaujour et al. who measured an out-of-plane magnetization of 93 mT [5]. The conclusion is that the magnetic resonance we see in Figure 53 is most likely from the Py strip.

We now turn to a comparison of air vs. DI water. If there is no intermixing between electric and magnetic effects, we should see no evidence of the Py resonance between air and water measurements. To make the comparison, we take the percent difference in the propagation constant ratios between air and water (Figure 54). What we find is that there is no evidence of the Py resonance. This finding indicates experimentally that there is no detectable level of intermixing over ~1% uncertainty.

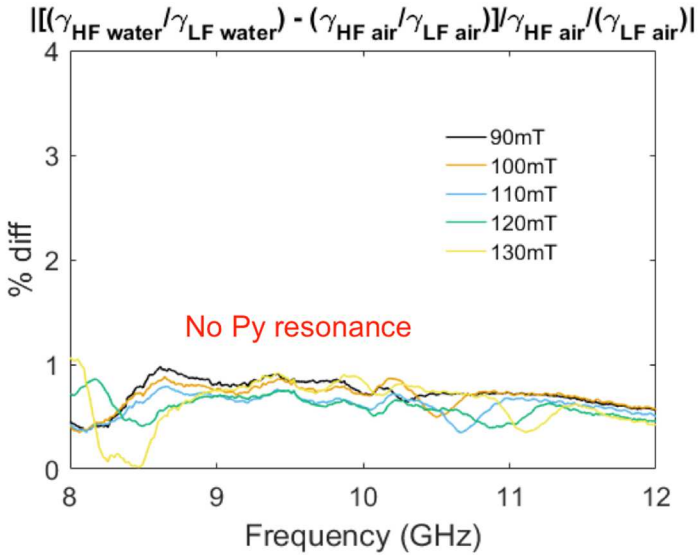

Figure 54. Taking the percent difference between propagation constant ratios for air and DI water filled channels. There should be no sign of the permalloy (Py) resonance if C and G are magnetic field in-dependent.

6.2.3 COMSOL Simulations of Quasi-TEM Field Distribution

In Section 6.2.2 we gave empirical evidence of minimal intermixing between μ and ε in forming RLCG. To explore the idea of intermixing computationally, we employed full-wave (see Appendix-D) COMSOL simulations. In pure TEM propagation, both electric and magnetic fields are exclusively in the transverse plan, i.e. orthogonal to the direction of propagation. Figure 55 shows the results of full-wave COMSOL simulations based on the geometries and material properties of the CPW devices used in this dissertation. The CPW is simulated as having quartz below the CPW, and water above the CPW, at 30 GHz. These criteria are considered a worst-case scenario for the purity of the TEM field distribution. Figure 55A and Figure 55B display the special distribution of the magnitude of the integrand quantity of the transverse and propagation direction components from the capacitance (C) expression of the general wave-guide equations (Equation 8). The distribution is similar in both the transverse and propagation directions, where the fields are strongest in the gaps. It is evident that the transverse component is much stronger than the propagation component. However, the propagation component is non-zero (Figure 55B).

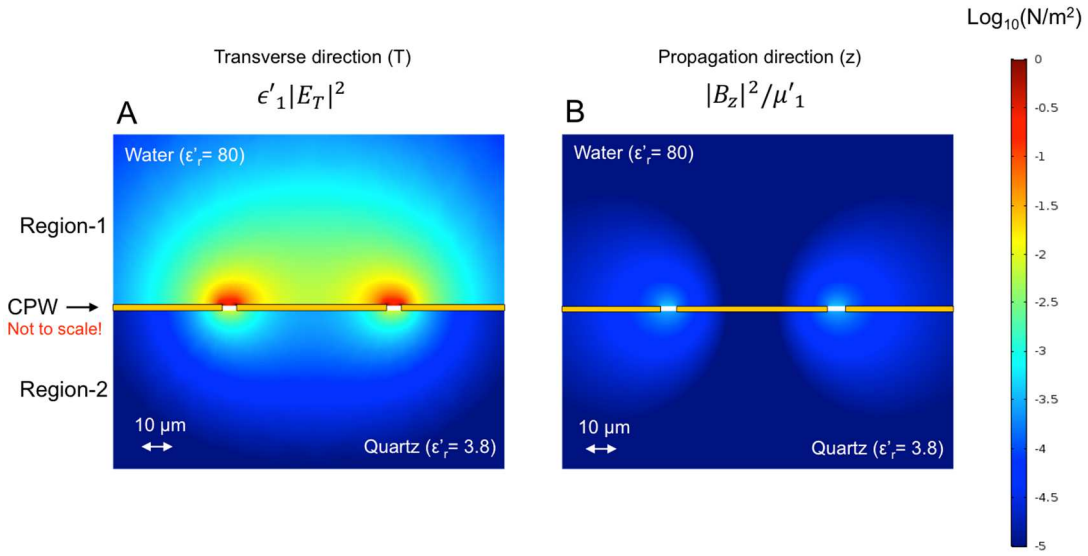

Figure 55. COMSOL full-wave simulations of the spatial distribution of the integrand quantities from the capacitance expression from the general waveguide equations (Equation 8) in both region-1 and region-2, above and below the coplanar waveguide (CPW) respectively. A) The transverse direction (T). B) The propagation direction (z).

In Figure 56 we display the ratio of integrand components in the propagation direction vs. the transverse direction for region-1, above the CPW. If the field distribution were pure TEM, the entirety of region-1 would be zero. However, we see areas of region-1 that have a ratio of greater than 3% deviation from pure TEM. To truly calculate the "TEM-ness" of the field distribution, we need to calculate the full expressions for the transverse and propagation direction components in C in the general waveguide equations (Equation 8), which requires use to take a surface integral. We preform the surface integral in region-1, above the CPW, and take the ratio of the quantities (Figure 56). If we subtract this quantity by one, we get the "TEM-ness" of the field distribution, which comes out to be 98.5%. Considering this is a worst-case scenario, we are confident in our quasi-static simulations from Chapter 4, and of the linear equations relating RLCG to complex μ and ε (Equation 7).

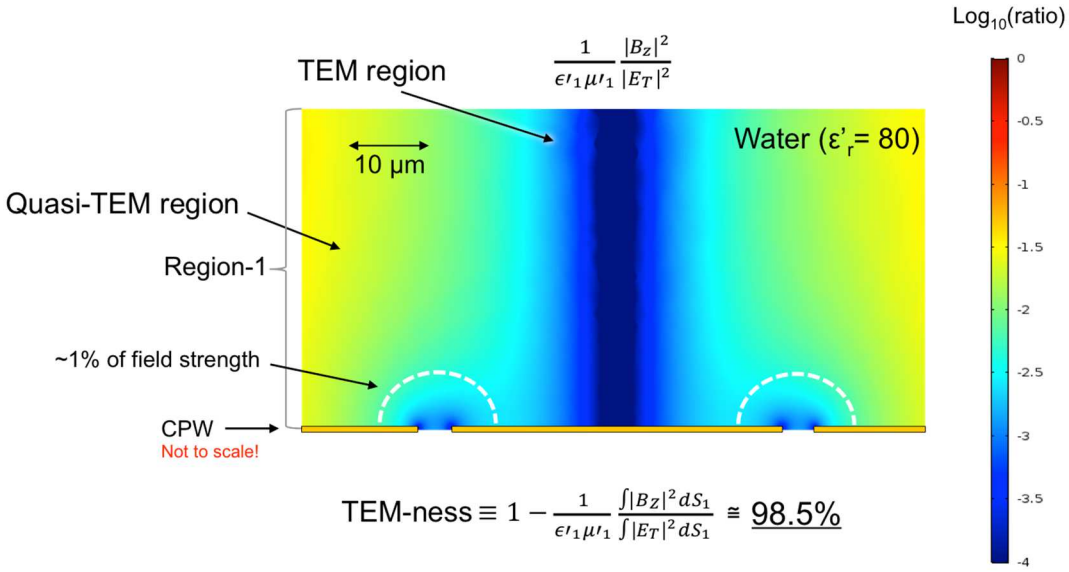

Figure 56. COMSOL full-wave simulations of the spatial distribution of the ratio of the integrand quantities from the capacitance expression from the general waveguide equations (Equation 8), only for region-1, above the coplanar waveguide (CPW). Taking the ratio of the integrals over the entirety of region-1 gives us an estimation for the "TEM-ness", the result being 98.5% TEM.

7 Conclusion and Future Work

7.1 Dissertation Summary

The core of this dissertation is the CPW-VNA measurement technique. In this technique, materials are placed over a coplanar waveguide (CPW). A vector network analyzer (VNA) is used to inject and receive microwaves to and from the CPW. Based on these raw measurements, we can infer the electromagnetic (EM) properties of the material in question. We have added microfluidic channels to the CPW structures, allowing us to measure the EM properties of fluids. We have shown how microwave calibrations can be applied to the CPW-VNA technique to quantitatively extract the distributed circuit parameters RLCG associated with microfluidic channels. We proceeded to show how RLCG relates to the broadband permittivity and permeability of fluids within microfluidic channels.

We have enriched these measurement techniques in three ways:

1) By developing fabrication methods to produce robust microfluidic-microwave devices.

2) By developing microwave calibrations appropriate for fluid measurement.

3) By developing fundamental techniques to relate calibrated CPW-VNA Measurements quantitatively to the permittivity and permeability of fluids, and from properties derive physical properties.

7.2 Envisioned Future Work

In future work we hope to apply this technique a wide variety of aqueous samples. In Chapter 5 we measured ideal saline solutions as a proof of concept. Currently, Dr. Angela Stelson, from our research group at NIST, is utilizing the same devices and methods to measure various molecular cages. Specifically, she is investigating Fe(II) Triazine and Fe(II) SO_3 metal-organic cages in solution. Preliminary results have shown evidence of an ion-pairing relaxation associated with the cages around

100 MHz, similar to ion-paring relaxations seen in large charge polymers such as with negatively charged DNA (referred to as a β relaxation)[110]. The EDL fitting is proving crucial in resolving the ion-pairing peak as without including this peak in the total fit of the data, the EDL is impossible to fit. We are now interested to see if we can resolve a similar ion-pairing peak in the saline solution data. This approach has the potential of being a new metrology technique for resolving the structure of non-covalent interactions between dissolved ions around macromolecules, which has previously been difficult to probe.

The broadband measurement approaches developed here give us more information fluids, making it is easier to extract quantitative permittivity values. Our magnetic measurements (Chapter 6), using the broadband approach, showed low sensitivity to magnetic resonance, relative to narrow-band resonator measurements. In the future, we would like to continue developing simulations of the quasi-TEM nature of the CPW structure. The simulations have preliminarily showed that dielectric discontinuities can lead to AC magnetic fields in the propagation direction, which is relevant for broadband FMR measurements. Using microfluidics, we can change the permittivity above the waveguide, altering dielectric discontinuity and changing the AC magnetic field power in the direction of propagation; we are interested in exploiting this finding in future work.

Bibliography

1. Little, Charles A. E. *et al.* On-wafer Magnetic Resonance of Magnetite Nanoparticles. *J. Magn. Magn. Mater.* 393, (2015).
2. Ding, Y. *et al.* A coplanar waveguide permeameter for studying high-frequency properties of soft magnetic materials. *J. Appl. Phys.* 96, 2969–2972 (2004).
3. Glowinski, H. *et al.* Coplanar waveguide based ferromagnetic resonance in ultrathin film magnetic nanostructures: impact of conducting layers. *ArXiv14025844 Cond-Mat* (2014).
4. Nembach, H. T. *et al.* Perpendicular ferromagnetic resonance measurements of damping and Landé g−factor in sputtered $(Co_2\ Mn)_{1-x}\ Ge_x$ thin films. *Phys Rev B* 84, (2011).
5. Kalarickal, S. S. *et al.* Ferromagnetic resonance linewidth in metallic thin films: Comparison of measurement methods. *J. Appl. Phys.* 99, 093909 (2006).
6. Bilzer, C. *et al.* Vector network analyzer ferromagnetic resonance of thin films on coplanar waveguides: Comparison of different evaluation methods. *J. Appl. Phys.* 101, 074505 (2007).
7. Counil, G. *et al.* Spin wave contributions to the high-frequency magnetic response of thin films obtained with inductive methods. *J. Appl. Phys.* 95, 5646–5652 (2004).
8. Orloff, N. *et al.* Broadband Characterization of Multilayer Dielectric Thin-Films. in *2007 IEEE/MTT-S International Microwave Symposium* 1177–1180 (2007). doi:10.1109/MWSYM.2007.380340
9. Ocket, I. *et al.* Dielectric characterization of biological liquids and tissues up to 110 GHz using an LTCC CPW sensor. in *2013 IEEE Topical Conference on Biomedical Wireless Technologies, Networks, and Sensing Systems* 43–45 (2013). doi:10.1109/BioWireleSS.2013.6613669

10. Grenier, K. *et al.* Integrated Broadband Microwave and Microfluidic Sensor Dedicated to Bioengineering. *IEEE Trans. Microw. Theory Tech.* 57, 3246–3253 (2009).
11. Mateu, J. *et al.* Broadband permittivity of liquids extracted from transmission line measurements of microfluidic channels. in *2007 IEEE/MTT-S International Microwave Symposium* 523–526 (IEEE, 2007).
12. Booth, J. C. *et al.* Quantitative Permittivity Measurements of Nanoliter Liquid Volumes in Microfluidic Channels to 40 GHz. *IEEE Trans. Instrum. Meas.* 59, 3279 to 3288 (2010).
13. Liu, S. *et al.* Hybrid Characterization of Nanolitre Dielectric Fluids in a Single Microfluidic Channel up to 110 GHz. *IEEE Trans. Microw. Theory Tech.* (2017).
14. Liu, S. *et al.* Broadband dielectric spectroscopy calibration using calibration liquids with unknown permittivity. in *84th ARFTG Microwave Measurement Conference* 1–5 (2014). doi:10.1109/ARFTG.2014.7013421
15. Little, C. A. E. *et al.* Modeling electrical double-layer effects for microfluidic impedance spectroscopy from 100 kHz to 110 GHz. *Lab. Chip* (2017). doi:10.1039/C7LC00347A
16. Wen, C. P. Coplanar Waveguide, a Surface Strip Transmission Line Suitable for Nonreciprocal Gyromagnetic Device Applications. in *Microwave Symposium, 1969 G-MTT International* 110–115 (1969). doi:10.1109/GMTT.1969.1122668
17. Shaw, J. M. *et al.* Precise determination of the spectroscopic g-factor using broadband ferromagnetic resonance spectroscopy. *ArXiv13107515 Cond-Mat* (2013).
18. Fannin, P. C. *et al.* Investigation of ferromagnetic resonance in magnetic fluids by means of the short-circuited coaxial line technique. *J. Phys. Appl. Phys.* 28, 2003 (1995).
19. Fannin, P. C. *et al.* Complex susceptibility measurements of a suspension of magnetic beads. *J. Magn. Magn. Mater.* 300, e210–e212 (2006).
20. Hagen, W. R. Broadband Transmission EPR Spectroscopy. *PLOS ONE* 8, e59874 (2013).

21. Lin, S. W. *et al.* Effects of electric and magnetic fields on the resonance frequency of piezoelectric ceramics. *Ferroelectrics* 88, 67–71 (1988).

22. El-Ali, J. *et al.* Cells on chips. *Nature* 442, 403–411 (2006).

23. Shields, C. W. *et al.* Microfluidic Cell Sorting: A Review of the Advances in the Separation of Cells from Debulking to Rare Cell Isolation. *Lab. Chip* 15, 1230–1249 (2015).

24. Velve-Casquillas, G. *et al.* Microfluidic tools for cell biological research. *Nano Today* 5, 28–47 (2010).

25. McAdams, E. T. *et al.* Tissue impedance: a historical overview. *Physiol. Meas.* 16, A1 (1995).

26. Zhu, Z. *et al.* Time-lapse electrical impedance spectroscopy for monitoring the cell cycle of single immobilized S. pombe cells. *Sci. Rep.* 5, 17180 (2015).

27. Schade-Kampmann, G. *et al.* On-chip non-invasive and label-free cell discrimination by impedance spectroscopy. *Cell Prolif.* 41, 830–840 (2008).

28. Gawad, S. *et al.* Micromachined impedance spectroscopy flow cytometer for cell analysis and particle sizing. *Lab. Chip* 1, 76–82 (2001).

29. Yang, L. Electrical impedance spectroscopy for detection of bacterial cells in suspensions using interdigitated microelectrodes. *Talanta* 74, 1621–1629 (2008).

30. Abdalla, S. Complex permittivity of blood cells and E. coli suspensions. *J. Mol. Liq.* 160, 130–135 (2011).

31. Raab, S. S. & Grzybicki, D. M. Cytologic-histologic correlation. *Cancer Cytopathol.* 119, 293–309 (2011).

32. World Malaria Report 2015. (2015).

33. Wongsrichanalai, C. *et al.* Review of Malaria Diagnostic Tools: Microscopy and Rapid Diagnostic Test (RDT). *American Society of Tropical Medicine and Hygiene*, 2007.

34. Ha, S. *et al.* Microfluidic electric impedance spectroscopy for malaria diagnosis. *ResearchGate* 1960–1962 (2012).

35. Sienkiewicz, A. *et al.* Multi-Frequency High-Field EPR Study of Iron Centers in Malarial Pigments. *J. Am. Chem. Soc.* 128, 4534–4535 (2006).

36. Inyushin, M. *et al.* Superparamagnetic Properties of Hemozoin. *Sci. Rep.* 6, (2016).

37. Brémard, C. *et al.* Spectroscopic Investigations of Malaria Pigment. *Appl. Spectrosc.* 47, 1837–1842 (1993).

38. Narayanamurthy, V. *et al.* Microfluidic hydrodynamic trapping for single cell analysis: mechanisms, methods and applications. *Anal. Methods* 9, 3751–3772 (2017).

39. Hernandez, P. NIST General Information. *NIST* (2008). Available at: https://www.nist.gov/director/pao/nist-general-information. (Accessed: 4th October 2017)

40. O'Carroll, A. G. *et al.* The Measurement of the Sea Surface Temperature by Satellites from 1991 to 2005. *J. Atmospheric Ocean. Technol.* 23, 1573–1582 (2006).

41. Guillou, C. *et al.* Impact of new permittivity measurements on sea surface emissivity modeling in microwaves. *Radio Sci.* 33, 649–667 (1998).

42. Little, C. A. E. *et al.* On-wafer magnetic resonance of magnetite nanoparticles. *J. Magn. Magn. Mater.* 393, 15–19 (2015).

43. Liu, S. *et al.* New Methods for Series-Resistor Calibrations on Substrates With Losses Up to 110 GHz. *IEEE Trans. Microw. Theory Tech.* 64, 4287–4297 (2016).

44. Salipante, P. F. *et al.* Jetting of a shear banding fluid in rectangular ducts. *Phys. Rev. Fluids* 2, 033302 (2017).

45. Maxwell, J. C. A Dynamical Theory of the Electromagnetic Field. *Philos. Trans. R. Soc. Lond.* 155, 459–512 (1865).

46. D'Agostino, S. Hertz's Experiments on Electromagnetic Waves. in *A History of the Ideas of Theoretical Physics* 135–166 (Springer, Dordrecht, 2000). doi:10.1007/978-94-010-9034-6_6

47. Kuno, H. J. & Shih, Y. C. Solid-state sources from 1 to 100 GHz. *Microw. J.* 145S (1989).

48. The NIST Reference on Constants, Units, and Uncertainty. Available at: https://physics.nist.gov/cuu/index.html. (Accessed: 26th October 2017)

49. Almog, I. F. *et al.* The Lorentz Oscillator and its Applications. *MIT OpenCourseWare* (2011)

50. Ashcroft, N. W. & Mermin, N. D. Solid State Physics. *Holt, Rinehart and Winston* (1976).

51. Huang, W. & Richert, R. The Physics of Heating by Time-Dependent Fields: Microwaves and Water Revisited. *J. Phys. Chem. B* 112, 9909–9913 (2008).

52. Peter Debye - Nobel Lecture: Methods to Determine the Electrical and Geometrical Structure of Molecules. Available at: https://www.nobelprize.org/nobel_prizes/chemistry/laureates/1936/debye-lecture.html. (Accessed: 3rd October 2017)

53. Fu, J. Y. On the theory of the universal dielectric relaxation. *Philos. Mag.* 94, 1788–1815 (2014).

54. Debye, P. *Polar Molecules*. (1929).

55. The Nobel Prize in Chemistry 1936. Available at: https://www.nobelprize.org/nobel_prizes/chemistry/laureates/1936/. (Accessed: 3rd October 2017)

56. Cole, K. S. & Cole, R. H. Dispersion and Absorption in Dielectrics I. Alternating Current Characteristics. *J. Chem. Phys.* 9, 341–351 (1941).

57. Havriliak, S. & Negami, S. A complex plane representation of dielectric and mechanical relaxation processes in some polymers. *Polymer* 8, 161–210 (1967).

58. Buchner, R. *et al.* The dielectric relaxation of water between 0°C and 35°C. *Chem. Phys. Lett.* 306, 57–63 (1999).

59. The Feynman Lectures on Physics Vol. II Ch. 34: The Magnetism of Matter. Available at: http://www.feynmanlectures.caltech.edu/II_34.html. (Accessed: 27th October 2017)

60. Heaviside, O. On the electromagnetic effects due to the motion of electrification through a dielectric. *Lond. Edinb. Dublin Philos. Mag. J. Sci.* 27, 324–339 (1889).

61. Fellner-Feldegg, H. Measurement of dielectrics in the time domain. *J. Phys. Chem.* 73, 616–623 (1969).

62. Microwave Engineering: David M. Pozar: 9780471448785: Amazon.com: Books. Available at: https://www.amazon.com/Microwave-Engineering-David-M-Pozar/dp/0471448788. (Accessed: 27th October 2017)

63. Marks, R. B. A multiline method of network analyzer calibration. *IEEE Trans. Microw. Theory Tech.* 39, 1205–1215 (1991).

64. DeGroot, D. C., Jargon, J. A. & Marks, R. B. Multiline TRL revealed. in *60th ARFTG Conference Digest, Fall 2002.* 131–155 (2002). doi:10.1109/ARFTGF.2002.1218696

65. Marks, R. B. A multiline method of network analyzer calibration. *IEEE Trans. Microw. Theory Tech.* 39, 1205–1215 (1991).

66. Orloff, N. D. *et al.* A Compact Variable-Temperature Broadband Series-Resistor Calibration. *IEEE Trans. Microw. Theory Tech.* 59, 188–195 (2011).

67. Booth, J. C. *et al.* Quantitative permittivity measurements of nanoliter liquid volumes in microfluidic channels to 40 GHz. *IEEE Trans. Instrum. Meas.* 59, 3279–3288 (2010).

68. Mateu, J. *et al.* Broadband Permittivity of Liquids Extracted from Transmission Line Measurements of Microfluidic Channels. in *2007 IEEE/MTT-S International Microwave Symposium* 523–526 (2007). doi:10.1109/MWSYM.2007.380523

69. Grenier, K. *et al.* Integrated Broadband Microwave and Microfluidic Sensor Dedicated to Bioengineering. *IEEE Trans. Microw. Theory Tech.* 57, 3246–3253 (2009).

70. Soft Lithography. *Annu. Rev. Mater. Sci.* 28, 153–184 (1998).

71. Zhang, Z. *et al.* Sealing SU-8 microfluidic channels using PDMS. *Biomicrofluidics* 5, 046503-046503-8 (2011).

72. Ren, Y. *et al.* A Simple and Reliable PDMS and SU-8 Irreversible Bonding Method and Its Application on a Microfluidic-MEA Device for Neuroscience Research. *Micromachines* 6, 1923–1934 (2015).

73. Lee, J. N. *et al.* Solvent Compatibility of Poly(dimethylsiloxane)-Based Microfluidic Devices. *Anal. Chem.* 75, 6544–6554 (2003).

74. Rodríguez-Ruiz, I. *et al.* Analysis of the Structural Integrity of SU-8-Based Optofluidic Systems for Small-Molecule Crystallization Studies. *Anal. Chem.* 85, 9678–9685 (2013).

75. Conybeare, J. G. G. The resistance of palladium and palladium-gold alloys. *Proc. Phys. Soc.* 49, 29 (1937).

76. Vogt, K. W. *et al.* Characterization of thin titanium oxide adhesion layers on gold: resistivity, morphology, and composition. *Surf. Sci.* 301, 203–213 (1994).

77. Keller, S. *et al.* Processing of thin SU-8 films. *J. Micromechanics Microengineering* 18, 125020 (2008).

78. Orloff, N. D. *et al.* A Compact Variable-Temperature Broadband Series-Resistor Calibration. *IEEE Trans. Microw. Theory Tech.* 59, 188–195 (2011).

79. Williams, D. F., Wang, C. M. & Arz, U. An optimal multiline TRL calibration algorithm. in *IEEE MTT-S International Microwave Symposium Digest, 2003* 3, 1819–1822 vol.3 (2003).

80. Janezic, M. D. & Williams, D. F. Permittivity characterization from transmission-line measurement. in *1997 IEEE MTT-S International Microwave Symposium Digest* 3, 1343–1346 vol.3 (1997).

81. W. M. Haynes. *CRC Handbook of Chemistry and Physics*. (CRC Press, 2017).

82. Matula, R. A. Electrical resistivity of copper, gold, palladium, and silver. *J. Phys. Chem. Ref. Data* 8, 1147–1298 (1979).

83. Marks, R. & Williams, D. F. A General Waveguide Circuit Theory. *J. Res. NIST JRES* - 97, (1992).

84. Bazant, M. Z. *et al.* Diffuse-charge dynamics in electrochemical systems. *Phys. Rev. E* 70, 021506 (2004).

85. Ragheb, T. & Geddes, L. A. The polarization impedance of common electrode metals operated at low current density. *Ann. Biomed. Eng.* 19, 151–163 (1991).

86. Jaron, D. *et al.* A mathematical model for the polarization impedance of cardiac pacemaker electrodes. *Med. Biol. Eng.* 6, 579–594 (1968).

87. Buck, R. P. Impedances of thin and layered systems: cells with even or odd numbers of interfaces. *Ann. Biomed. Eng.* 20, 363–383 (1992).

88. Pajkossy, T. Impedance of rough capacitive electrodes. *J. Electroanal. Chem.* 364, 111–125 (1994).

89. Fernández, D. P. *et al.* A Database for the Static Dielectric Constant of Water and Steam. *J. Phys. Chem. Ref. Data* 24, 33–70 (1995).

90. Malmberg, C. G. & Maryott, A. A. Dielectric Constant of Water from 0 to 100 C. *Journal of Research of the National Bureau of Standards* 56, (1956).

91. Pátek, J. *et al.* Reference Correlations for Thermophysical Properties of Liquid Water at 0.1 MPa. *J. Phys. Chem. Ref. Data* 38, 21–29 (2009).

92. *Mosby's Medical Dictionary*. (2009).

93. Solubility of Common Salts at Ambient Temperatures. in *CRC Handbook of Chemistry and Physics* (CRC Press/Taylor & Francis, 2017).

94. Buchner, R. & Hefter, G. Interactions and dynamics in electrolyte solutions by dielectric spectroscopy. *Phys. Chem. Chem. Phys.* 11, 8984–8999 (2009).

95. Elton, D. C. The origin of the Debye relaxation in liquid water and fitting the high frequency excess response. *Phys. Chem. Chem. Phys.* 19, 18739–18749 (2017).

96. Kerner, Z. & Pajkossy, T. Impedance of rough capacitive electrodes: the role of surface disorder. *J. Electroanal. Chem.* 448, 139–142 (1998).

97. Macdonald, J. R. Note on the parameterization of the constant-phase admittance element. *Solid State Ion.* 13, (1984).

98. Hong, J. *et al.* AC frequency characteristics of coplanar impedance sensors as design parameters. *Lab. Chip* 5, 270–279 (2005).

99. Timonen, J. V. I. *et al.* Magnetic Nanocomposites at Microwave Frequencies. in *Trends in Nanophysics* 257–285 (Springer, Berlin, Heidelberg, 2010). doi:10.1007/978-3-642-12070-1_11

100. Garg, T. *et al.* Room-temperature magneto-dielectric response in multiferroic $ZnFe_2O_4$ /PMN-PT bilayer thin films. *Smart Mater. Struct.* 25, 085032 (2016).

101. Reference ranges for blood tests. *Wikipedia* (2017).

102. Samet, M. *et al.* Electrode polarization vs. Maxwell-Wagner-Sillars interfacial polarization in dielectric spectra of materials: Characteristic frequencies and scaling laws. *J. Chem. Phys.* 142, 194703 (2015).

103. Desmond, M. *et al.* Maxwell-Wagner Polarization and Frequency-Dependent Injection at Aqueous Electrical Interfaces. *Phys. Rev. Lett.* 109, 187602 (2012).

104. EPR Spectroscopy Introduction.

105. Barry, W. A Broad-Band, Automated, Stripline Technique for the Simultaneous Measurement of Complex Permittivity and Permeability. *IEEE Trans. Microw. Theory Tech.* 34, 80–84 (1986).

106. Bousbahi, K. & Marcelli, R. Characterization of microwave magnetic narrow band filters by ferromagnetic resonance. *J. Appl. Phys.* 87, 5971–5973 (2000).

107. Kuanr, B. K., Camley, R. E. & Celinski, Z. Extrinsic contribution to Gilbert damping in sputtered NiFe films by ferromagnetic resonance. *J. Magn. Magn. Mater.* 286, 276–281 (2005).

108. Lee, S. *et al.* Ferromagnetic resonance of a YIG film in the low frequency regime. *J. Appl. Phys.* 120, 033905 (2016).

109. Hauser, C. *et al.* Yttrium Iron Garnet Thin Films with Very Low Damping Obtained by Recrystallization of Amorphous Material. *Sci. Rep.* 6, 20827 (2016).

110. Ermilova, E. *et al.* Dielectric measurements of aqueous DNA solutions up to 110 GHz. *Phys. Chem. Chem. Phys.* 16, 11256–11264 (2014).

111. Keller, S. *et al.* Processing of thin SU-8 films. *J. Micromechanics Microengineering* 18, 125020 (2008).

112. Feng, R. & Farris, R. J. Influence of processing conditions on the thermal and mechanical properties of SU8 negative photoresist coatings. *J. Micromechanics Microengineering* 13, 80 (2003).

113. Blanco, F. J. *et al.* Novel three-dimensional embedded SU-8 microchannels fabricated using a low temperature full wafer adhesive bonding. *J. Micromechanics Microengineering* 14, 1047 (2004).

114. Agmon, N. Tetrahedral Displacement: The Molecular Mechanism behind the Debye Relaxation in Water. *J. Phys. Chem.* 100, 1072–1080 (1996).

115. Head-Gordon, T. & Johnson, M. E. Tetrahedral structure or chains for liquid water. *Proc. Natl. Acad. Sci.* 103, 7973–7977 (2006).

116. Popov, I. *et al.* The mechanism of the dielectric relaxation in water. *Phys. Chem. Chem. Phys.* 18, 13941–13953 (2016).

Appendix-A: SU-8

A.1: Chemistry of SU-8

The SU-8 molecule relies on its epoxy side groups for crosslinking. Originally, a single molecule contains eight epoxy groups, hence the “8” in “SU-8”. After exposure to UV light, crosslinking will occur via the epoxy bonds between SU-8 molecules. Crosslinking will occur directly after UV exposure, but only to a very small degree. Noticeable crosslinking will only occur above the glass transition temperature ~55 °C [77].

We use SU-8 series 2000 and 3000 produced by MicroChem. SU-8 consist of three parts: 1) pre-polymerized single chains of SU-8 molecules (Figure 57A) with epoxy side groups along the chain (exact molecular weight is proprietary). 2) A solvent used to spread the SU-8 polymer chains evenly during spinning. For both the SU-8 2000 and 3000 series, cyclopentanone is used (Figure 57B). The solvent is referred to as "SU-8 thinner". 3) Crosslinking is initiated via a photo-acid generator, Triarylsulfonium hexafluoroantimonate salt. UV light acts to break the molecule apart (Figure 57C), creating an acid which activates/opens the epoxide/cyclic-ether. This action allows bonds to form between epoxy groups on separate SU-8 molecules, crosslinking the polymer (Figure 57D). In the 3000 series, an additional proprietary epoxy-based polymer is used in addition to the SU-8 molecule. The goal of the additional polymer is to relive stress and increase adhesion, however the 3000 series sacrifices aspect ratio (limit of 5:1 aspect ratio).

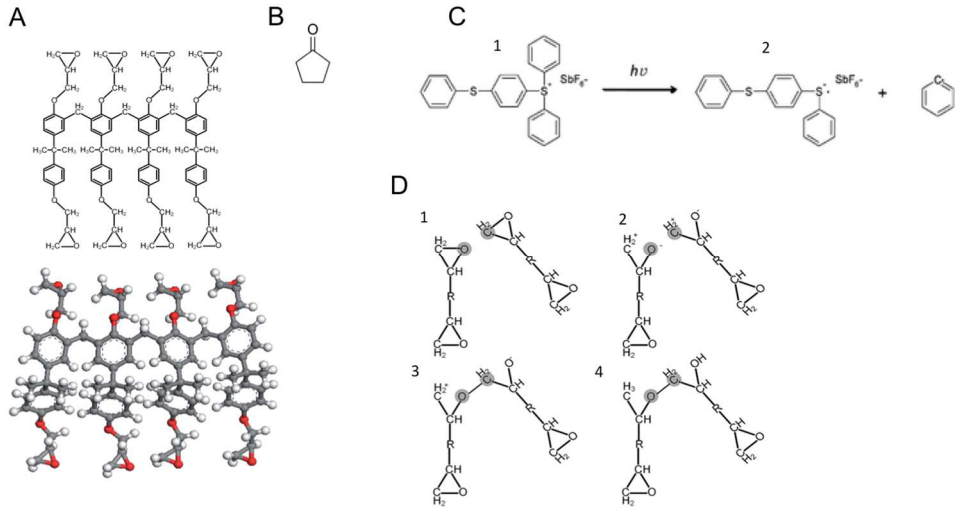

Figure 57. Chemistry of SU-8. A) molecular structure of SU-8 molecule. B) cyclopentanone solvent referred to as *SU-8 thinner*. C) Reaction of triarylsulfonium hexafluoroantimonate salt with UV to form acid. D) Epoxy bonding between cyclic-ether side groups, i.e. crosslinking.

Before crosslinking, SU-8 is mechanically a glass, with a glass transition T_g (un-crosslinked) of ~55 °C and a melting temperature T_m (un-crosslinked) between 70 and 85 °C for both the 3000 and 2000 series [111]. After crosslinking, SU-8 is a rigid structure. The glass transition is now considerable higher, T_g (crosslinked) is ~175 °C for both the 3000 and 2000 series, and there is no longer a temperature at which the material flows/melts. Crosslinked SU-8 will start to decompose at ~210 °C, and completely decomposes over ~380 °C [112].

Development, which occurs after UV exposure and crosslinking, is done with a separate solvent, Propylene glycol methyl either acetate (PGMEA). PGMEA does not act via a chemical reaction. The PGMEA molecule acts as a solvent, removing un-crosslinked SU-8, leaving the crosslinked SU-8 structure.

A.2 SU-8 Processing and Innovations

Many of our initial fabrication challenges centered on SU-8. SU-8, despite its difficulties, is a perfect material for fabricating microfluidic devices. SU-8 can be co-fabricated with existing electrical components using standard lithography techniques, has a rigid structure, and is widely chemical-resistant. SU-8 has poor adhesion to a number of materials, but has particularly poor adhesion to oxide surfaces like quartz and to gold, the two primary materials used in our devices. To prevent delamination, we consider the internal stress of the SU-8 films in addition to the adhesion of the SU-8 to the substrate. The low UV exposure process we use effectively lowers stress.

We have also starting using aluminum, where compatible, to increase adhesion. Aluminum adheres to SU-8 better than anything else with the exception of silicon. Aluminum also reflects backscatter light, which is a problem for lithographic processing on clear substrates.

The general SU-8 process has 6 steps: 1) Spin-coating the liquid SU-8. 2) Soft-bake, where solvent is removed from the film. 3) UV-exposure. 4) A post-exposure-bake, which initiates crosslinking. 5) Development, to remove un-crosslinked SU-8. 6) Hard-bake, a controversial step which is thought to reduce film stress.

All SU-8 recipes should be taken with a grain of salt, even from the manufacturer. We have found a lot of misinformation and misunderstanding about how SU-8 works. In addition, the exact molecular weight and ingredients are controlled by the manufacture.

A.2.1 Wafer Pre-bake

A pre-bake often helps with adhesion of SU-8 to the underlying substrate. Pre-baking falls under a wider category of surface preparation. For silicon oxide surfaces, such as quartz, a temperature of above ~180 °C is required to remove all water from the surface, including the monolayer directly contacting the oxide surface. For some surfaces, pre-bakes and O_2 plasma treatments can result in an SU-8 residue; this is discussed in Section A.3.

A.2.2 SU-8 Spin-on

The most important factors in spinning a flat film of SU-8 is the primary spin speed and the initial spin speed. The primary spin speed is the most important factor in determining the final film thickness and the largest factor in determining film uniformity; faster spin speeds produce a thinner and more uniform film. Faster initial spin speeds also produce a more uniform film but don't affect the final film thickness to a great extent [113]. Table 5 and Table 6 show typical spin parameters for SU-8 2050, 3050, and 2000.5.

Table 5. Spin parameters for SU-8 2050 or 3050

SU-8 2050 or 3050	Speed (rpm)	Ramp (rpm/sec)	Dwell (sec)
Step 1:	800 Initial spin speed	600	0.5
Step 2:	Primary spin speed (*)	2000	110
Step 3:	0 rpm	500	0

*4,000 rpm -> measured at 20 um thickness with SU8_3050

2,000 rpm -> measured at 51 um thickness with SU8_3050

3,000 rpm -> measured at 40 um thickness with SU8_3025 x2

Table 6. Spin parameters for SU-8 2000.5

SU-8 2000.5	Speed (rpm)	Ramp (rpm/sec)	Dwell (sec)
Step 1:	300	300	0.5
Step 2:	4000 (*)	2000	90
Step 3:	0 rpm	500	0

*4,000 rpm -> unknown with SU8_2000.5

A.2.3 Soft-Bake (SB)

Residual solvent in SU-8 films is thought to aid in crosslinking [111]. The movement of the solvent during the post-exposure bake helps with photo-initiator transport, increasing crosslinking, and thereby reducing stress in the film [111]. Soft-baking can also result in an SU-8 film with more internal stress and more cracking if a slow cool down is not performed. Un-crosslinked SU-8 is mechanically a glass, and like a glass, rapid cooling can induce thermal stresses. Soft-baking above the un-crosslinked melting temperature (~75 °C) causes the film to flow like a liquid. Higher temperature soft-bakes can be used to even out the surface of the SU-8 film through surface tension; this can be used to remove bubbles or just to make an extremely flat SU-8 surface. Again, a slow cool down is required from any temperature. No adverse effects have been seen for soft-bakes as high as 160°C, except for a greater likelihood of forming an SU-8 residue (Section A.3). The primary issue with not performing a soft-bake is that the film remains tacky for many hours after spinning.

A.2.4 UV Exposure

We have already discussed optimal UV exposure doses, however it bears repeating. SU-8 photo-acid generators are broadly sensitive to UV radiation around i-line (365 nm). Increased UV exposure results in higher photo-acid generation, in turn yielding greater crosslinking until the film is saturated with UV. For pure i-line radiation, SU-8 films require a minimum SU-8 dose around 160 mJ/cm^2 to be stable, i.e. one contiguous cross-linked structure. Due to the fact that SU-8 has low absorption; this energy dose roughly applies for all films between 2 µm and 50 µm thick. Saturation for the SU-8 films starts to occurs above 300 mJ/cm^2. In general, two regimes of exposure are preferable: A low UV dose around 200 mJ/cm^2, or an extremely high UV dose around 500 mJ/cm^2. We choose to use the low dose to reduce stress in the film, and to minimize backside reflections through our clear quartz substrates.

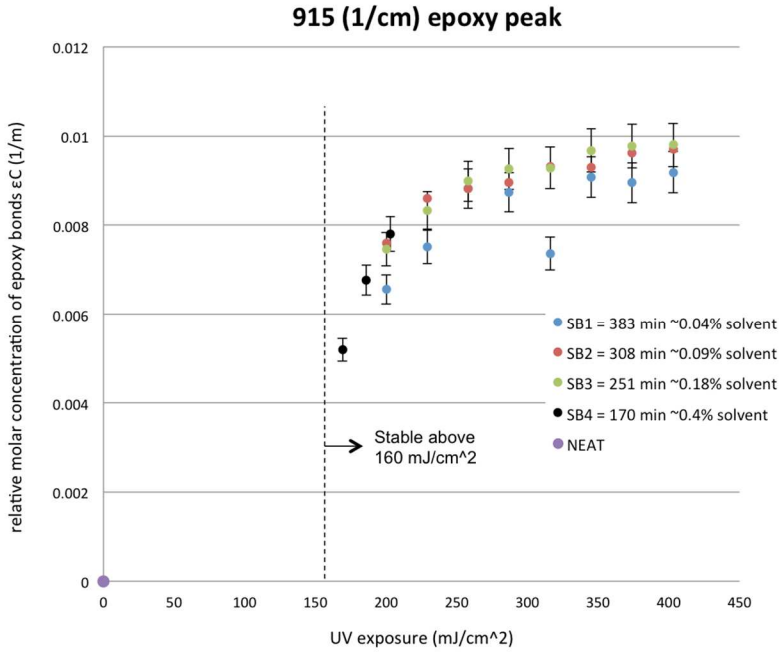

Figure 58. FT-IR measurements of 2 µm thick SU-8 films on silicon substrates. Measuring changes in the 915 cm^{-1} peak as an indication of epoxy bond formation. SU-8 films with different soft-bake times were measured using a room temperature soft-bake. Solvent concentration was determined by measuring the weight of the sample. SU-8 films were not stable bellow a UV does of 160 mJ/cm^{-2}.

A.2.5 Post-Exposure-Bake (PEB)

We use a PEB of 55 °C for 1 hour, as recommended by Keller et al. [111]. Most conventional recipes for SU-8 (Including those from MicroChem) specify a 95 °C PEB with a steady ramp-up. However, crosslinking begins to occur rapidly above the glass transition of SU-8 (~50 °C). Temperature ramping recommended in the conventional recipe is most likely inducing thermal stresses in the film, as crosslinking occurs with differing amounts of thermal expansion as the temperature is ramped up to 95 °C [111].

A.2.6 Development

SU-8 developer is used to remove un-crosslinked SU-8. Either spin-on or dunking method can be used to apply the developer. For the dunking method, only 3 minutes of agitation in SU-8 developer, followed by 1 minute of agitation in isopropanol, is needed to fully remove remaining un-crosslinked SU-8. The name "developer" is a misnomer; SU-8 developer in this case acts as a solvent: no chemical reaction occurs.

A.2.7 Hard Bake (HB)

Our fabrication process is specifically prone to *crazing*. Crazing presents as a network of small cracks over the surface of the SU-8. The phenomenon of crazing is distinct from ordinary cracks, which may form in the bulk of the material, the effect is superficial, i.e. it does not compromise the structural integrity of bulk SU-8. Crazing occurs typically in amorphous materials when transitioning from a liquid to a solid where the interfacial free energy at the surface is grater than the toughness of the material. Plastic deformation occurring within the crazing aligns the polymers to form intricate networks. Crazing can form in ceramic glasses and is often encouraged for aesthetics.

In order to lower the internal stress of the SU-8 film, thereby preventing ordinary cracking, we use a low UV exposure dose (200 mJ/cm^2). The low UV dose lowers stress because it results in a lower degree of crosslinking, however this also lowers the toughness of the SU-8, allowing the interfacial energy to dominate, resulting in crazing. The crazing might also be exacerbated by solvent shock during the development step (Section A.2.6).

Without understanding exactly why, we have found that a high-temperature hard bake (~150 °C with ramp up ramp down) works exceedingly well at removing crazing after development. Some faint trace of the crazing can still be see after HB, but for the most part the HB has permanently removed the crazing.

A.3 SU-8 Residue

We have found that certain metals can cause a phenomenon we refer to as SU-8 residue. SU-8 is commonly used as a positive mold for patterning PDMS channels, but is also used to create thick permanent structures. For some reason, SU-8 is rarely used over metal structures. This is probably why the SU-8 residue problem is not widely seen. The SU-8 residue is only noticeable after development. We believe that the residue forms through a surface catalytic reaction with the SU-8 epoxy groups. The SU-8 residue that is created can be as thick as 500 nm. If the conditions are right, the SU-8 residue will form in many locations over the wafer. We have found nothing in the literature concerning this phenomenon.

In the beginning of process development, the SU-8 residue was thought to occur randomly. After a series of tests, it was finally connected to the metals used and pre-treatment conditions such as O_2 plasma and pre-bake parameters. Also, the SU-8 residue seemed to form even when no UV exposure was made. Metals produce the residue in different amounts. Pd,

PdAu, and TiO_2, produce a thick coating of SU-8 residue; Au and Pt produce a thinner SU-8 residues that are very dependent on processing conductions (Figure 59). The fact that Pd and TiO_2 produce an SU-8 residue is unsurprising, both are known catalysts. Gold is also known to have surface catalytic properties under certain conditions. The primary cause of the formation of the SU-8 seemed to be the cleanliness of the surface. The dehydration bakes we perform are meant to remove all surface water, but also seem to promote the reaction, as a result of the fact that there is no water to get in the way. O_2 plasma is also used frequently in our processing to ensure that surfaces are free of organic compounds. This level of cleaning also allows for the formation of the residue. In addition, the O_2 plasma may be causing chemical changes to the metal surfaces, promoting the reaction. We also found that the temperature and time of the soft bake was a determining factor in the formation of the residue. Hotter and longer bakes produced a stronger reaction.

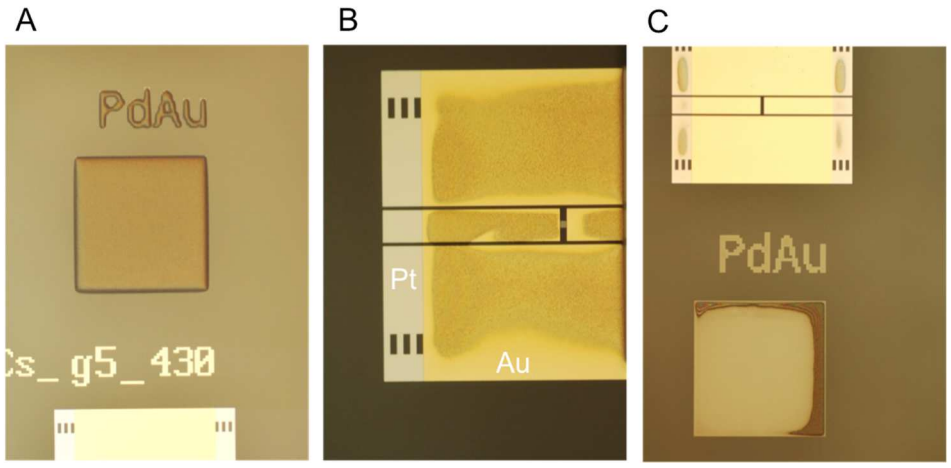

Figure 59. Examples SU-8 residue formation. A) SU-8 residue on PdAu. B) SU-8 residue on Au but not Pt. B) SU-8 residue on Pt but not Au, also on PdAu.

In our first generation of devices, our only method for mitigating the residue was to make sure to hydrate the wafer, which proved very effective. The layer of water gets in the way of the reaction. However, wafer hydration is also very bad for adhesion of SU-8 to our quartz substrates,

and it makes the already-poor adhesion of SU-8 to gold even worse. Some of the adhesion issues were addressed by managing the stress of the SU-8 film with lower UV doses. Our current solution is to use an Al adhesion layer over all, or most, areas that will be patterned with SU-8. Al has very good adhesion to SU-8, second only to silicon substrates. We still hydrate the wafer to prevent the residue from forming, but the Al layer still keeps good adhesion. If a small amount of residue forms, we can use O_2 plasma as a post-fabrication method to remove the thin-layer of SU-8 residue, without causing major damage to the surface of the permanent SU-8 structures.

Appendix-B: Dielectric Relaxation of Water.

We need to touch on the controversy surrounding the Debye interpretation of the physical origin water relaxation. There are issues with the physical model on which the Debye model is based [95]. Debye's original picture of the Brownian rotational relaxation of water was shown to be an incomplete picture; molecular dynamics simulations have shown both single molecule and cooperative reorganization processes [114]. Throughout the literature, data has shown a deviation from the Debye model above ~50 GHz. There have been a number of ad-hoc approaches to fitting measured data, most notably the Cole-Cole and double-Debye model. The double-Debye model is based on what is referred to as a "structural" relaxation, or the two-fraction model of water. The two-fraction model says there are two groups of water molecules, those that are strongly hydrogen bonded (H-bonded), and those that are free or weakly H-bonded. These two groups are often called fast and slow water respectively. The double-Debye model result in values for the second Debye relaxation time constant that vary greatly within the literature [95].

A newer model, called the "dynamic" model, says that deviation from the Debye model seen at higher frequency is due to various types of molecular motions. What has been found from recent work is that the interactions between water molecules in fact play a major role. Molecular

dynamics simulations have shown that the molecules undergo jumps as they rotate due to breaking of H-bonds [95], rather than continuous rotational Brownian diffusion in the original Debye model. It has been shown that water molecules tend to form structures that are somewhere between a "tetrahedral" arrangement [114] and a hydrogen-bonded disordered network [115]; this structure can be thought of as a *quasi-lattice*. The quasi-lattice has features of the tetrahedral arrangement but can also form chains and groups/clumps of water molecules. Water molecules tend to reorient mostly through stochastic jumps between occupied and un-occupied corners of the cube bounding with the $(H_20)_5$ tetrahedron [114].

The current understanding is that there are two mechanisms for relaxation, both having to do with defects in the tetrahedral lattice: The first is orientation relaxation (i.e. structural relaxation) that we have just discussed, which occurs by discreet jumping of positions in the tetrahedral lattice (some time referred to as "ordinary" diffusion). Molecular dynamics simulations show that it is defects in the tetrahedral lattice, moving through the lattice, which allow the molecules to reorient, and thus relax the system. The tetrahedral defect concept comes from Popov et al [116] (Figure 60), and has been validated by Elton et al. [95].

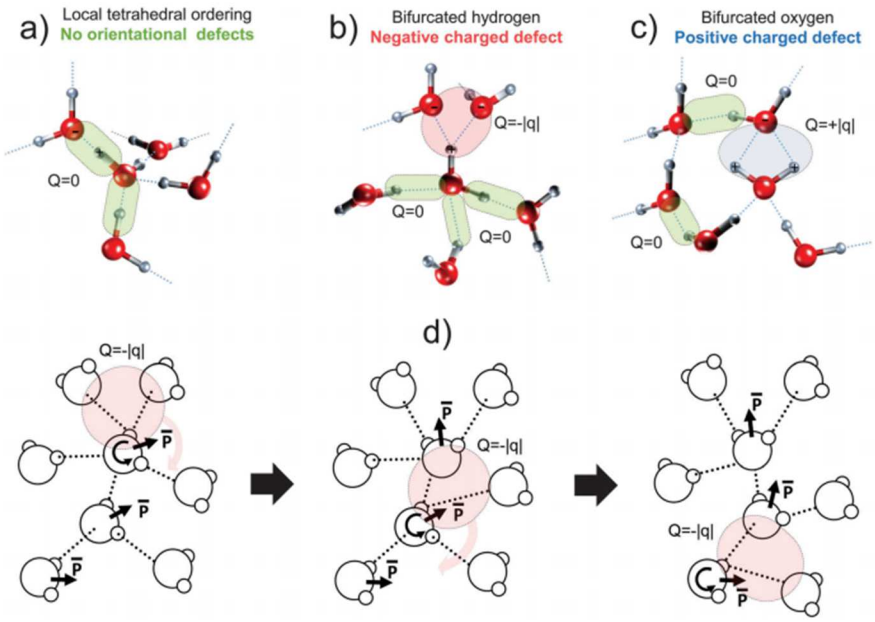

Figure 60. From figure 2 in "The mechanism of the dielectric relaxation in water" by Popov et al. [116]. a) depicts normal tetrahedral orientation. b) Depicts a negative charge defect in the tetrahedral lattice. c) Depicts a positively charge defect in the tetrahedral lattice.

The second mechanism is through ionic defects, referred to as "abnormal" proton mobility [114]. The movement of protons manifests as pars of hydroxide (HO^-) and hydronium (H_3O^+), resulting in a dipole moment, which can reorient as the defect moves through the lattice. However, orientation relaxation is the dominant mechanism, and proton mobility is commonly ignored [116].

If the Debye picture of water relaxation is incorrect, why then does the Debye model fit the data at all? Even though Debye formulated his expression with a specific physical model in mind, the general form of his equation (Equation 5) is applicable to any number of systems that return to equilibrium through random processes, generally meaning through thermal motion. The mobility of the defects also comes about through thermal motion, and thus should also present as Debye. Instead of being a characteristic time for the water molecule to rotate, the relaxation time in the Debye-type fit of water data can be thought of as a measure of the rate of diffusion of

defects through the lattice. Again, this physical interpretation of the water relaxation is still being hotly debated.

Appendix-C: Single-line Calibrations Strategy

The multi-device calibrations already discussed require microwave probing, and skilled technicians to be executed well. The multi-device calibration therefore does not lend itself to commercial applications such as point-of-care diagnostics. Ideally, we want connectorized device (a device with permanent coaxial connections), that does not require probing, and that can be calibrated without relying on the skill of the person performing the calibration. The following touches on how we have approached this problem.

C.1 XiaoCal

One solution is the Multistate Single-Connection Calibration, developed by Mr. Xiao Ma, which we endearingly refer to internally as *XiaoCal calibration*. Illustrated in Figure 61, XiaoCal uses multiple fluid standards, where the electrical response of the channel with each particular fluid is already measured and known. By measuring two or more fluid standards, error boxes can be calculated. In this calibration, the only thing that moves or changes is the fluid, which makes it appropriate for connectorized devices.

Measured Constant Known Constant

$$[T_{M_1}] = [A][Q|_{Z_1}^{Z_0}][T_{L_1}][Q|_{Z_0}^{Z_1}][B] \longrightarrow \text{Standard\#1: Air}$$

$$[T_{M_2}] = [A][Q|_{Z_2}^{Z_0}][T_{L_2}][Q|_{Z_0}^{Z_2}][B] \longrightarrow \text{Standard\#2: DIwater}$$

$$[T_{M_3}] = [A][Q|_{Z_3}^{Z_0}][T_{L_3}][Q|_{Z_0}^{Z_3}][B] \longrightarrow \text{Standard\#3: 30\% Saline}$$

Figure 61. XiaoCal measurements. Error boxes are constant, and fluid filled channel properties are known. From two or more measurements, the error boxes A and B can be estimated.

The XiaoCal fluid calibration is only a de-embedding method. To determine the propagation constant and impedance of the unknown fluid loaded line, we need either another calibration, or we need to apply an extraction algorithm such as ExtractRLCG, the closed-solution, or the trace method.

Although the de-embedding method described in Section 2.4.1 technically uses a single line on the test device. It also requires measurements of the SU-8 section and requires error box from MTRL on the decal device that are time sensitive, i.e. multiple individual measurements must be performed on the same day. This does not lend itself well to a connectorized device.

In Xiao's work, measurements of fluid standards air, water, and 30% saline, were preformed using the hybrid method described in the previous sections, giving the impedance and propagation constant for the channels filled with each fluid standard. XiaoCal was then preformed on the same devices, on a single line, using the three fluid standards. Results of XiaoCal showed that the calibration method is most accurate at lower frequencies (<~50 GHz) (Figure 62). Having 3-standards vs. 2-standards provides more accuracy for higher frequencies. However, the 2-standard method only requires air and DI water; DI water is an ideal standard compared to saline solutions, as it can be produced anywhere, without needing precise salt concentrations.

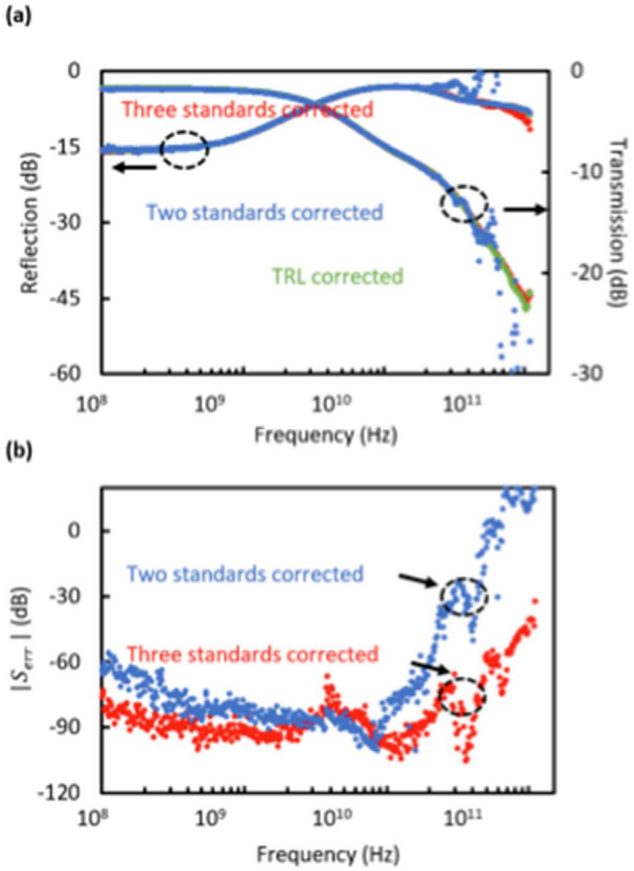

Figure 62. Tests of the XiaoCal calibration. A) S-parameter comparison between MTRL corrected S-parameters, and XiaoCal corrected S-parameters using two and three standards. B) Difference between Xiao call and MTRL for two and three standards.

C.2 Connectorized Devices

Based on the success of the XiaoCal method. We fabricated a separate set of single line devices designed to be connectorized. Figure 63 shows the assembled devices. SouthWest brand launch connectors were used to make a press-fit connection to each end of the CPW line. An aluminum package was designed to accept the chip and connectors. Afterwards the PDMS was placed over the SU-8 channels in much the same way as multi-line microfluidic devices discussed previously. Again, an acrylic press bar is used to keep the PDMS in place. These devices were designed for magnetic measurements of fluids. The CPW in the device snakes in such a way

(Figure 63B) that the direction of propagation of microwaves in the microfluidic channel is parallel with the external magnetic field (B_0). This means that the AC microwave magnetic field (B_1) is perpendicular to B_0, necessary for magnetic resonance (Section 2.2.5). An adjustable set of permanent magnets was used to create and change the external magnetic field.

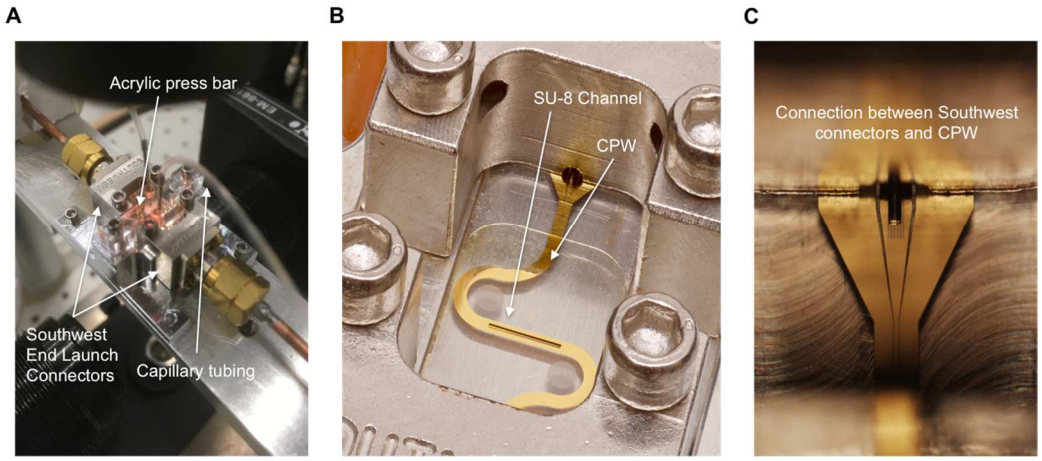

Figure 63. Connectorized devices made for magnetic measurements of fluids. Package holds Southwest connectors, chip with CPW lines and SU-8 channels, as well as an acrylic press bar to hold down the PDMS roof of the devices. A) Shows assembled device. B) shows up-close image of device with press bar and PDMS removed. C) shows an up-close image of the connection between Southwest connector and CPW line.

The wafer layout for these devices was modified from that in Section 3.4 to include the connectorized devices (Figure 64). The new wafer layout contains both MTRL fluid calibration chips, as well as MTRL bare CPW calibration chips. The connectorized devices are all placed on one side of the wafer. Since all devices are co-fabricated on the same wafer, and since the CPW and channel designs are standardized between devices, we can use MTRL devices to get the impedance and propagation constant of the fluid filled channels, and use the standard fluids on the connectorized device.

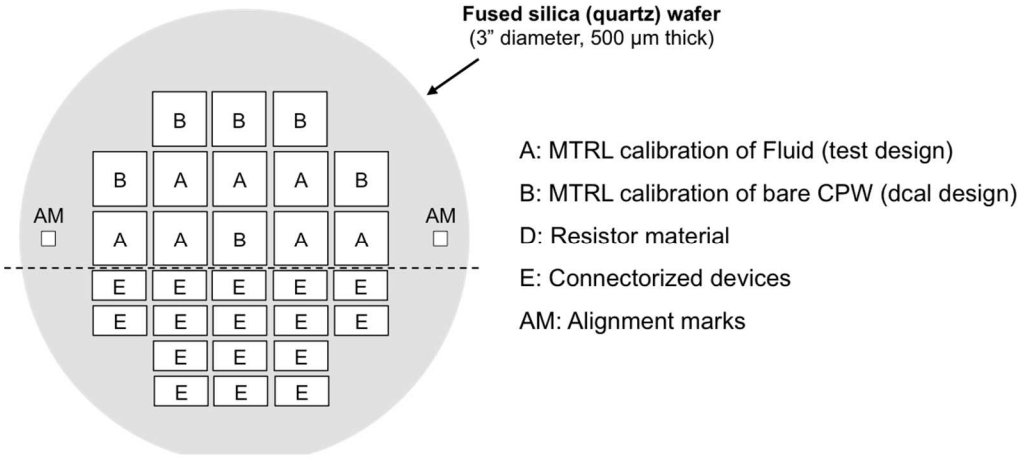

Figure 64. Example layout of connectorized devices on wafer.

This approach is scalable for making commercial devices. The majority of the wafers can allocated for fabricating connectorized devices, and a small area can be used for a few MTRL fluid devices. The properties of the fluid filled channels only need to be measured once, and these measurements are not time sensitive. Therefore, whenever connectorized device standard fluids are measured, these measurements can be used to preform XiaoCal on any of the devices fabricated on this wafer.

Appendix-D: Full-wave vs. Quasi-static

A quick note about Full-wave vs. Quasi-static solvers: Q3D uses the Quasi-static approximation. The quasi-static approximation assumes that all fields are TEM, i.e. no AC fields are in the propagation direction. It decomposes Maxwell's equations and solves electric and magnetic fields independently of one another. Based on a prescribed voltage in the conductors, it will solve for the electric fields and current in the conductors. The current is then used to predict the electric field distribution. A limitation/requirement of quasi-static tools is that the physical

size of your problem must be smaller then $1/10^{th}$ the wavelength of your highest frequency of interest to eliminate moding.

Full-wave solvers, like Ansoft HFFS, CST Microwave Studio, and the Electromagnetic Wave module of COMSOL, solve Maxwell's equations directly. This is done in a 3D volume with some boundary conditions. A full-wave solver does not make any assumption about field relationships and will find all modes (larger than the meshing size) that can propagate through any particular structure. Unlike quasi-static solvers, full-wave solvers take into account all terms of Maxwell's equations and thus also account for effects like radiation. Although the full-wave analysis provides the highest degree of accuracy, it requires extensive analytical and numerical calculations, as well as some method of benchmarking the simulation to real-world measurements. In a comparison between quasi-static and Full-wave, the quasi-static analysis is fundamentally faster in terms of CPU time.